Queen Mary
University of London

School of Physics
and Astronomy

Study of multiferroic materials by means of muon spin rotation and other complementary techniques

Doctoral thesis

Carlos Aristizabal
PhD Student

Supervisor: Dr. Alan J. Drew

Statement of originality

I, Carlos Eduardo Aristizabal Cardenas, confirm that the research included within this thesis is my own work or that where it has been carried out in collaboration with, or supported by others, that this is duly acknowledged below and my contribution indicated. Previously published material is also acknowledged below.

I attest that I have exercised reasonable care to ensure that the work is original, and does not to the best of my knowledge break any UK law, infringe any third partys copyright or other Intellectual Property Right, or contain any confidential material.

I accept that the College has the right to use plagiarism detection software to check the electronic version of the thesis.

I confirm that this thesis has not been previously submitted for the award of a degree by this or any other university.

Signature:

Date:

Abstract

Magnetic and ferroelectric materials have both had a very important impact in our society, not only because of the fascinating science behind the two phenomena, but also as a result of their use in many technological applications. The coupling and coexistence of these two order parameters within the same material opens the door to exiting new functional devices. Materials where magnetism and ferroelectricity coexist are known as multiferroic materials.

In this thesis, muon spectroscopy and other complementary experimental techniques, including neutron scattering and resonant ultrasound spectroscopy, are used to investigate two different multiferroics. Muon and total neutron scattering studies have been performed on $BiFeO_3$, one of the most studied multiferroic materials. Muon measurements reveal an anomaly in the temperature region of 200 - 220 K with a sudden and abrupt change in the muon's precession frequency that corresponds to a process of muon diffusion throughout the entire sample. The pair distribution function, calculated from total neutron scattering experiments on the compound, suggest that a change in the local structure of the material involving the bismuth-oxygen bond, in the same temperature region as the muon diffusion sets in, is a strong indicative that there is a link between two in terms of the muon diffusion being triggered by these local changes. Also, an extensive analysis and characterisation of the magnetic and ferroelectric properties of $Ba_4Dy_{0.87}Nb_{10}O_{30}$, an entirely new tetragonal tungsten bronze magnetoelectric material, is given. Neutron scattering and dielectric measurements are used to show that this material becomes ferroelectric below 470 K. We use muon spectroscopy and magnetic susceptibility measurements to investigate the magnetic properties of the material. Muon measurements under an applied electric field indicate that there is a strong coupling between the magnetism and ferroelectricity in the material. Resonant ultrasound spectroscopy is use to investigate whether the source of this coupling could be related to strain effects. Magnetic neutron scattering measurements show that there is no long range ordering in the material.

Acknowledgement

Thanks are due to my supervisor, **Alan Drew**, for his guidance, patience and his ability to keep me motivated when things were not working as planned (something that happened a lot throughout my PhD). I want to thank **Anthony Phillips** and **Martin Dove** for many useful discussions concerning many of the areas related to my research. To the students within our group, **Maureen Willis**, **Laura Nuccio** and **Leander Schulz**, for their invaluable contribution to my understanding of the μSR technique and data analysis; to our collaborators, especially **Donna Arnold** and her group at Kent university for their exceptional skill in preparing the samples for this thesis; to the beam line scientists at ISIS, especially **Francis Pratt** and **Sean Giblin**, for their support and technical help during the beam times; **Viswanathan Mohandos**, for his help and company at ISIS when experiments required staying awake all night; to my officemates and friends within the university, **Asmi Barot**, **William Little**, **Helen Duncan**, **David Holford**, **Lefteris Andritsos**, **Shuo Han**, **Ke Wang** and **Rodrigo Villavicencio**, for taking the time to listen to the various practice talks I had on my PhD and also, for the many talks completely unrelated to my work, which proved to be extremely useful when stress levels as a result of my work were high; to my mum and my sisters, **Beatriz Helena Cardenas**, **Monica Aristizabal** and **Lina Aristizabal**, for teaching me to be the person I am today, for their unconditional support and because I would not be siting here today writing this thesis if it wasn't for them; and finally, to my beautiful wife, **Laure Patry**, the person I love the most in the world and who I owe everything; for always being there for me unconditionally and her outstanding ability to listen (especially when talking about physics, something she's not really interested about but makes a super-human effort to try and enjoy the conversation).

And of course, a special thanks to the EPSRC, the funding body who have made it possible for me to take on this research project.

Contents

List of Figures

List of Tables

Chapter 1

Introduction

Magnetic and ferroelectric materials have both had a very important impact in our society, not only because of the fascinating science behind the two phenomena, but also as a result of their use in many technological applications. Ferromagnetic materials for example, whose magnetisation can be controlled by means of an applied magnetic field, have been found to be very useful for the data storage industry [8, 9]. Ferroelectric materials on the other hand, have proved to be essential for sensing and actuating devices that rely upon the switch of polarization of the ferroelectric with an applied electric field and also, the coupling between strain and electric polarization, which make these materials ideal for devices that take advantage on the correlation between elastic and electric energy [10]. Also, a lot of time and effort has been put into the development of ferroelectric random-access memories [11] as non-volatile and high speed memory media.

The coupling and coexistence of more than one order parameter within the same material opens the door to new functional devices. Materials where magnetism and ferroelectricity coexist are known as multiferroic materials. Note that, by the original definition, single phase multiferroics [12] are defined as those where either two, or all three of the primary ferroic order parameters (ferromagnetism, ferroelectricity and ferroelasticity) coexist within the same phase. However, this definition has been somehow modified as to exclude the requirement of ferroelasticity in practice as a result of the vast majority of research being focused on the coupling between ferroelectric and magnetic properties [13–

15]. The classification of these materials has also been broadened to include antiferroic order.

The search for these materials is motivated by the potential of being able to control order parameters by other than their conjugate fields, that is, controlling charges by applied magnetic fields and spins by applied voltages, which as mentioned above, promises a new path towards the design and production of new multifunctional devices [16, 17]. Even though the ideal situation would be to bring ferroelectricity and ferromagnetism together in a single phase material, this has proved to be rather difficult as a result of the tendency of the two order parameters to be mutually exclusive [2, 18, 19]. Also, the fact that magnetism and ferroelectricity may simultaneously be present in the same material doesn't necessarily mean that there is a strong coupling between the two as the microscopic mechanism behind each phenomenon is rather different, implying that they do not interfere strongly with one another [20, 21].

A promising development in the field has come in the form of tuning of electric properties of materials with applied magnetic fields, which has been achieved in materials known as frustrated magnets such as the perovskites $RMnO_3$, RMn_2O_5 (R: rare earth) [14, 22], $Ni_3V_2O_8$ [23], delafossite $CuFeO_2$ [24], and hexagonal ferrite $(BaSr)_2Zn_2Fe_{12}O_{22}$ [25]. The coupling between magnetic and ferroelectric properties in these materials is weak, and the ferroelectric polarization is about two to three orders of magnitude lower than in an ordinary ferroelectric. What makes the study of these materials so interesting, is the fact that the dielectric properties of the material are highly sensitive to an applied magnetic field and this in itself is a direct result of the ferroelectricity being induced by complex spin structures which arrange themselves in a cycloid type of configuration. This kind of spin structure will be discussed further in the text.

The objective of this work, is to give an extensive analysis and characterisation of the magnetic and ferroelectric properties of an entirely new tetragonal tungsten bronze multiferroic material by means of a series of experimental techniques and find out whether the magnetic properties of this material can be controlled with an applied electric field. We also investigate one of the most studied multiferroic materials, $BiFeO_3$ [26, 27], using

muon spectroscopy and neutron scattering in order to shed light on the temperature dependance of the magnetic properties of this material and potentially, a yet undiscovered low temperature structural phase transition involving the Bi-O bonds.

1.1 Structure of this thesis

Chapter 2: Background Basic concepts about crystal symmetry, magnetism and ferroelectricity are described. Such description lays the foundation for the discussion on multiferroic materials, starting with a brief historical overview and then moving on to a discussion about the conditions for multiferroicity to exist.

Chapter 3: Muon Spin Rotation, Relaxation and Resonance The μ^+SR technique is described. First, some of the fundamental properties of the muon are discussed and how they are created in order for experiments to be carried out. Then, a description of how the muon interacts with the sample to give information about the magnetic properties of the sample is given. Details about the technique follow, as well as a comparison between the different types of muon sources. Aspects relevant to this thesis are given.

Chapter 4: Complementary techniques In this chapter, a brief description of neutron scattering and resonant ultrasound spectroscopy (RUS) is given. The techniques are not discussed in a great deal of detail, they are used as a complement to the results obtained in the muon measurements.

Chapter 5: Experimental results: Bismuth ferrite :

The temperature dependance on the magnetic properties of $BiFeO_3$ is investigated using the μ^+SR technique. Total neutron scattering is used in order to complement the results obtained from the muon measurements.

Chapter 6: Experimental results: Magnetoelectric behaviour on the Tetragonal Tungsten

:

The magnetic and ferroelectric properties of a new tetragonal tungsten bronze magnetoelectric material, and the coupling between the two phenomena is explored with a combination of a number of experimental techniques, including μ^+SR, neutron scattering and resonant ultrasound spectroscopy. The μ^+SR technique is used

to show that the magnetic properties of the compound can be controlled with an applied electric field.

Chapter 2

Background

2.1 Introduction

The study of multiferroics is intrinsically connected to the magnetic, ferroelectric and structural properties of the sample under study. In order to understand how these three are merged to give these materials their multiferroic properties it is important to first understand some basic concepts about each of these properties separately.

In this chapter, I will give a general description of the basic physics behind the phenomena related to multiferroic materials. I shall first introduce concepts related to crystal symmetry (more specifically, I shall discuss point symmetry), then I will discuss the basics of magnetism and ferroelectricity and finally I will discuss how these can be linked in order for a material to be multiferroic.

Please note that, although symmetry analysis is a very important aspect in the field of multiferroics, is not an essential part in the understanding of the work presented in this thesis and therefore it will not be discussed in great detail. The concepts related to detailed symmetry analysis of multiferroic materials will be introduced very briefly as well as a short discussion about their relevance in the description of multiferroics and their properties. References [28, 29] contain detailed descriptions of how symmetry analysis can be used to determine magnetic point groups and whether or not the symmetry operations

that make up these groups allow for magnetic and electric coupling effects to occur.

2.2 Crystal symmetry

2.2.1 Point-symmetry: the five point symmetry operations

Point symmetry refers to the symmetry as seen from a single point in a crystal structure. There are five types of symmetry operations that describe the overall symmetry of a particular point in a lattice, these being the identity (1), rotation axes (1, 2, 3, 4, 6), mirror planes (m), centre of symmetry ($\bar{1}$) and rotoinversion axes. Following, I shall describe each one of these symmetry operations and the effect they have on atoms within a lattice [30].

Identity (1)

Identity is the symmetry operation that does nothing and leaves the system unchanged. An atom at (x, y, z) would remain at (x, y, z). Although it is an obvious symmetry operation that all structures have, it is included in order to have a more complete description of symmetry operations and also because it is needed for a more complete mathematical description of a group.

Rotation axes

Rotational symmetry exists when a structure is rotated around 360°/n where n is an integer, and after n turns the structure is indistinguishable from the original one. The value of n represents the particular rotational symmetry of the system. For instance, for $n = 2$ the system is said to have 2-fold rotation symmetry. In principle n can take any value, although the only values of n which are compatible with the presence of a lattice are $n = 1, 2, 3, 4$ and 6. There is also the special case of a 5 fold symmetry discovered in some metallic alloys. The discovery of quasicrystals, which is how this type of compound

came to be known, won the authors the 2011 Nobel Prize in chemistry [31]. Consider as an example, in terms of fractional atomic coordinates, a 2-fold rotation axis along the z axis and passing through the origin. the 2-fold operation would replicate an atom whose original postion is (x, y, z), at $(-x, -y, z)$. Similarly, a 4-fold rotation axis would replicate atoms at $(y, -x, z)$, $(-x, -y, z)$ and $(-y, x, z)$.

Mirror planes

An object is said to have mirror symmetry when it is reflected through a plane and it comes into coincidence with itself. For instance, a mirror plane parallel to the z axis and passing through the origin, will replicate an atom with initial position (x, y, z) at $(-x, y, z)$. A mirror plane perpendicular to z would replicate the same atom at $(x, y, -z)$. Figure 2.1 shows a schematic representation of rotation (left panel) and mirror (right panel) symmetry operations.

Centre of symmetry

A centre of symmetry is present whenever an object at some point, when mapped through the centre, is found on the other side at the same distance relative to the centre. Take as an example, the centre to be at $(0, 0, 0)$; An atom at (x, y, z) will be found at $(-x, -y, -z)$, as shown in figure 2.2. The centre of symmetry (also known as *inversion centre*) is perhaps one of the most important symmetry operations in the area of ferroelectrics and therefore of multiferroics, as it dictates whether there can be a net dipole moment within a crystal

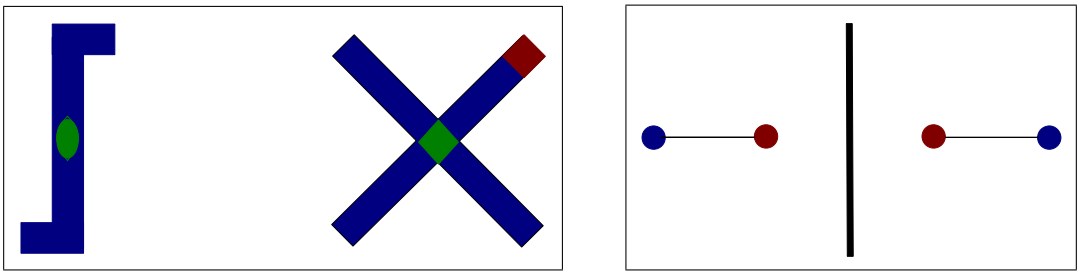

(a) 2-fold (left) and 4-fold (right) rotational symmetry

(b) Mirror symmetry

Figure 2.1: Rotational and mirror symmetries

and hence a ferroelectric polarization as a result of the loss of this symmetry operation due to atomic displacements.

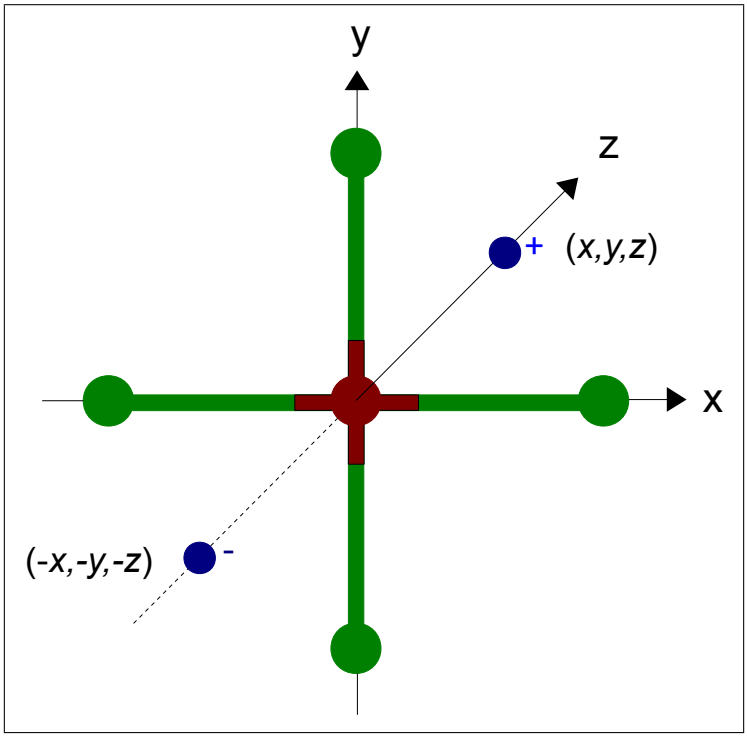

Figure 2.2: Centre of symmetry. The positive and negative signs indicate the position of the atom along the z-axis with respect to the origin.

Rotoinversion Axes

A rotoinversion axis, involves a rotation symmetry operation followed by a reflection through the centre. This type of symmetry operation is denoted as $\bar{n}$ where $n = 3, 4, 6$. Take as an example a $\bar{3}$ rotoinversion axis along the c axis. First, the 3 fold rotation would replicate an atom initially at (x, y, z) at $(-x, y, z)$, and then the inversion symmetry operation would take it to its final position at $(x, -y, -z)$.

2.2.2 The 32 crystallographic point groups

It is possible to combine different point symmetry operations which will in turn generate new symmetry operations. Consider as an example a 2-fold rotation axis and a mirror plane perpendicular to this axis [30]. Put together, this would be denoted as $2/m$. If we take the 2-fold rotation axis to be along the c axis, then an atom at (x, y, z) would

be replicated at $(-x, -y, z)$, while the mirror plane m would generate two new points at $(x, y, -z)$ and $(-x, -y, -z)$ respectively. The two last points, however, can also be replicated by applying an inversion symmetry operation to the (x, y, z) meaning that this symmetry operation is also included in the original combination $2/m$. The main point is that the combination of some symmetry operations can produce the same results as another symmetry operation.

Combining the symmetry operations in three dimensions leads to the so called *point groups*. Although there exist an infinite number of these groups in three dimensions, only the ones having rotational symmetry $n = 1, 2, 3, 4, 6$ will ever occur in crystal structure [30]. Because of this, the actual number of crystallographic point groups is 32. A table with the complete set of crystallographic point groups for each crystal class can be found in reference [30, p. 67].

2.2.3 Time reversal symmetry and magnetic point groups

In addition to the 5 crystallographic point symmetry operations, when the magnetic properties of materials are taken into account there is another symmetry operation that needs to be considered known as the time-reversal symmetry operation. This symmetry operation is vital in the description of magnetic structures as it is the combination of the time-reversal symmetry with the 5 crystallographic symmetry operations that give rise to the magnetic point groups [29, 32]. Time-reversal symmetry has the effect of reversing the direction of motion of the particles in a system. For instance, the magnetic moments of electrons in a crystal, which are visualised as current loops, when applying time reversal symmetry the direction of the current loop will reverse, which in turn will cause the magnetic moments to flip.

Magnetic point groups can then be constructed by combining the 32 crystallographic point groups with the time reversal symmetry operation, denoted as $1'$. Starting with a point group G, a new group G' can be constructed such that G' contains all the symmetry operations of G and in addition, a combination with $1'$. Taking as an example

the crystallographic point group mmm, where there is a mirror plane associated with each axis, another point group, namely $mmm1'$, can be formed. This new group will have all the symmetry elements of mmm plus the combination of those symmetry elements with the time-reversal operation $1'$.

The isomorphic subgroups that can be constructed from the combination $mmm1'$ can be written as $m'm'm'$, $m'm'm$, $m'mm'$, $mm'm'$, $m'mm$, $mm'm$, mmm'. By applying the same to the 32 crystallographic points groups, 122 magnetic point groups can be constructed. A list of these groups can be found in reference [29].

2.3 Basics of Magnetism

2.3.1 Magnetic moments

Magnetic moments are the crucial objects when talking about magnetism. Unlike electric charges, there is no evidence for the existence of magnetic monopoles [1] and therefore a single magnetic moment can instead be described as two magnetic monopoles with different magnetic charge, separated by a small distance. This object behaves just as an electric dipole and hence it is known as a *magnetic dipole*.

Macroscopically, magnetic moments can be represented as current loops. A current loop I moving around a loop of area S, then the magnetic moment $\boldsymbol{\mu}$ is given by the expression:

$$\boldsymbol{\mu} = \int I \boldsymbol{dS} \tag{2.1}$$

The magnitude of the vector dS is equal to the area of the current loop. The magnetic moment $\boldsymbol{\mu}$ points in a direction perpendicular to the plane of the loop and can therefore be either parallel or antiparallel to the angular momentum of the charged particle moving around the loop.

[1] Although there is no direct evidence, it has been reported that in spin ice systems, which are frustrated systems with no magnetic order, defects in the magnetic structure of the spin ice are in fact magnetic particles that behave as ionic charges [33]

2.3.2 The Bohr magneton

Throughout this thesis I will be using the Bohr magneton μ_B as the unit to define the magnitude of atomic magnetic moments. It is therefore worth understanding what the Bohr magneton is and where this unit comes from. Consider the classical view of an electron moving around a nucleus in an orbit of radius r. The current I due to the moving charge is given by

$$I = -e/T \tag{2.2}$$

where e is the electron charge, $T = (2\pi r)/v$ is the orbital period, v is the tangential velocity and r is the radius of the orbit. In the ground state, the magnitude of the angular momentum $L = mvr$ is equal to $\hbar$. The magnetic moment is then given by:

$$\boldsymbol{\mu} = \pi r^2 I = -\frac{e\hbar}{2m_e} = -\mu_B \tag{2.3}$$

where $\mu_B = 9.274 \times 10^{-}24\ Am^2$ is known as the **Bohr magneton**, a useful unit to describe the magnitude of magnetic moments of atoms. Since the electron has a negative electric charge, its angular momentum is antiparallel to its magnetic moment as shown in equation 2.3.

2.3.3 Bulk magnetization

In a solid, magnetism arises due to the magnetic moments of the large number of atoms the solid is made of. In the bulk phase, the magnetisation M of a solid is defined as the total magnetic moment per unit volume. In a vacuum, magnetization does not exist ($M = 0$). In this case, the magnetic field is described in terms of the field vectors **B** and **H** through a linear relation

$$\boldsymbol{B} = \mu_0 \boldsymbol{H} \tag{2.4}$$

where μ_0 is a constant known as the **permeability of free space**. In this relation, **B** is the magnetic induction and **H** is the magnetic field strength, although the two variables are really just a scaled version of each other [6]. In a solid, where a magnetisation does exist, the above equation becomes

$$\boldsymbol{B} = \mu_0(\boldsymbol{H} + \boldsymbol{M}) \tag{2.5}$$

Equation 2.5 shows that **B** and **H** can be very different in terms of magnitude and direction, and also, since **H** is the field in vacuum **H** is a field that is not concerned with the effects on magnetic solids. In other words, In a vacuum **H**=**B** but in a magnetic solid **H**≠**B**. In the case of linear materials, the magnetisation will have a dependence on the applied field through a linear relation

$$\boldsymbol{M} = \chi \boldsymbol{H} \tag{2.6}$$

where χ is a dimensionless constant of proportionality known as the **magnetic susceptibility**, defined as the degree of magnetization that a material will have in response to an applied magnetic field.

By substituting the expression for M given by equation 2.6 into equation 2.5 we get

$$\boldsymbol{B} = \mu_0(1 + \chi)\boldsymbol{H} = \mu_0\mu_r\boldsymbol{H} \tag{2.7}$$

where $\mu_r = 1 + \chi$ is known as the **relative permeability** of the material.

The values of the magnetic susceptibility χ can be either positive or negative. A negative value for the susceptibility means the material is *diamagnetic*, meaning that the magnetization within the solid opposes any applied external field. A positive susceptibility value means the material is *paramagnetic* and the magnetic moments will tend to align in the direction of the applied field and lose their alignment as soon as the field is removed because of the effects of thermal motion of the moments.

2.4 Atomic view of magnetism

So far, the discussion about magnetism has been described in terms of circulating current loops that give rise to a magnetic moment perpendicular to the plane of motion of the current loop. This is a purely classical view of magnetism, but when looking at the atomic origins of magnetism we need to consider quantum mechanical effects, or in other words, we have to understand what the quantum numbers that directly affect the magnetic moments in an atom represent.

At the atomic scale, there are two different contributions to the magnetic moment of a free atom in the absence of an applied magnetic field. The first is the angular momentum of the electrons orbiting the atomic nucleus, which is consistent with the classical interpretation. However, apart from the orbital angular momentum, electrons also have an intrinsic magnetic moment which is related to an intrinsic angular momentum. This intrinsic magnetic moment is known as *spin*. The observed magnetic moment of an atom must therefore be described as a combination of the spin and the orbital angular momenta.

In an atom, the *orbital angular momentum* of the electron depends on the electronic state that the electron occupies [6]. The orbital quantum number, l, determines the magnitude of the electron's angular momentum. The *absolute value* of the orbital angular momentum, $|L|$, of a single electron is related to the angular momentum quantum number, l, by

$$|L| = \hbar\sqrt{l(l+1)}. \tag{2.8}$$

The quantum number l, can take values $l = 0, 1, 2, 3, etc.$, which correspond to the standard labels for atomic orbitals *s, p, d* and *f*.

The magnetic quantum number, m_l, describes the orientation of the angular momentum with respect to an applied magnetic field, and it is allowed to take integer values from -l to $+l$. A p orbital for example (where $l = 1$), can have values of $m_l = 1, 0$ or -1. This implies that there exist 3 different orientations associated with the p orbitals relative to

an applied magnetic field.

The projection of the orbital angular momentum along a given axis is given by

$$L_z = m_l \hbar \tag{2.9}$$

in this case the projection is taken along the z axis. A p orbital will therefore have components of $+\hbar$, 0 or $-\hbar$.

Electron spin

The spin of an electron is described by a spin quantum number s which always has the value $s = \frac{1}{2}$. For a single electron, the absolute value of the *spin angular momentum* is

$$|\boldsymbol{S}| = \hbar\sqrt{s(s+1)} = \frac{\sqrt{3}}{2}\hbar. \tag{2.10}$$

The fact that the spin angular momentum is quantized, implies the existence of yet another quantum number. The m_s quantum number (the spin analogue to the magnetic quantum number, m_l), can only take values of $+\frac{1}{2}$ or $-\frac{1}{2}$.

The projection of spin angular momentum S along the field direction is given by $S = m_s\hbar = \pm\frac{\hbar}{2}$. There is a relation between the spin angular momentum of an electron and its magnetic moment along the field direction, which is given by

$$\boldsymbol{\mu} = -g_e \mu_B m_s \tag{2.11}$$

with an associated magnitude given by

$$|\boldsymbol{\mu}| = g_e \mu_B \sqrt{s(s+1)} \tag{2.12}$$

In these relations g is a constant known as the *Lande g-factor* whose function is, broadly speaking, to take quantum mechanical effects into account (in classical physics $g = 1$).

The Lande g-factor is given as

$$g_J = \frac{3}{2} + \frac{S(S+1) - L(L+1)}{2J(J+1)} \tag{2.13}$$

Where $J = L + S$ is the total angular momentum (the contribution from orbital and spin angular momentum). For an electron, the g-factor takes an approximate value of $g = 2$, in which case the projection of intrinsic magnetic moment along the z axis is approximately $\mp\mu_B$ [6].

Note that the $\mp\mu_B$ is the other way around (as opposed to $\pm\mu_B$) as a result of the angular momentum being antiparallel to the magnetic moment. Again, this is as a result of the negative charge of the electron, so that when $m_s = +\frac{1}{2}$, the moment is equal to $-\mu_B$. When $m_s = -\frac{1}{2}$, the moment is equal to $+\mu_B$.

2.5 Magnetic interactions

2.5.1 Magnetic dipolar interaction

As the name indicates, this type of magnetic interaction exists between two magnetic dipoles μ_1 and μ_2. The interaction energy between the two dipoles separated by some distance r is given by:

$$E = \frac{\mu_0}{4\pi r^3}\left[\boldsymbol{\mu_1}\cdot\boldsymbol{\mu_2} - \frac{3}{r^2}(\boldsymbol{\mu_1}\cdot\boldsymbol{r})(\boldsymbol{\mu_2}\cdot\boldsymbol{r})\right] \tag{2.14}$$

where μ_0 is the permeability of free space. The above equation shows that the interaction has a dependence on the two magnetic dipoles μ_1 and μ_2 and their alignment, as well as on their position relative to one another via the position vector r. Also, it shows that the energy has a $1/r^3$ dependance which is typical of this kind of interactions.

2.5.2 Exchange interaction

The concept of exchange interaction has no classical analogue, it is a pure quantum mechanical effect. This concept describes properties of electrons that lead directly to the Pauli exclusion principle. Consider two electrons in a given atom. If the spins of these two electrons are arranged antiparallel relative to one another, they will then be allowed to share the same atomic or molecular orbital. This in turn will result in an spatial overlap of their wavefunctions which will in turn cause an increase in the electrostatic Coulomb repulsion between the two electrons. If on the other hand, the spins of the electrons are aligned parallel to each other, the electrons will not be allowed to occupy the same orbital and the overlap of their wavefunctions will be minimised, which will result in a less unfavourable Coulomb repulsion and hence, an overall state of lower energy for the system. So the actual orientation of the spins of electrons has a direct effect on the spatial part of the wavefunction, and this as a result determines the electrostatic Coulomb interaction between the two particles.

The actual derivation of the exchange energy goes beyond the scope of this thesis (for a clear derivation see reference [34, p. 70] or reference [6, p. 74]), but the main result is known as the Heisenberg model and is given by

$$E = -\sum_{\mathbf{ij}} J_{ij}\mathbf{S}_i \cdot \mathbf{S}_j \tag{2.15}$$

where J_{ij} is known as the *exchange constant*, which describes the interaction between 2 atoms i and j and S is the spin of the electrons. In terms of the different types of magnetism, the exchange constant plays a vital role as it is its sign which will dictate whether the magnetic moments line up parallel ($J > 0$) or antiparallel ($J < 0$) to one another.

Direct exchange

Direct exchange occurs when an exchange interaction exists between neighbouring magnetic ions. It is called *direct* because there is no need for an intermediary between the two atoms for the interaction to take place. One would naively think that direct exchange is the most obvious route for the exchange to proceed, but in reality, this type of exchange is not very significant as a result of a lack of direct overlap between magnetic orbitals of adjacent magnetic ions.

Superexchange

This type of interaction may be defined as an indirect exchange interaction between two magnetic ions which is mediated by a non-magnetic ion, usually oxygen. To understand the exchange we can consider the exchange between two transition metal ions that are coupled antiferromagnetically. We assume the magnetism in each metal ion to come from a single unpaired electron in a d orbital and also that the oxygen atom has 2 electrons on its p orbital. Antiferromagnetic coupling lowers the energy of the system as a result of an electron hopping process, which allows the electrons to become delocalised throughout the whole structure.

Exchange in metals

This type of exchange is known as *RKKY interaction* (or as *Itinerant exchange*), and it is mediated by the conduction electrons. The spin of conduction electrons is first polarized by a localised electron and these in turn couple to other localised moments of neighbouring atoms which are a distance r away. This interaction is long range and is also an indirect effect because there is no direct coupling between neighbouring atoms.

Anisotropic exchange interaction

Also known as *Dzyaloshinsky-Moriya interaction*, in this type of exchange it is the spin-orbit interaction in one of the magnetic ions that mediates the exchange. The exchange interaction occurs between the exited state of one ion and the ground state of the other ion. For a coupling between two spins S_1 and S_2, the Hamiltonian is written as [6]

$$\hat{H}_{DM} = \mathbf{D} \cdot S_1 \times S_2 \tag{2.16}$$

where the vector $\mathbf{D}$ vanishes if the crystal field has an inversion symmetry relative to the centre between the two magnetic ions. The vector $\mathbf{D}$ is proportional to $\mathbf{x} \times \mathbf{r_{1,2}}$, where $\mathbf{r}$ is a vector connecting the magnetic ions and $\mathbf{x}$ accounts for the displacement of the oxygen ligand away from this vector (see figure 2.3). The energy in this interaction depends on $\mathbf{x}$, which represents the degree of inversion symmetry breaking [35]. The effect of this interaction is to cant the spins at small angles. In an antiferromagnet, the canting of the spins can result in a small ferromagnetic component of the magnetic moments in a direction perpendicular to the antiferromagnetic alignment.

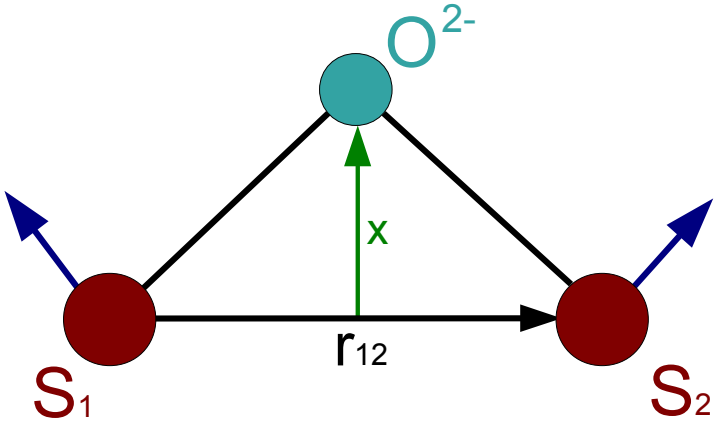

Figure 2.3: The Dzyaloshinsky-Moriya interaction. $r_{1,2}$ is the vector that connects the magnetic spins S_1 and S_2, and x is the displacement of the oxygen ion relative to the vector $r_{1,2}$.

2.6 Types of magnetic ordering

2.6.1 Ferromagnetism

Ferromagnetism is without a doubt the most easily observed of all magnetic phenomena and such materials are characterised by large positive values of susceptibility and also, an exchange constant $J > 0$. Permanent magnets are usually made of ferromagnetic materials which include Iron, Nickel and Cobalt. Ferromagnetic materials go through a phase transition from a high temperature phase in which the material has no macroscopic net magnetization, to a low temperature phase where the material has a spontaneous magnetization even when there is no applied external field. Because of their ability to retain magnetic flux, ferromagnetic materials find a wide range of applications in magnetic technologies such as transformer cores, permanent magnets and electromagnets [19]. The magnetization of the material is of course due to the magnetic moments of electrons in atoms which are randomly aligned in the high temperature phase resulting in no magnetization, and tend to spontaneously line up in the same direction below some critical temperature T_c known as the *Curie temperature*. Figure 2.4 shows the transition from a paramagnetic to a ferromagnetic state below T_C.

Very often, samples of ferromagnetic materials do not exhibit macroscopic magnetization due to the presence of what are known as magnetic domains [6]. Although the magnetic moments within each domain are all lined up in the same direction, the lack of an overall magnetization is due to the domains themselves being randomly oriented in the bulk of the sample. An applied field H causes a reorientation of the domains and this in turn results in what is known as a hysteresis loop in the magnetization M of the sample, as shown in figure 2.5.

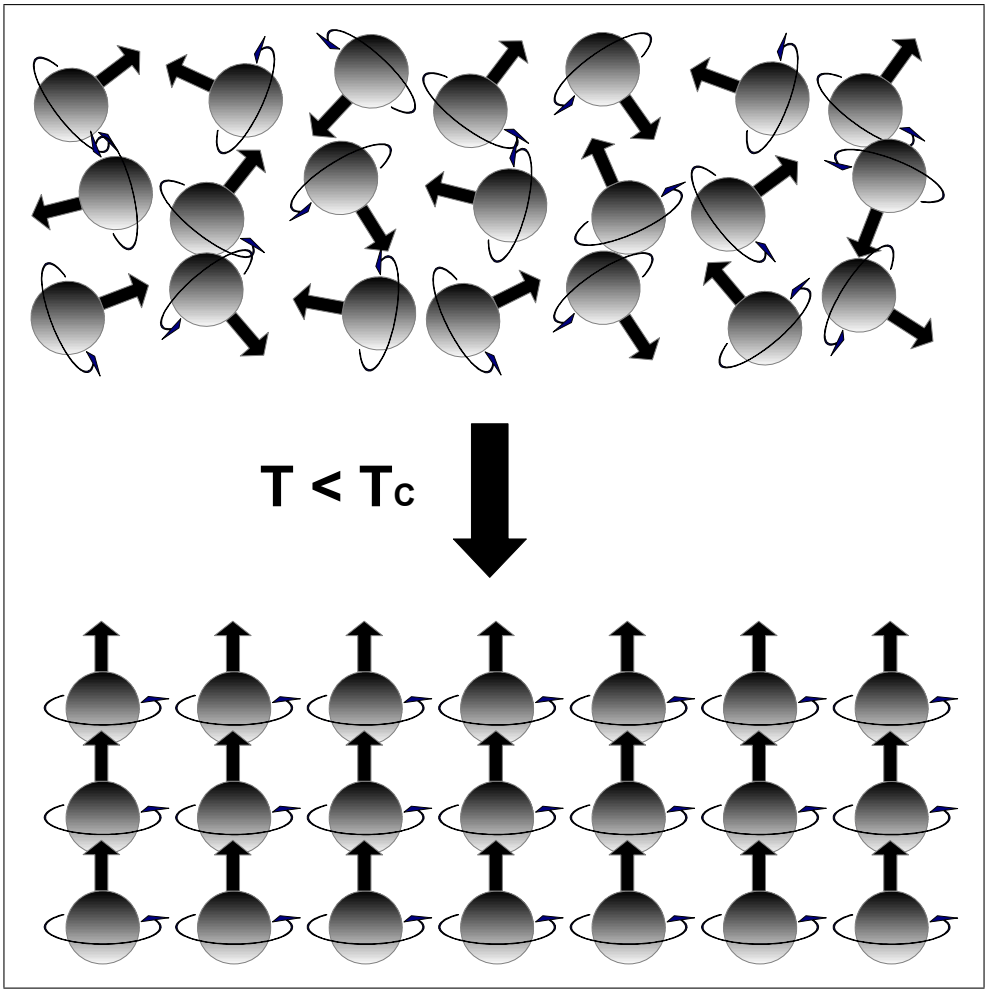

Figure 2.4: Paramagnetic - ferromagnetic transition below the Curie temperature

The ferromagnetic material starts off with no magnetization at $H = B = 0$. As the field H is increased in the positive direction the magnetic moments start to align with the field until eventually they reach a point of saturation at B_s, where all the magnetic moments point in the same direction. If the field is then reduced to zero from saturation, the magnetic induction will go from B_s to B_r. B_r is called retentivity because even though the applied field is zero the material still retains some residual flux from the initial induction. Microscopically, the magnetic moments will start to follow the field in the opposite direction (hence losing their alignment) but at $H = 0$ not all the moments lose their alignment and hence the material retains some magnetization. In order for the magnetization of the material to go to zero, the applied field has got to be further increased in the negative direction.

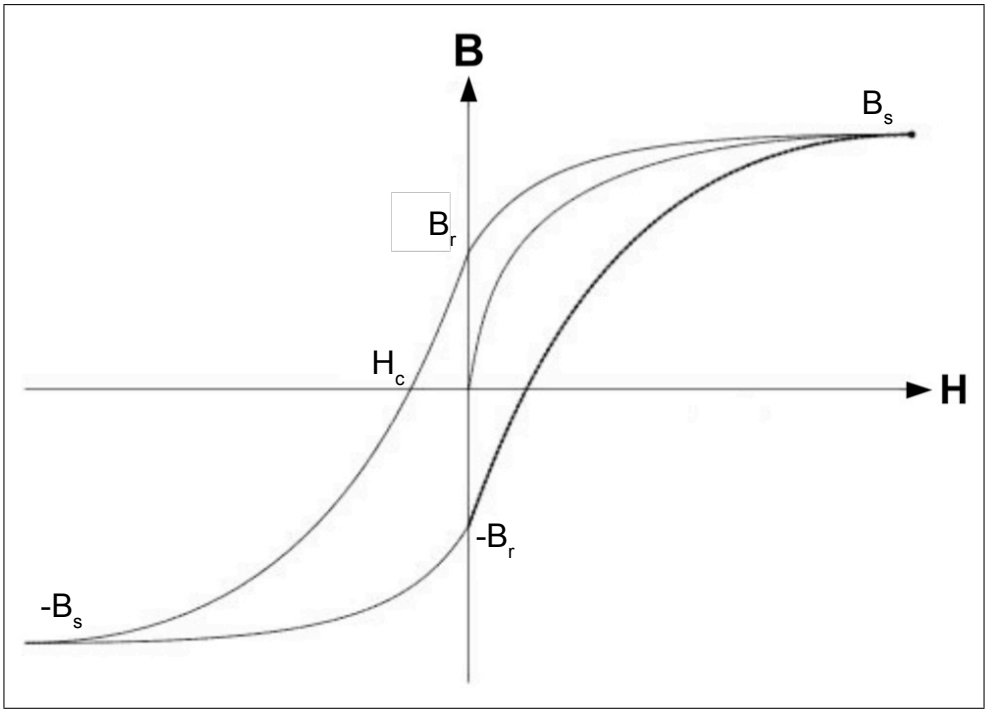

Figure 2.5: Typical hysteresis loop for a ferromagnetic material

The point at which $B = 0$ is called the *coercivity* H_c and it is defined as the reversed field needed to bring the magnetization of the material to zero. There are two different classifications of ferromagnetic materials depending of their value of coercivity. Hard magnets, require large fields in order to reduce the magnetisation to zero. Soft magnets on the other hand, are easily saturated, but at the same time only a small field is required to reduce the magnetisation to zero. Repeating the process again in the negative direction will again cause the moments to align with the field causing the sample to be magnetic again and by changing the direction of the applied field back to the positive direction, a hysteresis loop is obtained.

2.6.2 Antiferromagnetism

In an antiferromagnetic material the exchange constant $J < 0$. This type of materials consist of one or many pairs of magnetic sublattices of the same magnetic ion which occupy crystallographic positions equivalent to one another. The magnetic ions within these sublattices all have magnetic moments of equal magnitude which order antiparallel

to each other (figure 2.6) below a transition temperature known as the *Neel temperature* (T_N). An ordinary antiferromagnetic material (collinear antiferromagnet) will display no net magnetization because the magnetic moments of atoms in one sublattice will exactly cancel out the magnetic moments of the adjacent sublattice.

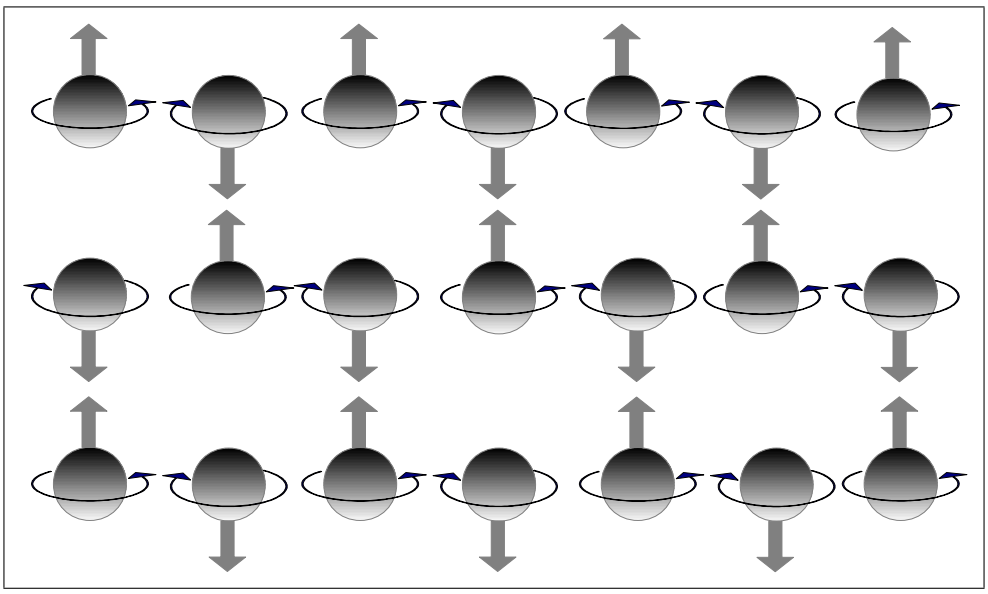

Figure 2.6: Collinear antiferromagnetic ordering

Unlike ferromagnets, antiferromagnetic materials cannot be used for applications in magnetic technologies due to their lack of net magnetization. There are cases in which the antiferromagnetic ordering can in fact exhibit a small net magnetization. This is because although the magnetization of the sublattices is still arranged in an antiparallel manner, there is a small canting moment of the spins which takes them away from the perfect antiparallel alignment as shown in figure 2.7. Because this arrangement allows for an overall net magnetization of a sample the term *weak ferromagnetim* is used to described this type of antiferomagnetic ordering.

2.6.3 Ferrimagnetism

The arrangement of the sublattices in a ferrimagnetic material is the same as that of an antiferromagnet, the key difference being that the former contains different types of magnetic ions within each sublattice which in turn makes them non-equivalent. As a

result, the magnetization of the sublattices do not cancel out and a net magnetization exists.

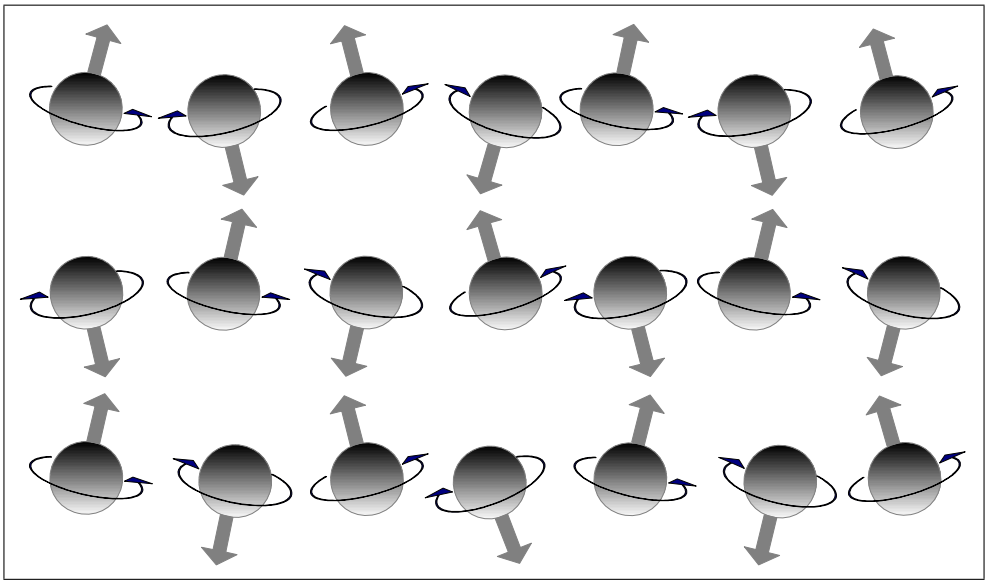

Figure 2.7: Non-collinear antiferromagnet

It is important to note that because the spontaneous magnetization in each sublattice of a ferrimagnet is different, they may have different temperature dependance, which in turn can cause the overall magnetization to have a rather complicated temperature dependence. This is because one of the sublattices may dominate the magnetization at low temperatures and the other at higher temperature. In this case, the magnetization of a ferrimagnet can then be decreased to zero and change its sign at a temperature known as the *compensation temperature* [6].

2.6.4 Helimagnetism

This type of magnetic structures are often found in rare earth metals where the atoms are arranged in layers. In dysprosium for example, there is a ferromagnetic alignment of magnetic spins in each layer and their interaction can be described in terms of the exchange constant J_1 for nearest-neighbours and J_2 for next-nearest-neighbours.

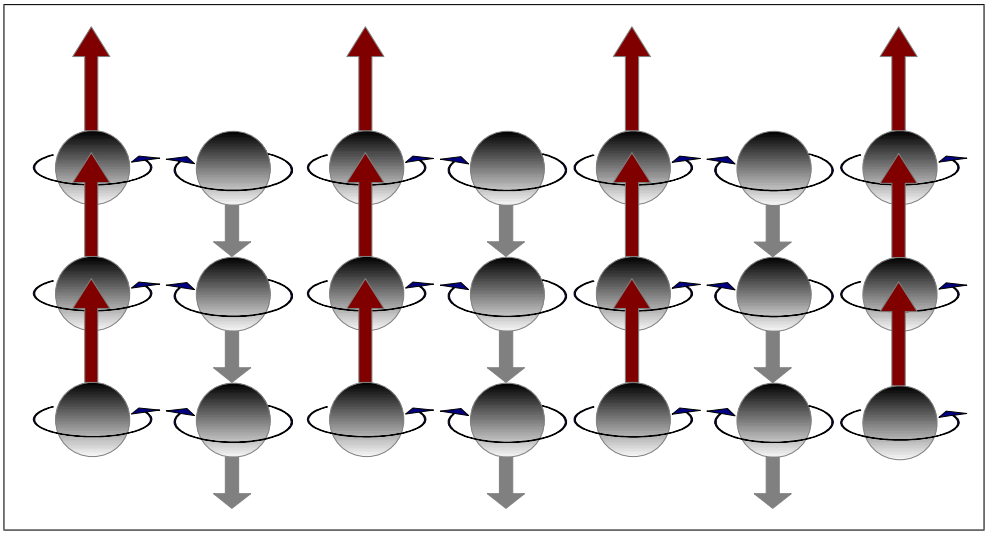

Figure 2.8: Ferrimagnetic ordering. Magnetic moments are inequivalent thus giving net magnetization to the material

If the angle between the spins in adjacent layers is ϕ (as shown in figure 2.9), then using equation 2.15, the overall energy of the system can be written as

$$E = -2NS^2(J_1\,Cos(\phi) + J_2\,Cos(2\phi)) \tag{2.17}$$

where N is the number of atoms per layer. The minimum energy is found when

$$\frac{dE}{d\phi} = 0$$

by making the substitution $Cos(2\phi) = 2\,Cos^2(\phi) - 1$ into equation 2.17 and performing the derivative we get

$$Sin(\phi)(J_1 + 4J_2\,Cos(\phi)) = 0. \tag{2.18}$$

There are 2 different solutions to this equation. For the first solution, either $sin(\phi) = 0$, implying that $\phi = 0$ (Ferromagnetism) or $\phi = \pi$ (Antiferromagnetism). For the second solution we have

$$cos\phi = -\frac{J_1}{4J_2}. \tag{2.19}$$

The above solution corresponds to a *helical* spin configuration and it is favoured when $J_2 < 0$ and $|J_1| < 4\,|J_2|$.

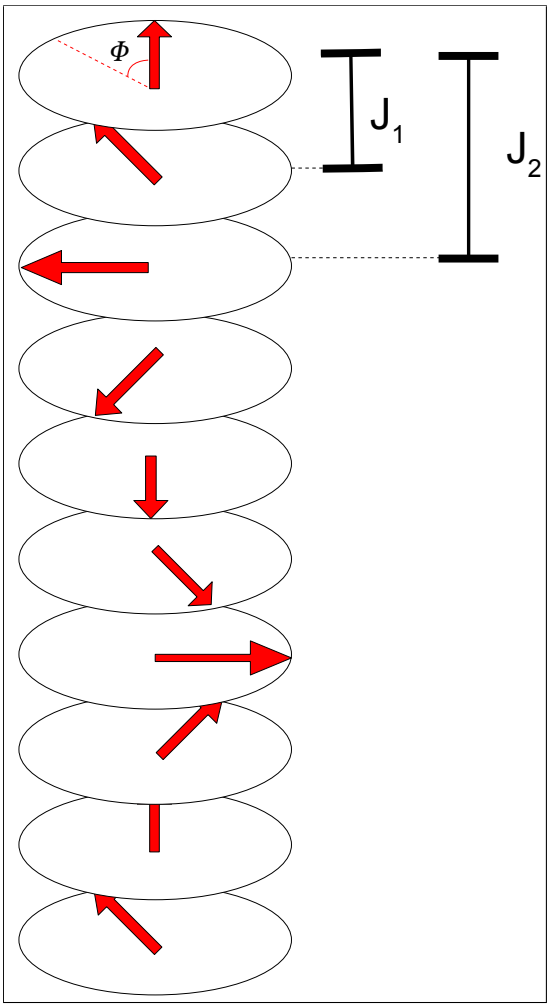

Figure 2.9: Helical magnetic ordering

As mentioned before, these helical structures are quite common among the rare earths (Tb, Dy, Ho). These elements usually have hexagonally closed packed structures and the axis along which the helix propagates is perpendicular to the planes, usually taken to be the c axis. Helical structures (referred in literature as spiral configurations) are in fact an important case in the study of magnetoelectric multiferroics. This is because first, this type of magnetic ordering induces a ferroelectric polarization (breaks space inversion symmetry) and also, the type of spiral configuration of the system (either sinusoidal,

screw, cycloidal or conical) determines whether or not the linear magnetoelectric effect is allowed by symmetry [3].

Compounds such as Cr_2BeO_4 have been reported to exhibit magnetoelectric responses in terms of the ferroelectricity being induced by the presence of a spiral like spin configurations [36, 37]. Ferroelectricity induced by magnetic ordering will be discussed in more detailed in the following section.

2.7 Ferroelectricity

Ferroelectric materials are defined as those in which there is a phase transition from a non-polar to a polar phase below a critical temperature T_c. At high temperatures, the behaviour of a ferroelectric is analogous to that of an ordinary dielectric material, that is, the application of an electric field induces an electric polarization which is lost once the field is removed. At low temperature however, the material undergoes a spontaneous polarization whose direction can be switched by applying an electric field. Many of the properties of ferroelectric materials are analogous to those found in ferromagnets in the sense that they also have domains and display a hysteretic behaviour on the polarization under an applied electric field.

Microscopically, the existence or absence of ferroelectricity depends on the balance between the short-range repulsions between adjacent electron clouds in ionic materials which favour the non-polar cubic structure, and the long range coulomb forces which favour the ferroelectric state [19, 38]. As mentioned above, the ferroelectric state has a temperature dependance. At high temperatures, a ferroelectric material maintains a symmetric, unpolarized state as a result of the forces associated with the short-range repulsions between adjacent electron clouds. At low temperatures however, the forces needed to keep a stable, polarized state are greater than the short-range repulsions, and therefore the material becomes electrically polarized even in the absence of an electric field.

In the 1920s, the study of ferroelectric materials was focused primarily on Rochelle salt

$KNa(C_4H_4O_6) \cdot 6\,H_2O$. In 1920, Joseph Valasek published a paper entitled *Piezoelectric and allied phenomena in Rochelle salt* [39] where he was able to draw a parallel between electric polarization and magnetism in terms of the hysteretic behaviour of the polarization in response to an applied electric field. Valasek studies were in fact focused on the piezoelectric effect on Rochelle salt under various conditions, but his studies lead directly to the term ferroelectricity to describe spontaneous polarization below the ferroelectric transition temperature.

Although the studies on Rochelle salt were key in understanding many of the fundamental properties of ferroelectric materials, it was in fact difficult to find a consistent theoretical model that could explain experimental results due to the complexity of the structure of the material as well as the large number of ions per unit cell [19]. Hence, it became vital to find a different class of ferroelectric compounds with a simple crystal structure and less ions per unit cell. The discovery of the *perovskite structure* was the answer to the problem, and now, some of the most studied ferroelectric compounds, such as $BiFeO_3$ [27], have this structure.

The family of perovskite-structure oxides is without a doubt the most widely studied and used in many technological applications today. Also, the materials considered in this thesis are all related to this crystal structure and hence it is important to examine the structure more closely and also to understand its importance in terms of structural flexibility that lead to their wide applicability [40, 41].

The perovskite structure has a chemical formula of the form ABO_3, where A and B are cations. In fractional coordinates, the position of the A cation is $\frac{1}{2}$, $\frac{1}{2}$, $\frac{1}{2}$, the B cation sits at the origin and the oxygen atoms occupy the positions $\frac{1}{2}, 0, 0$; $0, \frac{1}{2}, 0$; and $0, 0, \frac{1}{2}$ (The structure can also be drawn with the A site at the origin [30, p. 35]). Figure 2.10 shows the cubic perovskite structure. As shown in the figure, the B cation's position is at the centre of an octahedron of oxygen anions while the A cation is at the corners of the unit cell. The A sites have 12 oxygen neighbours and neighbouring oxygen octahedra are corner linked together forming a network that extends throughout the entire crystal, as shown in figures 2.11 and 2.12 respectively.

The importance of the perovskite structure becomes apparent when the flexibility and tolerance of chemical variation of the structure is considered. Also of great importance, is the fact that perovskite structures can undergo multiple phase transitions that can be controlled by means of a particular chemical composition. Displacive phase transitions (such as ferroelectric phase transitions) are allowed due to the flexibility in the structure set by the conditions of ionic radii [30, p. 36], which allows for this kind of displacements to take place.

2.7.1 Ferroelectric phase transition in perovskites

The ferroelectric phase transition in perovskites is the most important one for modern technology. Many ferroelectric compounds with the perovskite structure such as $BaTiO_3$ [42] and $PbTiO_3$ [43] find a whole range of technological applications as a result of the ability of the material to undergo this transition. The ferroelectric phase transition in perovskites involves the displacement of atoms relative to the centre of the oxygen octahedra that result in a net dipole moment as a result of symmetry changes in the unit cell. There are two different phenomenological models that describe the transition to the ferroelectric state. In the order-disorder model, the B cation in the perovskite structure must be able to lower its energy as a result of a displacement along one of the diagonals of the unit cell ($\langle 111 \rangle$ directions), which leads to the characteristic double well potential in terms of the position of the cation relative to the oxygen anions, as shown in figure 2.13.

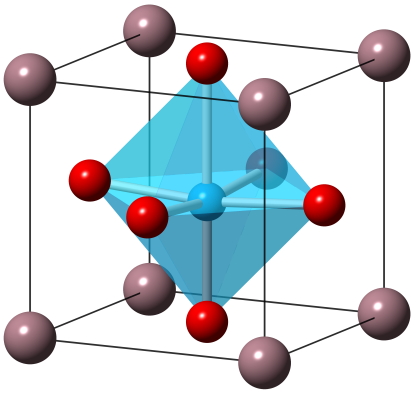

Figure 2.10: The cubic perovskite structure. The B cation (blue) sits in the middle of the oxygen octahedra (red). The Large A cation occupy the corners of the unit cell.

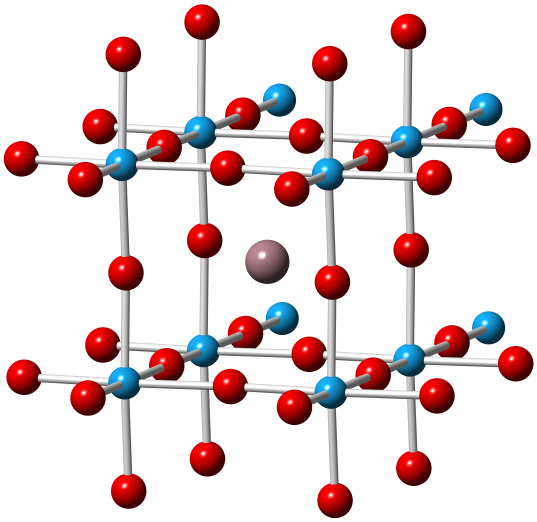

Figure 2.11: Perovskite unit cell showing the neighbouring anions of the A site. The figure shows the Fe ions on the B site (blue spheres) in octahedral coordination with the neighbouring oxygen anions.

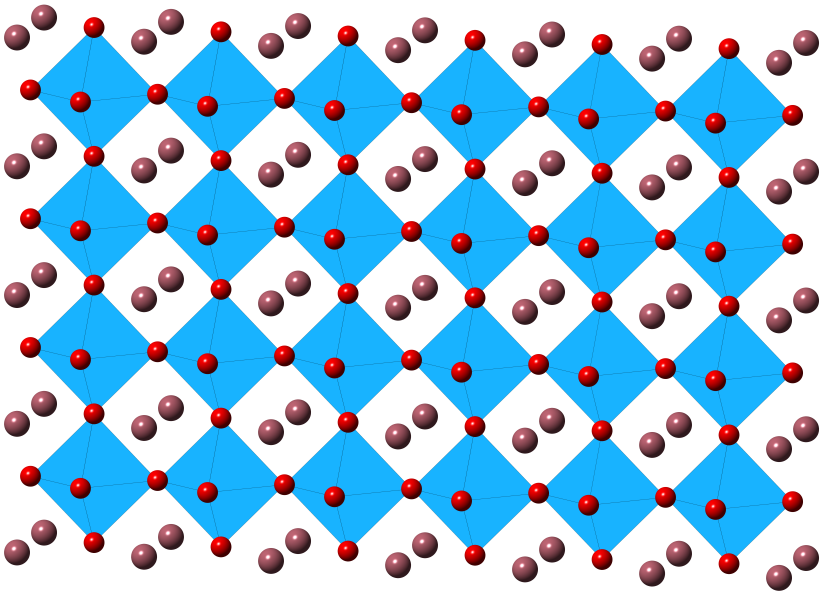

Figure 2.12: Corner linked oxygen octahedra. The sketch shows neighbouring octahedra joined at the corners forming a network that propagates throughout the whole crystal.

In the soft-mode model, there is an associated restoring force above the ferroelectric transition temperature that tends to push the B cation to the centre of symmetry if a displacement takes place. As a result, the ferroelectric state due to the ion displacement is only stable below the transition temperature. This is because the phonon associated with the restoring force becomes weaker with decreasing temperature, until eventually the frequency of the phonon is reduced to zero resulting in a spontaneous displacement

of the cation.

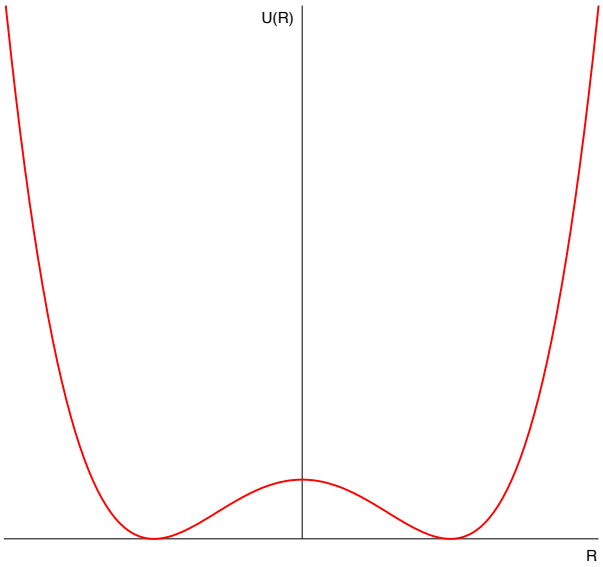

Figure 2.13: Typical double well potential energy curve for ferroelectric perovskite oxides. The two minima correspond to the displacement of the B cation with respect to to the oxygen anions (either up or down).

$PbTiO_3$ for example, has the ideal cubic structure above 766 K. Below this temperature, the material undergoes a displacive phase transition and the structure changes from an ideal cubic structure to tetragonal. This structural change gives rise to a ferroelectric polarisation as a result of the displacement of the cations and anions in opposite directions, with the polarization taken to be along the tetragonal c axis as shown in figure 2.14. Many symmetry elements are lost as a result of these displacements, which include the centre of symmetry, the 3-fold rotation axis, the 4-fold rotation axes normal to the c axis and a mirror plane perpendicular to the c axis. Due to the symmetry change of the material, a small dipole moment is developed on the tetragonal phase which can be written in terms of ionic displacement as [30, p. 37]

$$P = \sum_i q_i u_i^{(z)} \tag{2.20}$$

where q_i is the charge of ion i and $u_i^{(z)}$ is the displacement of the ion along the tetragonal c axis. The sum takes all the atoms within the unit cell.

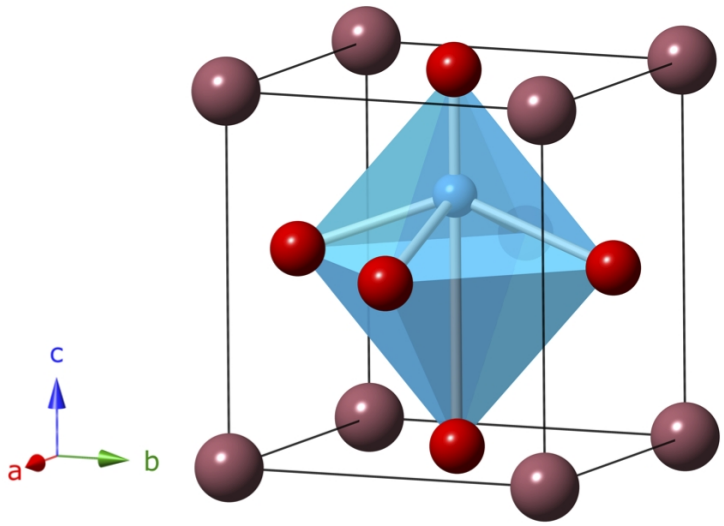

Figure 2.14: Tetragonal unit cell showing the atomic displacement of the cation in the centre of the oxygen octahedra. The system develops a ferroeletric polarization as a result of this displacement. For clarity, the displacement shown in the figure is greatly exaggerated.

In $BaTiO_3$, the ferroelectric transition also involves atomic displacements but the material goes through a variety of phase transitions with decreasing temperature, which in turn changes the magnitude and direction of the polarisation [30, p. 39].

$BaTiO_3$ is an example of a material where the Ti^{4+} cations hop between different sites that are slightly displaced away from the centre of symmetry of the oxygen octahedra. Below 393 K, the structure of the material changes from an ideal cubic to a tetragonal phase and the dielectric polarisation is along the z-axis as a result of the cations' tendency to occupy the top 4 sites . Below 273 K, the material undergoes a second phase transition from tetragonal to orthorhombic and the structure preferentially occupies 2 of the sites. A final phase transition occurs below 183 K where the material adopts a rhombohedral phase. In this final phase transition, all the Ti^{4+} ions occupy one of the sites and the polarization direction is along the diagonal [111] axis [19, 44].

2.7.2 Ferroelectricity due to lone pairs

This type of ferroelectric transition is responsible for the ferroelectricity in some perovskite compounds such as $BiFeO_3$, $BiMnO_3$, $PbVO_3$, Bi^{3+} and Pb^{2+} [2, 45, 46]. These

ions contain two outer 6s electrons that are said to be stereochemically active and are not involved in any chemical bonding. These electrons are known as lone pair valence electrons or dangling bonds and they are characterised for having a high polarizability and a strong tendency to break local inversion symmetry. The onset of this type of ferroelectricity can be visualised as the cross-gap hybridisation that exists between the occupied *p* orbitals of the oxygen anions and the empty *np* states of the corresponding lone pair cation. The lone pair of the cation causes the empty p orbitals to come closer in energy to the anion p orbitals thus inducing the off-centering of the cation from the coordination polyhedron towards the anion. This in turn generates a net dipole moment throughout the whole crystal causing the system to become ferroelectric. Work done on compounds with this mechanism for ferroelectricity, such as the one preformed by J. A. McLeod and his associates on multiferroic perovskite compounds such as $BiFeO_3$ and $BiMnO_3$ [47], shows that the origin of the ferroelectricity in this systems is indeed due to lone pairs.

2.7.3 Other types of ferroelectricity

Although not relevant to the work done in this thesis, it is important to mention other mechanisms in which the ferroelectric state can be achieved, which include *ferroelectricity due to charge ordering* [48, 49] and *Geometric ferroelectricity* [1, 50].

Ferroelectricity due to charge ordering may occur in materials containing the same magnetic species but each with a different valence charge (i.e. Fe^{2+} and Fe^{3+}). In cases like this, it is possible for the charges to arrange themselves in such a way as to have a non-centrosymmetric configuration of the system. In principle, such configuration ought to be switchable by means of an applied electric field. Compounds such as $LuFe_2O_4$ fall into this class [51].

Geometrically driven ferroelectricity does not involve any type of bond formation or charge effects which makes it compatible with the presence of magnetism. The ferroelectric transition in this case involves rotational instabilities of the coordination polyhedra

which in turn drives the displacement of the A-cation, thus inducing a dipole moment as shown in figure 2.15. A necessary requirement for this mechanism is for the different co-ordination polyhedra within the system not to be linked three dimensionally because this kind of connectivity would imply that one polyhedra rotating in one direction would cause the neighbouring polyhedra to rotate in the opposite direction, and this would cause a zero net polarization. Ferroelectricity of this type has been observed in antiferromagnetic compounds such as $YMnO_3$ [1] and $BaNiF_4$ [52].

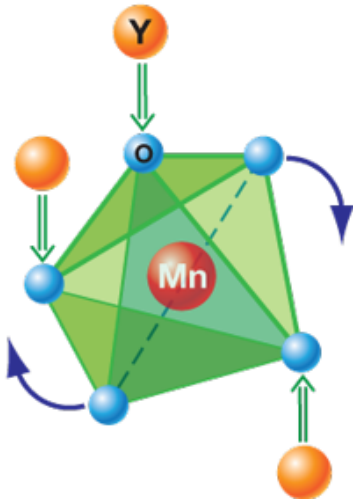

Figure 2.15: The ferroelectric mechanism in the hexagonal manganite $YMnO_3$ [1]. The figure shows the buckling of the MnO_5 polyhedra which combined with the movement of the rare earth Y gives rise to a net polarisation as indicated by the green arrows. The Mn ion does not have any influence on this mechanism for ferroelectricity. (figure reproduced from reference [2])

2.8 The magnetoelectric effect

In the year 1884, Curie was the first one to recognise that materials in which the magnetic properties could be controlled by means of electric fields, and electric properties controlled by means of a magnetic field, should in fact exist. Then, in 1957 Landau and Lifshitz gave this prediction a more precise form in mathematical terms by expanding the thermodynamic free energy in terms of B and E as [17]

$$\begin{aligned} F(\vec{E},\vec{H}) =& F_0 - P_i^s E_i - M_i^s H_i \\ & - \frac{1}{2}\epsilon_0\epsilon_{ij}E_iE_j - \frac{1}{2}\mu_0\mu_{ij}H_iH_j - \alpha_{ij}E_iH_j \\ & - \frac{1}{2}\beta_{ijk}E_iH_jH_k - \frac{1}{2}\gamma_{ijk}H_iE_jE_k - \cdots \end{aligned} \tag{2.21}$$

the polarization can be found by differentiating $F(\vec{E},\vec{H})$ with respect to E_i as

$$P_i(\vec{E},\vec{H}) = -\frac{\partial F}{\partial E_i} \tag{2.22}$$

$$= P_i^s + \epsilon_0\epsilon_{ij}E_j + \alpha_{ij}H_j + \frac{1}{2}\beta_{ijk}H_jH_k + \gamma_{ijk}H_iE_j - \cdots \tag{2.23}$$

and the magnetization by differentiating with respect to H_i as

$$M_i(\vec{E},\vec{H}) = -\frac{\partial F}{\partial H_i} \tag{2.24}$$

$$= M_i^s + \mu_0\mu_{ij}H_j + \alpha_{ij}E_i + \beta_{ijk}E_iH_j + \frac{1}{2}\gamma_{ijk}E_jE_k - \cdots \tag{2.25}$$

where $\vec{E}$ and $\vec{H}$ represent the electric and magnetic field respectively, $\vec{P^s}$ and $\vec{M^s}$ are the spontaneous polarization and magnetization, $\hat{\epsilon}$ and $\hat{\mu}$ the electric and magnetic susceptibilities.

Ignoring the first two terms in equations 2.23 and 2.25, as well as the terms with higher order coefficients β_{ijk} and γ_{ijk}, the electric polarization can then be written as

$$P_i = \alpha_{ij}H_j \tag{2.26}$$

and the magnetization as

$$M_i = \alpha_{ij} E_j \tag{2.27}$$

equations 2.26 and 2.27 show the proportionality between the polarization P_i with respect to and applied field H_j, and between the magnetization M_i with respect to an applied electric field E_j through the magnetoelectric coefficient $\boldsymbol{\alpha}_{ij}$. The coefficient $\boldsymbol{\alpha}_{ij}$ is a second rank tensor which corresponds to the induction of mangnetization as a result of an applied electric field or electric polarization in response to an applied magnetic field. This phenomenon is known as the *linear magnetoelectric effect* (ME). The tensors β and γ correspond to higher-order ME, but these are rather weak effects and hence most of the research on this phenomenon has been made on the linear ME effect.

The very first experimental observation of this effect was made by Astrov and Dzyaloshinskii in the antiferromagnetic compound Cr_2O_3 [53, 54] where they were able to show an electric field induced magnetization. Despite the fact that the effect was experimentally proved to exist, it was clear that the magnitude of the effect (either induced magnetization by an applied electric field or induced polarization by an applied magnetic field) was not near large enough for useful applications. In Cr_2O_3 for example, the magnitude of the ME coefficient was found to be $\boldsymbol{\alpha}_{zz} = 4.13\ ps\ m^{-1}$ [17]. After the successful experiment on Cr_2O_3, attempts were made to find compounds in which the ME could be enhanced. The search eventually paid off, and a number of different compounds displaying the effect were found, such as Ti_2O_3 [55], several boracites including $Ni_3B_7O_{13}I$, which was the first ferromagnetic ferroelectric boracite to be discovered [56] and phosphate compounds [57].

A general problem with the ME effect is the lack of understanding of the microscopic mechanism that drives this effect [17]. Also, it was further demonstrated that the coupling between the two phenomena is limited by [58]

$$\alpha_{ij}^2 = \chi_{ii}^e \chi_{jj}^m \tag{2.28}$$

where χ^e and χ^m correspond to the electric and magnetic susceptibilities, respectively. Equation 2.28 shows that in order to have a large magnetoelectric response the materials used must be ferroelectric and/or ferromagnetic.

2.8.1 Symmetry aspects

Understanding the coupling between magnetism and electric polarization in materials requires the treatment of symmetry properties of both phenomena as it is these properties that dictate whether the ME effect is allowed in a given compound. Polarization and magnetism have different symmetry properties. For instance, electric polarization $\boldsymbol{P}$ is represented by a polar vector which is invariant under time reversal but has a sign change under space inversion. Magnetization $\boldsymbol{M}$ on the other hand, is represented by an axial vector (also known as pseudovector) which is invariant under space inversion but changes sign under time reversal [17, 28, 59]. α is an axial second rank tensor whose components change sign under time reversal symmetry. As a result, the magnetic point groups that allow the magnetoelectric effect to occur cannot have a centre of symmetry which implies that inversion symmetry cannot be a symmetry element of the point group. However, the mangnetoelectric effect can take place in groups with an inversion centre that is primed (time-reversed) [29]. For magnetization it is time reversal symmetry which cannot be a symmetry element of the point group.

Since magnetoelectric effects involve magnetic and electric fields, neither time reversal nor space inversion symmetry can be a symmetry operation (ie. both symmetry operations must be simultaneously broken). Among the 122 Shubnikov point groups , there are 58 where the magnetoelectric effect is permitted. These groups and the forms of the tensor describing the effect are listed in [29, 32].

It can be shown why the two symmetries must be broken in order for the ME to exist. Polarization (P) is an even function for space ($\vec{r}$) and an odd function for time (t). Applying inversion symmetry (I) to both sides of the relation

$$\vec{P} = \alpha\vec{H} \tag{2.29}$$

in a system where I is a symmetry element, yields

$$I\vec{P} = I(\alpha\vec{H})$$

$$I\vec{P} = (I\alpha)(I\vec{H})$$

and hence

$$-\vec{P} = \alpha\vec{H} \tag{2.30}$$

from equations 2.29 and 2.30, $\boldsymbol{\alpha} \equiv \mathbf{0}$.

Now, magnetism (H) on the other hand, is an odd function for $\vec{r}$ and an even function for t. Applying time reversal symmetry (R) to equation 2.29 in a system where R is a symmetry operation, yields

$$R\vec{P} = R(\alpha\vec{H})$$

$$R\vec{P} = (R\alpha)(R\vec{H})$$

hence

$$\vec{P} = \alpha(-\vec{H}) \tag{2.31}$$

from 2.29 and 2.31, $\boldsymbol{\alpha} \equiv \mathbf{0}$.

Breaking of both, inversion symmetry I and time reversal R ensures the magnetoelectric tensor $\boldsymbol{\alpha}$ to be finite. In other words, the magnetoelectric effect vanishes for all symmetry groups that contain time reversal symmetry ($1'$) as well as for symmetry groups with ordinary inversion symmetry ($\bar{1}$) as a symmetry operation. If however, inversion symmetry is combined with time reversal symmetry ($\bar{1}'$), the magnetoelectric effect is allowed.

Non-linear magnetoelectric effects

Another route to combine ferroelectricity and magnetism that is currently under extensive research is the possibility of controlling the orientation of magnetic domains by means of a reorientation of ferroelectric domains with an applied electric field. The onset of ferroelectricity is accompanied by a reduction of the overall symmetry of the crystal and this in turn dictates the orientation of the magnetic easy axis through a phenomenon known as magnetocrystalline anisotropy [34]. Consider as an example a tetragonal structure with an elongation along the c-axis and the easy plane of magnetization along the a-axis. A 90° reorientation of the polarization induces a change of the easy plane of magnetization forcing the magnetic spins to align along the new orientation of the plane of magnetization. This type of coupling has been observed in $BiFeO_3$, where the easy plane of magnetization of the antiferromagnetic layers can be reoriented by means of an applied electric field [60].

2.9 Multiferroic materials

Multiferoics are defined as materials in which two or more of the primary ferroic orders (either (anti)ferromagnetism, ferroelectricity and ferroelasticity) coexist in the same phase. Even though ferroelasticity (spontaneous deformation) is considered to be one of the primary ferroic orders, the vast majority of research has been made on the coupling between ferroelectricity and magnetism and as a result, the term multiferroic applies mainly to coexistence between these two order parameters. There is also the concept of ferrotoroidicity which involves toroidal moments (which are associated with circular like spin configurations), and the cooperative arrangement of the moments. This concept, although an interesting phenomenon, is out of the scope of this thesis. In this section I will start with a brief historical overview about multiferroics, then I will describe what are the requirements for multiferroicity to exist and finally, I shall explain how these materials are classified.

2.9.1 Historical overview

Understanding magnetic and electric phenomena and indeed, the relation between them has been the subject of much interest among the scientific community for many years. The search for a coupling between the two order parameters began with the birth of the magnetoelectric effect, which can be traced back as far as 1888 with the work of Röntgen [61] in which he observed that a moving dielectric became magnetised when an electric field was applied. This was followed by the observation of polarization of a moving dielectric under an applied magnetic field 17 years later [62]. In 1894, Curie suggested the possibility of intrinsic magnetoelectric behaviour of static crystals on the basis of symmetry properties of crystals [63].

It wasn't until 1959, when Landau and Lifshitz first introduced a theoretical description for this effect in a volume of their course of theoretical physics [64]. They described the possibility of a linear coupling between magnetic and electric fields (ie. magnetization linearly proportional to an applied field) that could exist in materials with a particular magnetocrystalline symmetry. They pointed out that any magnetoelectric effect could only exist in time-asymmetric media, in other words, that the effect was odd with respect to time reversal and it hence would vanish in materials with no magnetic structure. However, they did not discuss the phenomenon any further because at the time there were no materials in which this coupling had been observed [2].

Dzyaloshinskii showed that time-reversal symmetry could be violated in some systems and on this basis, he predicted that a magnetoelectric coupling in the form of electric polarization being induced by a magnetic field (or magnetism induced by an applied electric field) should occur in the antiferromagnetic compound Cr_2O_3 [53] which was soon after confirmed experimentally by Astrov [54]. This effect is now known as the linear magnetoelectric effect.

Soon after the experimental breakthrough with Cr_2O_3, many other compounds of this class were discovered and classified according to symmetry groups that would permit the effect [18].

Due to the limitations on the magnetoelectric effect (see equation 2.28) it became clear that a new class of materials were needed in order to enhance the coupling between the order parameters. The idea of materials where two different types of ordering (i.e. alignment of magnetic moments and electric dipoles for example) could in fact coexist within the same material was brought forward. In the case of ferroelectricity and magnetism, the materials that could give a large coupling response are ferroelectric ferromagnetic materials. Such materials were given the name of *multiferroic materials* [12].

It is important to note the following relation between magnetoelectric and multiferroic materials:

- *Not all magnetoelectric materials are multiferroic*

  Cr_2O_3 for example, is a magnetoelectric antiferromagnet with no ferroelectric ordering [54]

- *Not all multiferroic materials are magnetoelectric*

  $YMnO_3$ for example, is a hexagonal ferroelectric antiferromagnet in which the magnetoelectric effect is not allowed by symmetry [1]

- *All ferroelectric ferromagnets can be magnetoelectrics*

  This is indeed the case in compounds such as $Ni_3B_7O_{13}I$, which was the very first ferroelectric ferromagnetic material to be discovered [56]

2.9.2 Conditions for coexistence in magnetoelectric multiferroics

A magnetoelectric multiferroic material must be both, ferroelectric and ferromagnetic simultaneously. The properties that the material has (either structural, physical or electronic) must meet the conditions set by its ferromagnetic and ferroelectric properties. In order for the material to be multiferroic, there are some basic requirements that have to be met, which in turn can affect the coexistence of ferroelectricity and magnetism and

therefore explain why so few of them exist [19]. In the following, I shall give a list of the main factors that limit the coexistence of the two order parameters.

1. *Symmetry*

   One of the main conditions for ferroelectricity to occur, is a structural distortion that takes the material from a high symmetry phase with an inversion symmetry to a low symmetry phase where the inversion symmetry vanishes. A spontaneous electric polarization is allowed in 31 point groups and 31 others allow for magnetic ordering to exist. Out of these, there are 13 point groups that are common to both sets and allow for the two properties to exist in the same phase (1, 2, 2', m, m', 3, 3m', 4, 4m'm', m'm2', m'm'2', 6 and 6m'm') [19]. Although this is a large reduction in the number of point groups where the effect can occur (out of the 122 Shubnikov point groups [29]), there is a significant number of compounds in one of the allowed symmetries, meaning that symmetry arguments alone cannot explain the reason why so few ferromagnetic ferroelectrics exist.

2. *Electrical properties*

   In order for a material to behave as a ferroelectric it must be an insulator, so that the flow of an electric current can be prevented when an electric field is applied and instead the material can become electrically polarized. The vast majority of ferromagnetic materials on the other hand, are metals. The lack of magnetic insulators could therefore be taken as a major cause for the scarcity of ferroelectric ferromagnetic materials. However, If we are to also consider ferrimagnetic and weak ferromagnetic (antiferromagnets with canted moments) materials, then this argument is no longer true because in fact, most ferrimagnets and weak ferromagnets are insulating materials.

3. *Chemical contra-indication: "$d^0 - ness$"*

   Ferroelectricity and magnetism are chemically contraindicated and this perhaps is one of the most critical variables in terms of scarcity of ferromagnetic ferroelectrics. For materials with the perovskite structure (ABO_3) the ferroelectric phase transi-

tion requires a d^0 electron configuration on the B site in order for the transition to become stable. Magnetism on the other hand, requires partially filled d orbitals for any type of magnetic ordering to occur, either ferri-, ferro- or antiferromagnetic. The problem with this is that for a system in a stable ferroelectric phase with a d^0 configuration, as soon as the d shell is partially occupied the ferroelectric polarization looses stability and causes the system to return to a centrosymmetric phase which is totally incompatible with ferroelectricity [13, 19].

There are a number of factors which could explain why the tendency for the B cation to shift away from the centre of symmetry disappears once the d-shell is partially filled:

- *size of the small cation*

  The question here is whether or not the cations with a d^n electronic configuration are too big to shift away from the centre of symmetry compared to those with a d^0 configuration. This question can be answered by comparing the ionic radii of some common *ferroelectric perovskites* (d^0 electron configuration) such as Ti^{4+}_{rad}=74.5 pm and Nb^{5+}_{rad}=78 pm, to those of well known *non ferroelectric perovskites* (d^n electron configuration) which include Mn^{3+}_{rad}=78.5 pm (with d^4) and Ti^{3+}_{rad}=81 pm (with d^1) [65].

  The values of ionic radii of ions with a d^1 configuration are by no means much larger to those ions with a d^0 configuration, which leads to the conclusion that ionic radii is definitely not a critical factor for a ferroelectric transition to occur.

- *Ferroelectric vs Jahn-Teller distortions*

  Conventionally, in a perovskite ferroelectric material a phase transition that takes the non-ferroelectric high symmetry structure to a lower symmetry one, occurs as a result of a shift of the B cation relative to the oxygen anions in the oxygen octahedra, causing the structure to lose the centre of symmetry.

  However, there is another type of distortion the material can undergo, namely,

a Jahn-Teller distortion [6]. This type of distortion can occur in some materials depending on the occupancies of the d-orbitals of the cation [19]. It is the d-orbital occupancies of the cation that determine whether the dominant distortion is a Jahn-Teller or a ferroelectric one.

Jahn-Teller distortions have been observed in compounds such as $LaMnO_3$ and $YTiO_3$, where for the former, Mn^{+3} ions have a d^4 electronic configuration, and for the latter, Ti^{3+} ions have a d^1 configuration. The distortion in these two materials is known as a $d-type$ Jahn-Teller distortion, which is characterised by the elongated axes of the oxygen octahedra being parallel to the crystallographic c-axis [66]. Neither of these two materials is ferroelectric.

- *d-orbital occupancy and magnetism*

  The key question in this point is whether the tendency for a perovskite oxide compound with a d^n configuration to display ferroelectricity is suppressed as a result of partially filled $d-shells$ only, or if the electron magnetic spin polarization is the main factor driving the overall effect.

  This question has been addressed by means of density functional theory, where it is possible to study the response of a known magnetic system (d^n configuration) to the artificial removal of the spin polarization of the electron to see whether or not the system becomes ferroelectric [19]. The DFT calculations reveal that removal of the electron spin polarization in fact does not have a significant effect on the tendency for the system to lose the ferroelectric behaviour, which leads to the conclusion that d-orbital occupancy is the main factor driving the absence of ferroelectricity in the system.

Although many of the factors that limit the coexistence of ferroelectricity and magnetism have been identified, there is still the question of why there are so few ferroelectric ferromagnetic materials. It is known however, that the coexistence of ferroelectricity and magnetism in multiferroic materials depend upon a series of competing factors, and it appears that the key factor affecting the coexistence of ferroelectricity and magnetism is the $d-orbital$ occupancy, at least in the case of the perovskite oxides. Despite the

difficulties in finding candidate materials, increasing interest and research on the field continues and I think it is safe to say that it is only a matter of time before multiferroic materials will find their way into modern devices and a whole range of other technological applications.

2.9.3 Classification of multiferroics

Multiferroic materials can be classified into two different groups depending on the source of the ferroelectricity and the magnetism within the material, as well as the strength of the coupling between the two order parameters.

Type I multiferroics are those where the origin of the ferroelectricity is different than that of the magnetism, and as a result the coupling between the two is very weak. normally, the onset of ferroelectricity in these materials happens at a higher temperature than the onset of magnetic ordering and the magnitude of the ferroelectric polarisation is often rather large.

In contrast, *Type II multiferroics* display a strong coupling between ferroelectricity and magnetism as a result of the onset of ferroelectricity being caused by the onset of magnetic order in the material. Despite the fact that the magnitude of the spontaneous polarisation in these materials is very small compared to the values obtained for type I multiferroics, the strong coupling between the order parameters makes them a very attractive possibility in terms of useful applications. I shall now describe type II multiferroics in more detail.

Ferroelectricity due to magnetic ordering

Also known as *improper ferroelectricity*, this type of ferroelectricity can only occur as a result of the onset of magnetic ordering within a crystal, as mentioned above.

Interest in compounds that show this effects began in 2003 with the discovery of ferroelectric activity in $TbMnO_3$, a rare earth perovskite manganite with an orthorhombic distorted structure that displays antiferromagnetic ordering with an associated long wavelength resulting from competing magnetic interactions [14]. What made this compound

so significant in the field of multiferroics was the fact that a large change in the ferroelectric polarisation was observed with an applied magnetic field at the magnetic transition temperature (large magnetoelectric response), which made it a new type of multiferroic material. Further research on the compound, both theoretical and experimental, revealed that the ferroelectric polarisation was a direct result of a cycloidal spiral spin structure [67–69]. Since the onset of ferroelectricity is due to magnetic ordering, the coupling between the two order parameters is particularly strong, making these compounds strong candidates for multiferroic based device applications.

The microscopic mechanism behind this effect in all these compounds appears to be directly linked to magnetic frustration which in turn induces a spiral type spin configuration. The fact that there is magnetic ordering implies that time reversal symmetry is already broken, and the actual spiral configuration itself ensures that inversion symmetry is also broken, that is, a change of sign of all coordinates changes the direction of rotation of the spins within the spiral, from left-handed to right handed or viceversa [35, 50]. This is shown schematically in figure 2.16. In the figure, a left handed screw spiral type structure is shown. Applying space inversion symmetry turns the left handed screw into a right handed screw, and as a result the two structures do not coincide with one another. This is only possible if space inversion symmetry is not a symmetry operation [3].

It is important to note that this is not always the case as not all spiral type configurations lead to ferroelectricity. Figure 2.17 shows the different types of spiral spin configurations. $TbMnO_3$ for example, goes through a series of magnetic transitions as a function of temperature, but ferroelectricity only appears with a particular type of spiral spin structure well below T_N. Neutron diffraction studies on the compound [70, 71] show that the Mn moments undergo an antiferromagnetic transition at $T_N \sim 41$ K. According to their model, below T_N the moments are aligned along the b axis and they adopt a sinusoidal type order but no ferroelectric polarization can be observed.

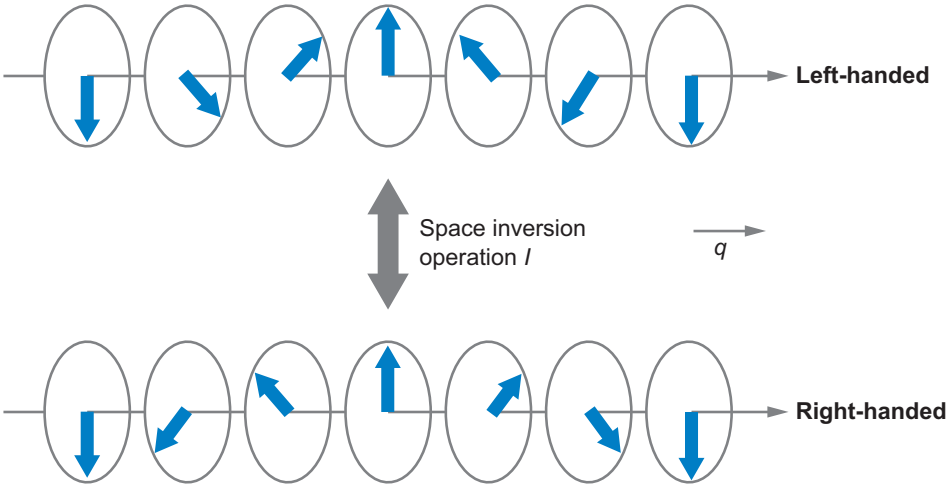

Figure 2.16: Inversion symmetry operation on a screw spiral spin configuration. The left handed screw is turned into a right handed one by applying space inversion I. q is the propagation vector of the screw configuration (reproduced from reference[3]).

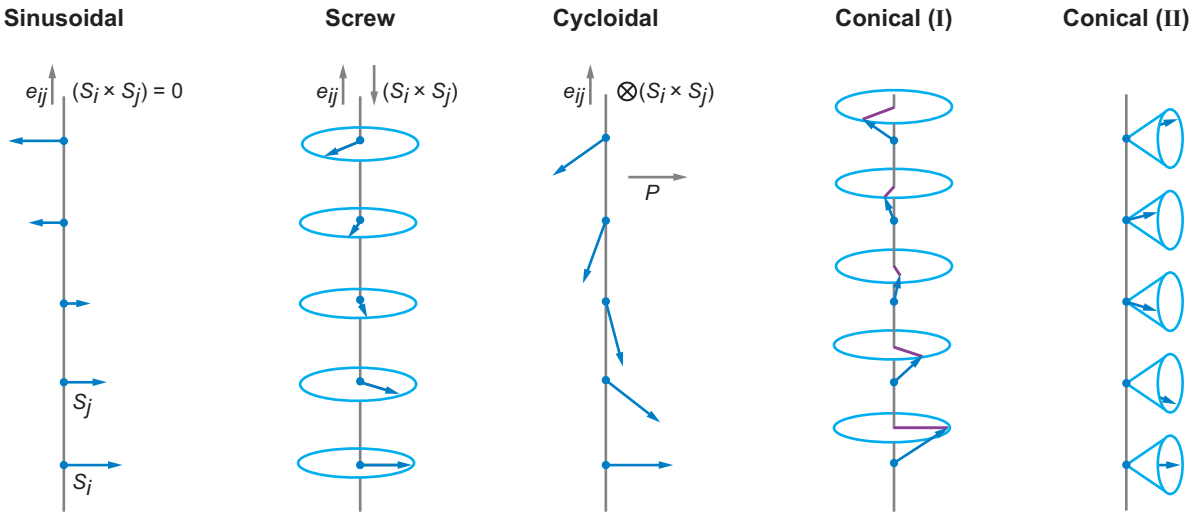

Figure 2.17: The different spiral spin configurations. The last two types (from left to right) result from the application of small fields to the screw and cycloidal types (reproduced from reference [3]).

The onset of ferroelectric order develops at $T \sim 28$ K, where the spontaneous polarisation is along the $c-axis$. However, the magnetic order changes from a sinusoidal configuration to a transversely modulated spiral magnetic structure [69], a structure which has also been confirmed in the rare-earth manganite $Tb_{1-x}Dy_xMnO_3$ at the onset of the ferroelectric phase transition [72]. Reference [3] contains a detailed review on the type of spirals there are and also, which ones allow ferroelectricity as a result of magnetic ordering.

There is a significant number of multiferroic materials in which this effect has been observed, such as manganite oxides with a chemical formula $RMnO_3$ (R=Tb, Gd or Dy) with orthorhombically distorted perovskite structure [14, 72], in $Ni_3V_2O_3$ [23] and in hexaferrite compounds (ferrite compounds with a hexagonal structure) [73]. Even though there is potential for these multiferroics to become useful for device applications in terms of the large ME coupling (such as in the case of $TbMnO_3$ [14] or $TbMn_2O_5$ [22]), the induced ferroelectricity is in fact lower than in conventional ferroelectrics such as $BaTiO_3$. In spite of these drawbacks, research in these compounds continues as it opens new ways to achieve large coupling between the two order parameters which in the end, is what will eventually lead to multiferroic materials being used in various device applications once the effect can be achieved at room temperature.

Chapter 3

Muon spin rotation, relaxation and resonance

Muon spin rotation, relaxation and resonance (also known as μSR) is a technique used to investigate intrinsic electronic and magnetic properties of materials by measuring the time evolution of the muon spin. Once muons are produced via the decay of pions, the change in the muon's polarization can be measured to a great degree of accuracy. For the work in this thesis we focus on muon spin rotation and relaxation.

A fundamental difference between this technique and those which use neutrons and x-rays as probes, is the fact that in the μSR technique there is no scattering involved in the process in terms of how the measurements are made. Muons are implanted in the sample and they remain there until they decay. The positron, which is one of the muon's decay products, is what is actually detected and gives information about the muon from which it came. For most experiments, μ^+ are used as probes to investigate the properties of the material. This is because the negative muon μ^- tends to stop close to atomic nuclei, making it a lot less sensitive to phenomena of interest in solid state physics such us magnetism or superconductivity. Positive muons on the other hand, prefer to stay away from atomic nuclei in regions of large electron density [4] making them a very useful probe to study the behaviour of the muon spin as a function of time. In this section I shall describe the basics of the μSR technique.

3.1 The muon and its properties

The muon is a spin - $\frac{1}{2}$ particle which together with the electron and the tau (and their corresponding neutrinos), belong to a family of elementary particles known as leptons. Muons and electrons share similar properties in terms of charge ($\pm e$ for matter/antimatter pairs) and spin quantum number. The only significant difference between the two particles is in their mass. The mass of the electron is $0.551 MeV/c^2$ while the mass of the muon is $105.6 MeV/c^2$ (200 times that of the electron). Because of their similarities, it is useful sometimes to think of the muon as a much heavier version of the electron or a lighter version of the proton depending on the experiment being performed. Unlike electrons and protons, muons are unstable particles with an average life time of about 2.2 μs, making it the second unstable particle with the longest life time after the neutron [74].

Table 3.1 contains a summary of the main properties of the muon compared to that of the proton and the electron.

	PARTICLE		
PROPERTY	Muon	Electron	Proton
Mass (MeV/c^2)	105.6	0.511	938.2
Charge	*e*	*-e*	*e*
Spin	½	½	½
Gyromagnetic ratio (MHz/T)	135.53	28025	42.576
Mean life time	2.2 µs	Stable	Stable

Table 3.1: The properties of the positive muon, μ^+, the electron, e^- and the proton, p. In the table, c is the speed of light and e is the charge of the electron.

Muons are produced naturally through processes in the upper atmosphere. In fact, cosmic rays arriving at sea level are mainly made up of muons and about 10000 of them pass through every square meter of the surface of the earth every minute [74]. The fact that so many muons pass through the atmosphere and survive the journey all the way to the earth's surface is clear evidence of the effects of special relativity (time dilation). This was in fact experimentally tested and confirmed in 1963 by placing muon counting devices on top of mount Washington and at sea level. This experiments showed that the count

rates ratio was consistent with the predictions of special relativity [75].

3.2 Experimental aspects of μSR

3.2.1 Muon production

Even though muons are produced naturally, the number of muons needed for experiments in condensed matter is nowhere near enough. In order to carry out experiments high muon intensities are needed, and this can be only achieved with particle accelerators. To produce a high intensity beam of muons, a high energy proton beam (800 MeV at the ISIS Laboratory in the United Kingdom) is directed into a target (usually graphite). Out of the collision between the proton beam and the nucleons in the target, pions (π^+) are created via

$$p + p \rightarrow \pi^+ + p + n.$$

Pions are created at rest in the laboratory frame of reference with a mean lifetime of 26 ns, after which they decay into muons via

$$\pi^+ \rightarrow \mu^+ + \nu_\mu$$

where ν_μ is a muon neutrino which is produced as a consequence of the system having to conserve lepton number [76]. In order for momentum to be conserved, the muon and the neutrino's momentum must be of equal magnitude and opposite to one another. Pions have zero spin which implies that the spin of the muon and the neutrino must be opposite at the moment of decay to conserve helicity. Neutrinos are known to have negative helicity, meaning that their spin is aligned antiparallel to its momentum implying that the muons themselves must also have the same alignment of their spin relative to their momentum. The muons produced out of this reaction are 100% spin polarized, and it is this property that makes the muon a very useful probe for studies in condensed matter physics.

3.2.2 Muon implantation and decay

Once the muons are produced, they are directed towards the sample of interest using magnetic and electric fields. The muons enter the sample with an initial kinetic energy of about 4 MeV and because of different processes such as ionisation of atoms and scattering with electrons, they lose their energy in a very short period of time (usually in 0.1 - 1 ns) down to a few k eV [77]. After this initial loss of energy, a process of capture and loss of electrons within the sample follows causing the muons to further reduce their energy down to a few hundred eV within a picosecond [78]. After this, there is the possibility that the muon will either capture an electron and form a stable "hydrogen-like" state known as muonium or continue as a free muon. In either case, the newly created muonium ions or free muons will lose the remaining kinetic energy to inelastic collisions with surrounding atoms or molecules before coming to a rest. The fact that the stopping processes are all Coulombic in nature implies that the muons are thermalised in the sample with negligible spin depolarization [4]. Studies concerning muonium formation and its properties are not examined in this thesis, although information related to how they can be used for studies in condensed matter physics can be found in references [4, 77, 78].

The decay of the muon is a three-body process, and is described by the relation [76]

$$\mu^+ \rightarrow e^+ + \nu_e + \bar{\nu_\mu}$$

out of which a positron, an electron-neutrino and a muon-antineutrino are created as a result of conservation of lepton number. This three body decay implies that the energy of the emitted positrons has an angular dependence and it varies depending on how the total momentum of the decay is divided between the particles involved. The muon decay is mediated by the weak interaction and as a consequence parity conservation is violated [79]. This unusual property of the weak decay implies that the positrons have a tendency to be emitted preferentially along the muon spin direction at the moment of decay allowing an accurate picture of the behaviour of the muon spin once it is implanted in the sample of interest.

Although the ideal situation would be for the positrons to be emitted exactly along the direction of the muon spin at the moment of decay, in reality they are not always emitted precisely along the spin direction of the muon. Instead, there is an intrinsic distribution around this direction which can be described by the probability function

$$W(\theta) = 1 + a\,Cos(\theta) \tag{3.1}$$

where θ is the angle between the muon spin and the direction of the emitted positron and a is known as the asymmetry factor which is given by

$$a(\eta) = \frac{2\eta - 1}{3 - 2\eta} \tag{3.2}$$

where $\eta = \frac{E}{E_{max}}$ is the ratio between the positron's energy and the energy of the most energetic emitted positrons. The asymmetry factor increases monotonically with increasing positron energy up to a value $a = 1$ which corresponds to the maximum positron energy $E_{max} = 53MeV$. Such an event only takes place when the emitted positron momentum is exactly antiparallel to the emitted neutrinos as shown in figure 3.1.

Positrons are emitted over a range of different energies with high energy positrons being the ones most likely to escape the sample and hit the detectors. In fact, low energy positrons are not emitted very often and when they are, it is very unlikely that they will be detected. Apart from the fact that these positrons aren't energetic enough to penetrate the material and reach the detector, in many experimental instruments degraders are placed between the sample area and the detectors in order to absorb incoming low energy muons and hence maximize the measured asymmetry.

The probability distribution function (equation 3.1) is plotted in figure 3.2 showing the angular distribution for positrons of different energies. Averaging over all possible positron energies yields a value of $a = \frac{1}{3}$ implying a less pronounced angular distribution as shown in figure 3.3. In spite of this, this asymmetry value allows for an accurate follow up of the muon spin precession, provided one is willing spend time taking enough data.

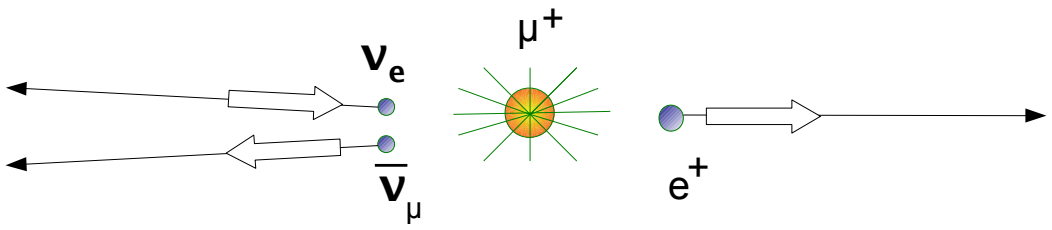

Figure 3.1: Positive muon decay. The image shows the case that gives the highest possible positron energy and hence 100% asymmetry, which correspond to the neutrinos and the positrons being emitted (almost) exactly antiparallel to each other

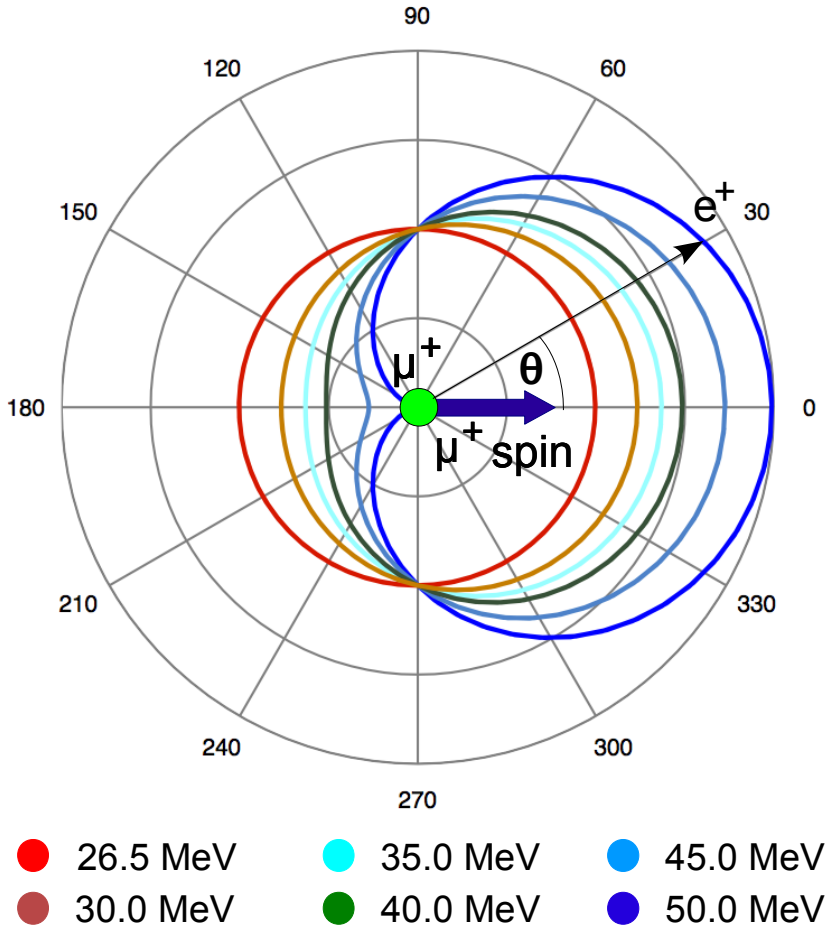

Figure 3.2: Polar plot of the angular distribution of decay positrons from positively charged muons for various energies.

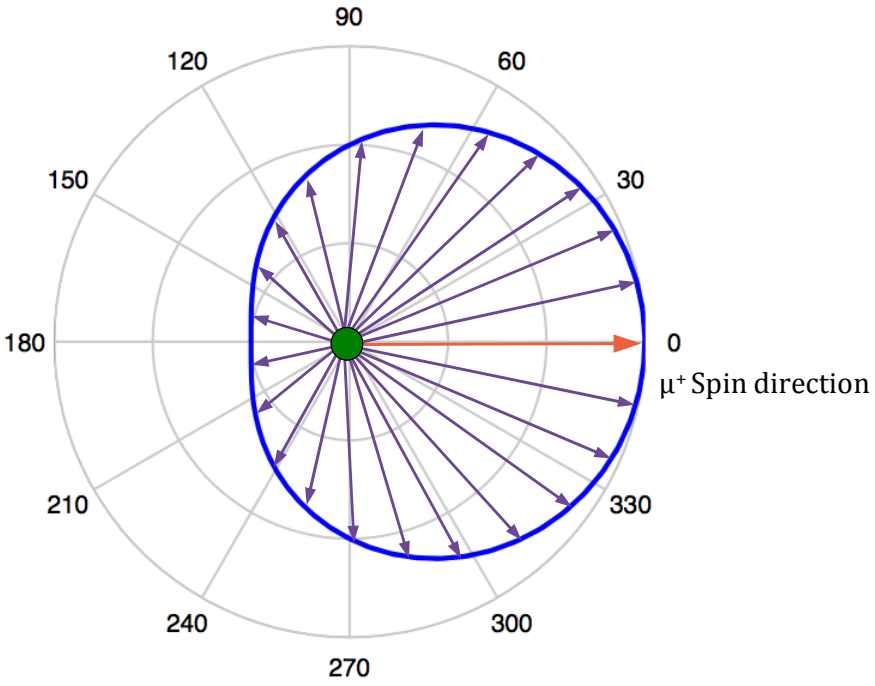

Figure 3.3: The angular distribution of decay positrons averaged over all possible energies. The yellow arrow represents the muon spin direction which is also the most probable direction in which the positron can be emitted

3.2.3 The asymmetry spectrum

A μSR experiment is performed in order to monitor the time evolution of the muon spin. To achieve this, detectors, which are typically labelled as forward (F), backward (B), up (U), down (D), left (L) and right (R), must be placed around the sample environment and these must be sensitive enough to be able to keep count of the outgoing decay positrons. Depending on the experiment to be performed, there are two different types of experimental geometries that can be used: Transverse field (TF) μSR, in which an external magnetic field is applied normal to the initial muon spin polarization, and Longitudinal field (LF) μSR, in which the field is applied parallel to the initial muon spin direction. There is also the Zero field (ZF) μSR, in which the geometry is the same as that used in LF experiments and is the type of geometry used in the experiments performed for this thesis. A more detailed description of each geometrical configuration will be given later in the text [78].

The quantity of interest in a μSR experiment is the asymmetry function which is extracted from the time histogram positron spectra. Obtaining the asymmetry involves the combination of the time spectra from two detectors placed in opposite sides of the sample. In the case of the (LF) geometry for example, the Forward and Backward detectors are used. The number of events recorded on each of the detectors can be described in terms of [78]:

- The efficiency $\epsilon_{B,F}$ of both, B and F detectors

- The background BG due to positrons coming from muons which were not implanted in the sample

- The time dependent intrinsic asymmetry of each detector. The positron count rate is proportional to $1 \pm a_{B,F}$ for muons with their spin along the symmetry axis of the detector

- The time dependent muon spin polarization $P_i(t)$ where $i = x, y, z$ depending on which axis the spin polarization direction is taken to be. Typically, the z axis is the one considered for the muon polarization direction

The number of events N, as measured with each of the detectors is proportional to the decay rate of the muons

$$N_j(t) \propto e^{(-t/\tau_\mu)} \tag{3.3}$$

hence, the number of recorded events on each detector can be written in terms of the above parameters as

$$N_B(t) = BG_B + N_0\epsilon_B \exp(-t/\tau_\mu)[1 + a_{B,F}\, P_z(t)] \tag{3.4}$$

$$N_F(t) = BG_F + N_0\epsilon_F \exp(-t/\tau_\mu)[1 - a_{B,F}\, P_z(t)] \tag{3.5}$$

where the exponential term accounts for the muon finite lifetime τ_μ and N_0 is a normalization factor that provides the scale for the positron count [80].

The experimental positron asymmetry can therefore be calculated by taking the difference between the number of events measured by each detector and dividing it by the total count rate between the two detectors. The Asymmetry is therefore

$$A_0(t) = \frac{[N_B(t) - BG_B] - [N_F(t) - BG_F]}{[N_B(t) - BG_B] + [N_F(t) - BG_F]} \tag{3.6}$$

which for vanishing background can be written as

$$A_0(t) = \frac{N_B(t) - \alpha N_F(t)}{N_B(t) + \alpha N_F(t)} \tag{3.7}$$

here, $\alpha = \epsilon_F/\epsilon_B$. The parameter alpha is an constant which compensates for small differences in efficiency between the two detectors. Alpha is also dependent on sample positioning and it is therefore necessary to determine its value for each experiment. In order to determine alpha, a small field is applied (usually 20 G) perpendicular to the muon spin polarization. The muon spin precesses about the field yielding an oscillating signal which can be used to adjust alpha until the signal oscillates symmetrically about the horizontal axis (see figures 3.4 and 3.5).

Once the alpha value and the background are determined, all the information that the experimenter wishes to gain from the sample is contained within the Asymmetry function. The maximum experimental initial asymmetry one can obtain (as given by equation 3.1) from an average of all possible positron energies corresponds to $A(t = 0) = a = \frac{1}{3}$. Although this would be the ideal case, in reality the value of $A(t = 0)$ of the instrument is considerably lower than this as a result of different factors such as the limited solid angle coverage of the detectors, the rejection of low energy positrons in the sample and the

effects of magnetic fields on positron trajectories [80, 81]. In a typical μ SR experiment, the value of the initial asymmetry ranges from $20 - 25\%$ [78].

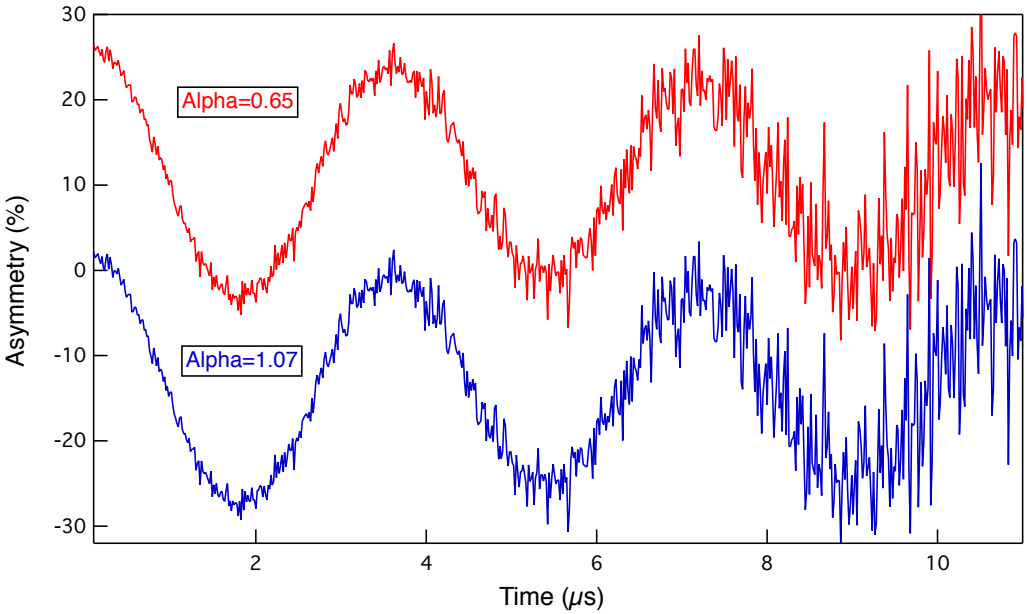

Figure 3.4: Incorrect alpha values. The two signals oscillate above (red) and below (blue) zero on the horizontal axis.

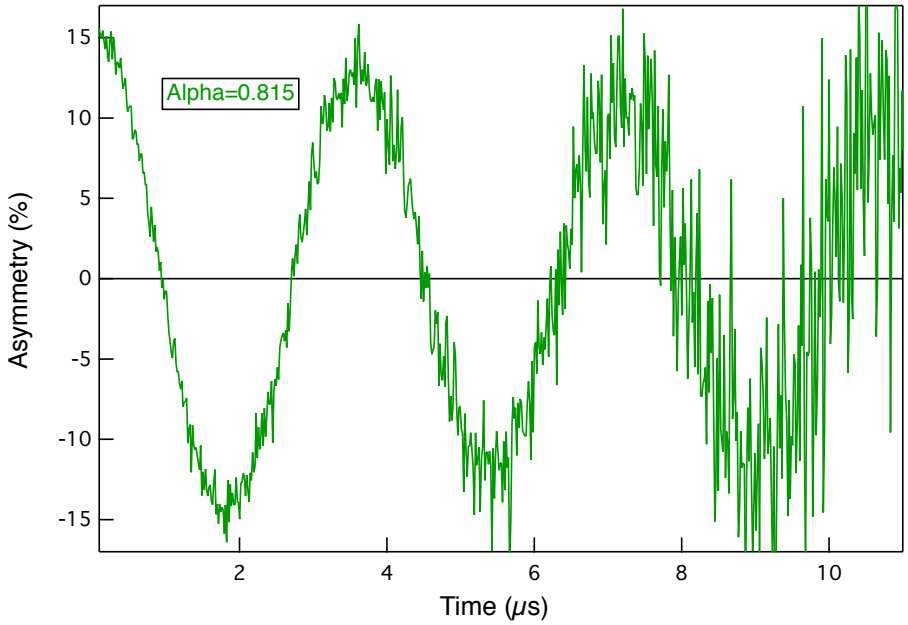

Figure 3.5: Correct alpha value. The signal oscillates symmetrically about zero on the horizontal axis.

The Asymmetry function can be written as $A_0(t) = a_{B,F}\, P_z(t) = A(t)$ which implies that $A(t) \propto P_z(t)$. This means that a measurement of the asymmetry function A(t), gives us

also information about about $P_z(t)$, a quantity that represents the spin polarization of the muon along the z axis of the experimental instrument.

3.2.4 Spin Precession and Relaxation Functions

In a μSR experiment, the spin of implanted muons precess around any local magnetic field **B** they encounter, with an angular frequency given by

$$\omega = \gamma_\mu \mathbf{B} \tag{3.8}$$

where $\gamma_\mu = \dfrac{ge}{2m_\mu} = 2\pi \times 135.5\ \mathrm{MHzT}^{-1}$ (see table 3.1) is the gyromagnetic ratio for the muon [4]. The asymmetry A(t) is usually given in the time domain, and the shape of the spectra is fitted by using what are known as *relaxation functions*. The form of a particular relaxation function is what reveals the intrinsic physics of the sample being measured.

Consider the semi-classical view of a muon spin precessing around a local field **B** which is at an angle θ to the initial direction of the muon spin, as shown in figure 3.6. We take the initial muon spin direction to be along the z axis.

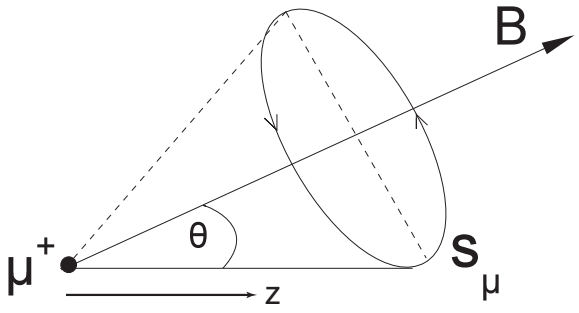

Figure 3.6: muon-spin precession about a magnetic field **B** applied at an angle θ.

The z component of the muon spin polarization $P_z(t)$ is therefore given by [4, 78, 80, 82]

$$P_z(t) = \cos^2\theta + \sin^2\theta \cos\left(\gamma_\mu \left|B\right| t\right). \tag{3.9}$$

where the first term corresponds to the average non-oscillating, time-independent polarization component along the z axis and the second term corresponds to the precessing component of the overall asymmetry. This is a very important result as it is this relation which the whole of the μSR technique is based on [82].

As mentioned in section 3.2.3, μSR experiments can be performed in a number of ways depending whether an external field is applied parallel or perpendicular to the initial muon spin direction, or with no applied field at all. In the following section, I shall describe each of the experimental geometries used in μSR, with emphasis on the Zero Field (ZF) geometry which is the one used on the experiments presented in this thesis.

3.2.5 Experimental geometries

Zero field μSR

Materials that possess intrinsic magnetic properties do not require any kind of external field for μ^+SR measurements to be performed. A material with a spontaneous magnetic ordering causes the implanted muon ensemble to precess about the internal field in accordance to equation 3.9. The samples considered in this thesis are all powder samples made of a very large number of crystallites which are all randomly aligned. For single crystals, equation 3.9 gives a good description of the behaviour of implanted muons due to the well defined set of axis within the sample. The fact that in a powder sample the crystallites are randomly oriented implies that the internal field direction is entirely random and therefore a *powder average* must be performed over all space.

An angular average taken over all space (over a sphere) for each component yields

$$\langle \cos^2 \theta \rangle = \frac{1}{3}$$

$$\langle \sin^2 \theta \rangle = \frac{2}{3}$$

and therefore, equation 3.9 becomes [4, 77, 78]

$$P_z(t) = \frac{1}{3} + \left(\frac{2}{3}\right)\cos(\gamma_\mu |B| t) \tag{3.10}$$

where the $\frac{1}{3}$ term corresponds to the crystallite orientations expected to lie parallel to the muon spin polarization ensemble at the moment of implantation. Magnetic ordering below a certain transition temperature can therefore be identified by the presence of oscillations as well as a $\frac{1}{3}$ tail at longer times, below which a relaxation can not be observed. Figure 3.7 shows an example of the asymmetry spectrum below T_N in a sample of $BiFeO_3$, a material that will be discussed in the following chapter.

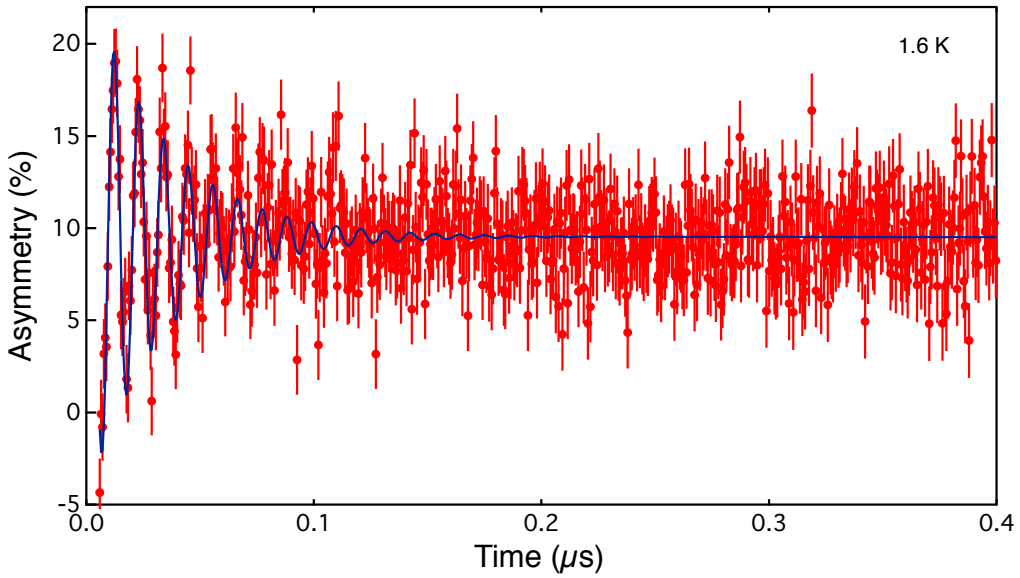

Figure 3.7: Asymmetry spectra obtained from a $BiFeO_3$ sample at 1.6 K, well below its magnetic transition temperature. The signal shows the expected behaviour, a damped oscillation at times $t < 0.4$ μs as a result of small variations in the local field with respect to the muon's site [4], and the 1/3 tail at longer times below which the data does not relax.

For a sample with a single muon site, or many magnetically equivalent muon sites, the signal will behave as an ordinary cosine function (in the case of static magnetism of course). A system where the field varies slightly from site to site causes different muons to precess at slightly different frequencies resulting in a progressive dephasing of the precessing spins of the muon ensemble which manifests itself in the data as a relaxing damped oscillation. If the field variation is too great the dephasing is such that no

oscillations are observed on the muon signal.

Random static fields in the muon site give rise to field distributions. If the strength of the static field is taken from a Gaussian distribution distributed about a mean of zero, then the muon polarization follows the well known *Kubo-Toyabe function* (KT),

$$P_{KT}(t) = \frac{1}{3} + \frac{2}{3}\exp\left(\frac{-\Delta^2 t^2}{2}\right)(1-\Delta^2 t^2) \tag{3.11}$$

where $\frac{\Delta}{\gamma_\mu} = \sqrt{(B - \langle B\rangle^2)}$ is the width of the distribution (the second moment of the distribution with mean $\langle B\rangle$). Figure 3.8a shows the origins of this distribution as a number of curves of equation 3.11 for different values of B. Initially, all the curves display the same behaviour, but after a short time the curves start to dephase relative to one another. This results in the KT function which shown in figure 3.8b. The KT function reaches a minimum at $\Delta t = \sqrt{3}$ and the $\frac{2}{3}$ oscillating component dephases entirely leaving the $\frac{1}{3}$ tail that corresponds to those muons with their spins lying parallel to the local field. The recovery of asymmetry to $\frac{1}{3}$ is, according to the Kubo-Toyabe theory, unmistakable evidence for random, static fields [83].

Materials with incommensurate magnetic structures, where the local field at the muon site oscillates sinusoidally within the unit cell where the muon is implanted, results in a field distribution that is described by a *Bessel Function* [84]. This relaxation function is used in this thesis to fit the muon data obtained from measurements made on a $BiFeO_3$ sample that will be discussed later in the following chapter.

Another way in which the muon ensemble can relax is by the presence of dynamics within the system. Spin fluctuations can result in an exponential relaxation of the form $e^{-\lambda t}$ where lambda is the relaxation rate.

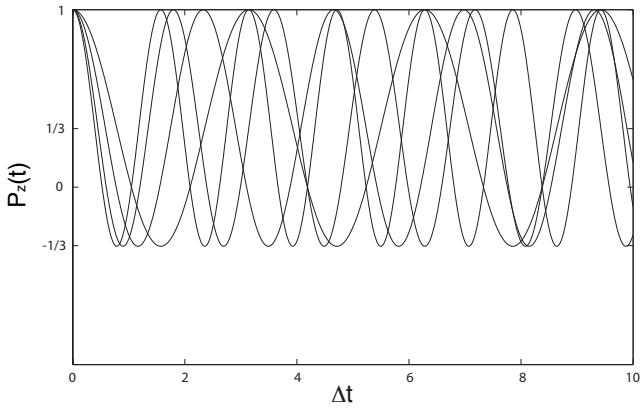

(a) Time evolution of the muon spin for different values of $|B|$

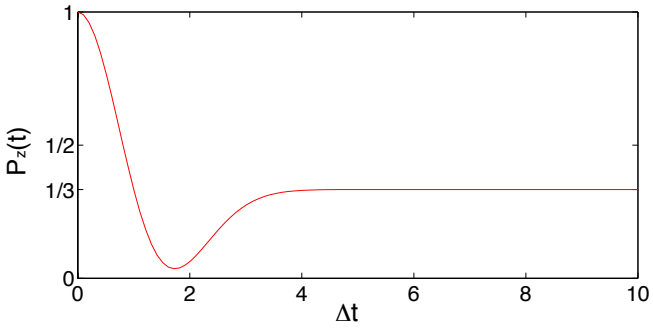

(b) Kubo-Toyabe function obtained by averaging all the curves in (a).

Figure 3.8: Kubo-Toyabe function

Longitudinal Field Geometry

A μSR experiment in the longitudinal field (LF) geometry implies the application of an external magnetic field parallel to the initial muon spin polarization, and it is referred as *Muon Spin Relaxation*. Assuming that the applied external field is larger than the internal local field of the sample (so that any competing factors are absent), implanted muons with 100% spin polarization retain their spin state. The focus of this type of geometry is on the form of the relaxation function describing the spin depolarization as a function of time [77]. Usually, in LF experiments the positron asymmetry is measured using the forward and backward detectors with respect to the initial polarization of the muons, as shown in figure 3.10. The asymmetry in this case does not display the oscillatory behaviour that is observed in other experimental set ups (such as transverse field geometry). Instead, the asymmetry shows an exponential decay that is described

in terms of relaxation functions. Note that the fact that in a LF geometry the field is applied parallel to the muon spin direction might naively lead to the conclusion that all the events should be recorded in the back detector. In some systems, however, (such as magnetic systems) spin fluctuations cause some of the muons to relax (lose their initial spin polarization), and the decayed positron to be recorded in the front detector. The majority of the events however, are consistently recorded in the back detector as is to be expected with a LF set up.

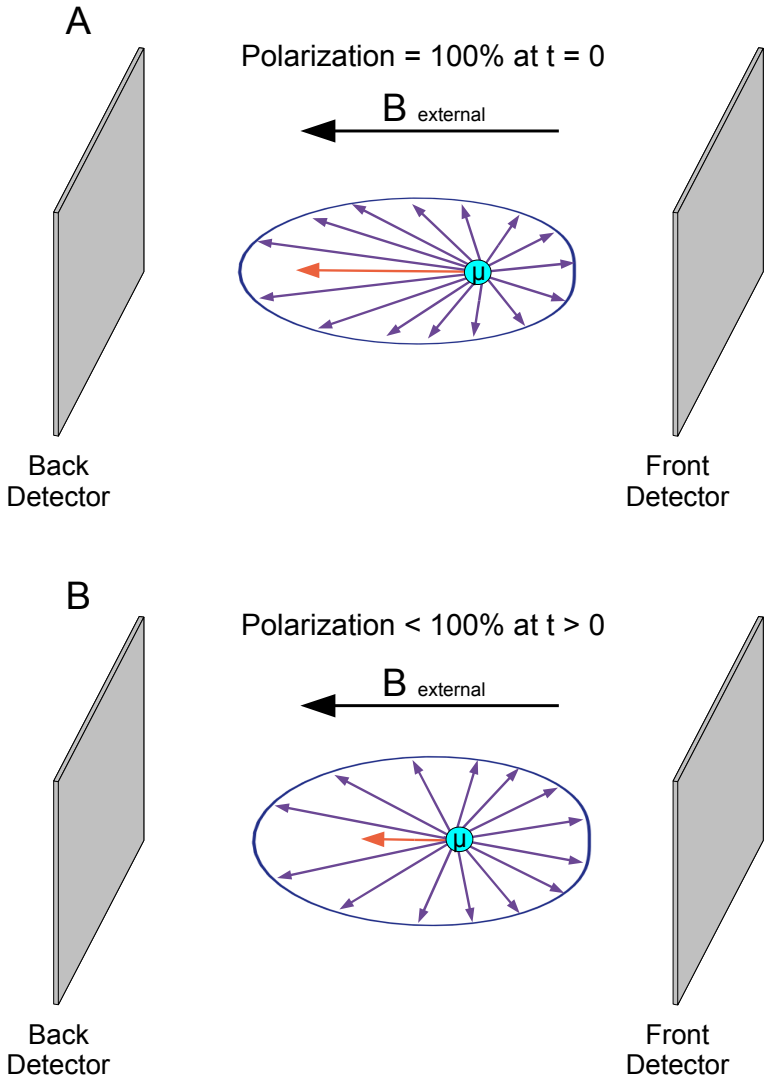

Figure 3.9: The sketch shows the Longitudinal field configuration with an external field applied parallel to that initial muon spin polarization. A) Muons with their spin 100% polarized are implanted in the sample at t=0. When they decay, the emitted positrons are mostly recorded on the back detector. at longer times however, some of the muons lose their spin polarization (represented in the sketch as a shorter orange arrow) and events are also recorded in the front detector.

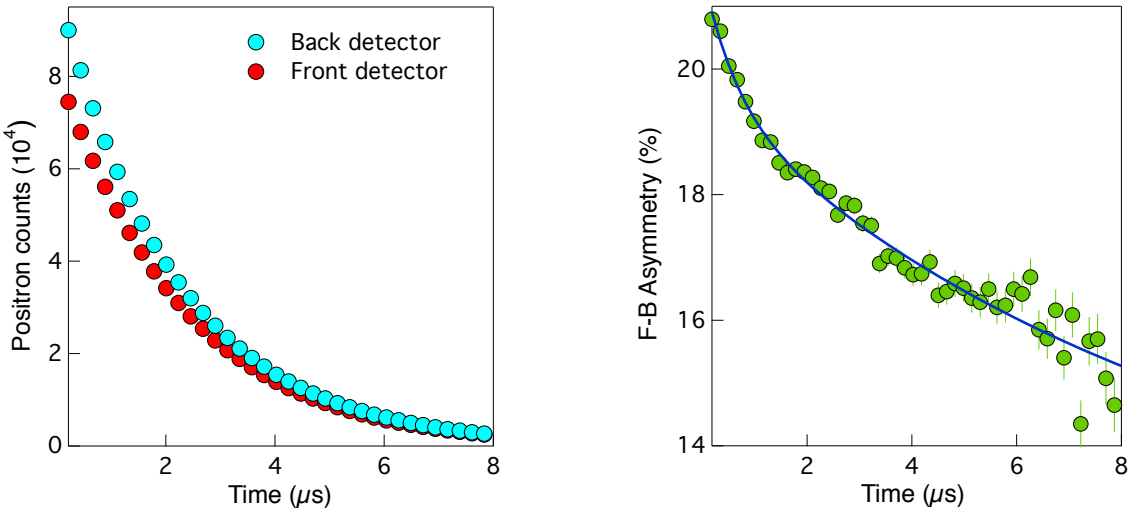

(a) (b)

Figure 3.10: a) Positron count as a function of time. As expected, the positron count on the back detector is consistently higher that on the front detector. The reduction in number of event in each detector is the result of the finite muon lifetime. b) The asymmetry A(t) as a function of time. No oscillations are observed, just the relaxation of the signal.

The Asymmetry can therefore take the form of a relaxation as

$$A(t) = G_z(t) \tag{3.12}$$

where $G_z(t)$ represents the longitudinal relaxation function, and can be extracted via a sum and difference ratio (equation 3.7) between the two detectors

$$G_z(t) = \frac{P_z(t)}{P_z(0)} \propto \frac{N_B(t) - N_F(t)}{N_B(t) + N_F(t)} \tag{3.13}$$

Figure 3.10 (a), shows a plot of positron counts versus time for each of the two detectors in an applied LF of 30 G. The asymmetry function $A(t)$ can then be calculated from the number of events in each detector (equation 3.7). The Asymmetry for this particular example is plotted in figure 3.10 (b).

Transverse Field Geometry

In a transverse field (TF) experiment, an external field is applied perpendicular to the initial direction of the muon spin. As a result, the muons precess about this applied field with a frequency $\omega = \gamma B$, where γ is the gyromagnetic ratio of the muon and B is the applied field. Muons implanted on a sample with no internal activity would yield a cosine function in the data. In real samples however, the frequency of the cosine function would undergo a small change regulated by a relaxation which would itself be dependent on the physics of the sample being measured. As a result, the general transverse field TF relaxation function has the form

$$A(t) = a_0 \, Cos(\omega t + \phi) \, G(t) \tag{3.14}$$

where a_0 is the initial asymmetry, ω is the angular frequency of the oscillation, ϕ is the phase between the initial spin direction of the muon and the principle axis of the detector and $G(t)$ is the function describing the relaxation. The configuration of the TF geometry is shown in figure 3.11 where various stages of precession are shown. Figure 3.12 shows a plot of positron counts versus time, and it reveals the muon spin precession pattern shown in figure 3.11. For magnetic materials, the behaviour of the muon signal under an applied TF depends on the magnitude of the applied field relative to the internal field of the sample. In the limit of small applied fields, the internal field of the sample significantly affects the spin behaviour of the muons and hence, the total field sensed by the muons must be taken as a vector sum of the internal and applied fields. In the case of a large applied field, the applied field becomes dominant and the relaxation function can be described as a cosine function with a frequency $\omega = \gamma \, B_{trans}$. As well as magnetism, the transverse field geometry is widely used in the study of superconductors [85]. Figure 3.13a shows the recorded positron events for the back and front detectors with a 180° phase shift with respect to one another revealing the oscillation of the muon spin. In figure 3.13b the asymmetry is plotted as a function of time.

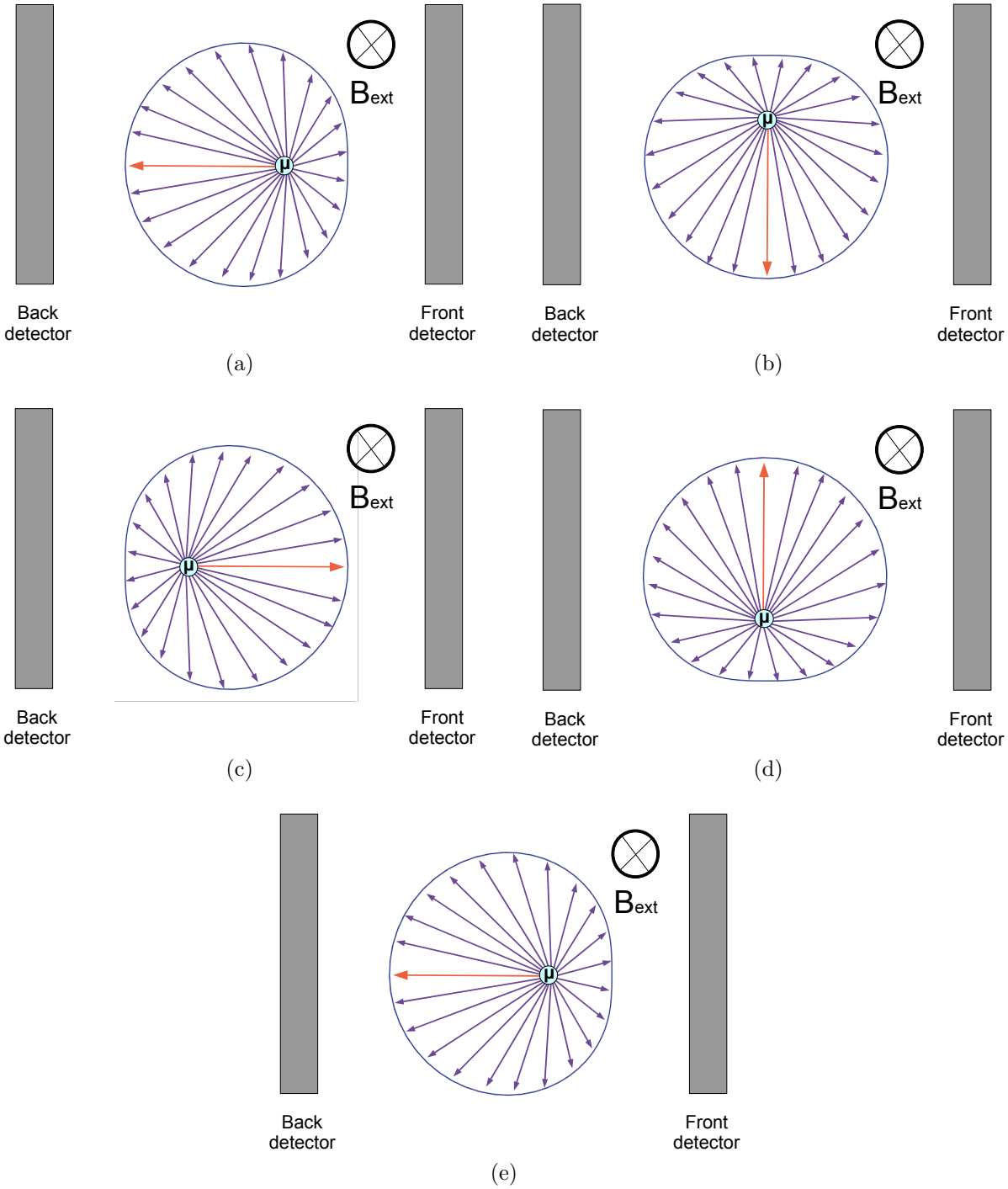

Figure 3.11: a)-e) Evolution of the muon spin as a function of time under an applied transverse field. The sketch shows the muon precession around an applied magnetic field perpendicular to the initial muon spin direction. Figure 3.12 shows the positron count in each detector of the two detectors at the stages of the precession shown in this sketch.

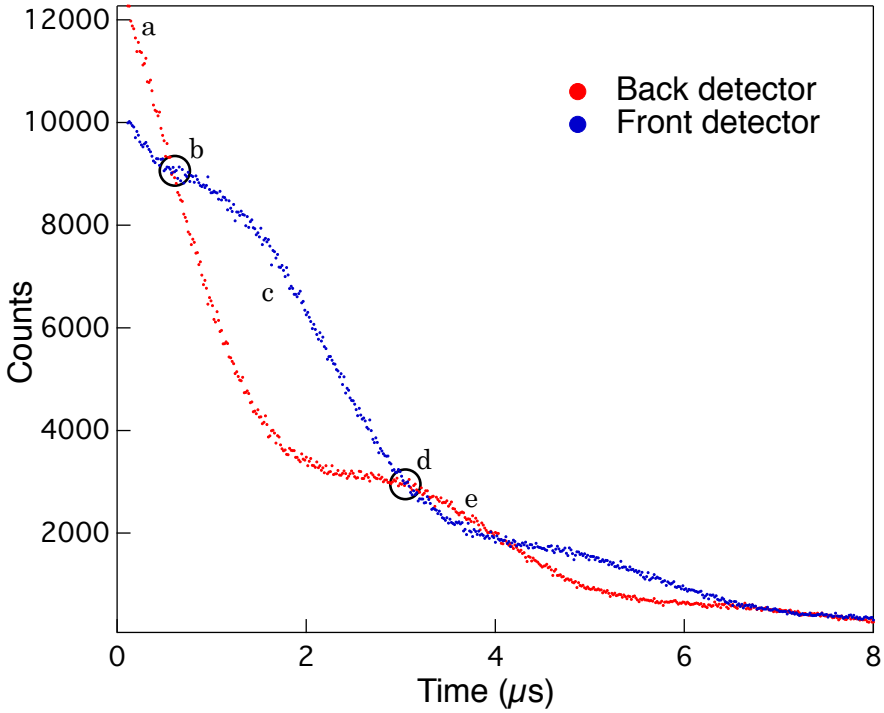

Figure 3.12: Plot showing the positron count in the front (blue) and back (red) detectors under and applied transverse field. The letters on the plot indicate the stages of precession shown in figure 3.11. After the muon is implanted, At t=0 the muon spin points towards the back detector and as a result, more events are recorded on it as shown in **a**. At stage **b**, the two lines intersect as a result of the muon spin pointing away from the two detectors. At **c**, The muon spin points towards the front detector and more positron counts are therefore recorded on it. Just as in **b**, at **d** the muon spin once again points away from the detectors causing the two lines to intersect again. Finally at **e**, the muon spin direction is back where it started giving more positron counts on the back detector.

3.3 Muon sources

Muon sources can be divided into two main categories: Pulsed sources, where muons arrive in the sample in large bunches of finite length, and continuous sources, where muons are fired into the sample in a continuous stream and there is only a single muon in the sample at any given time. In this section, I shall describe the different muon sources and the advantages and disadvantages associated with each one of them.

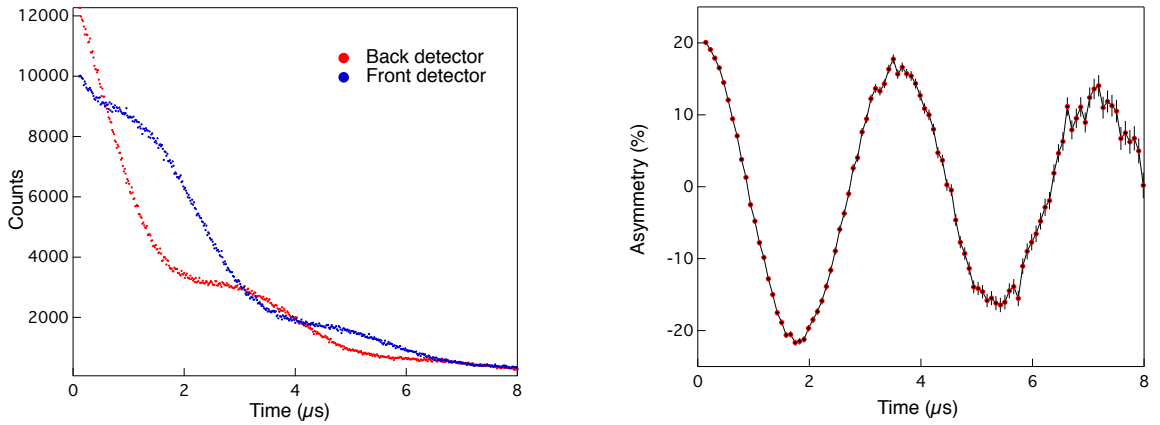

(a) (b)

Figure 3.13: a) Plot of positron counts as a function of time for the front and back detectors in the transverse field configuration. The plot shows the oscillations associated with the positron counts as well as the 180° off-phase shift consistent with the detector configuration. b) The asymmetry A(t) as a function of time for TF geometry. As expected, the signal behaves as a cosine function. after about 8 μs the relaxation of the signal can be observed.

3.3.1 Pulsed beam sources

In a pulsed muon source the muons are directed to the sample area in large bunches and are implanted in the sample almost simultaneously. The experimental clock starts once the muons arrive and the data acquisition starts when the middle of the muon pulse has entered the sample. The positron count is timed relative to the arrival of the whole muon pulse.

A key disadvantage of a pulsed muon source is the resolution limits when measuring the precession frequencies of the muons within the pulse. The fact that the muons arrive in the sample as a pulse implies that when the first muons arrive in the sample, by the time the last muons enter the sample, the first ones have already undergone a full rotation while the ones in the middle of the pulse are half way through their precession and any signal coming from it will be eliminated. For a single broad pulse, a progressive reduction in the amplitude signal occurs until eventually, at some cut-off frequency the muon precession can no longer be reliably resolved. In other words, if the muon spin precess too quickly relative to the time resolution of the instrument, then the oscillation will no longer be observed and the overall muon spin polarization will be averaged out to

zero.

Despite of such restriction, it is still possible to determine whether a system has gone thorough a magnetic phase transition into a long-range magnetic ordering where the muon precession frequency is just too high to be observed. After the phase transition, if no oscillations are observed in the signal, a drop in the initial asymmetry is expected from a_0, down to $\frac{1}{3}a_0$. Also, an increase in the asymmetry can be observed sometimes as a result of the 1/3 tail at longer times in the muon signal.

The rate at which data can be acquired at a pulsed source is limited by the detector *dead time*. When running an experiment, after a detector records a positron count there is a small interval of time (usually $10\mu s$) before it is able to record another event. It is therefore possible that another positron will arrive at the detector within this this time interval and not be recorded. As a consequence, instead of using two detectors, a large number of individual detectors are used to minimize this effect. For the longitudinal field geometry, large numbers of these detectors are grouped together in banks to act as two segmented detectors. Facilities that provide pulsed muon beams include the ISIS laboratory (United Kingdom) and the KEK Meson Science Laboratory (Japan).

The EMU spectrometer

Most of the experiments in this thesis have been performed in the **EMU** spectrometer at ISIS. This spectrometer consists of 96 individual detectors split into two banks of 48. It is optimised for studies in zero field and longitudinal field. The instruments also consists of magnets that can provided applied fields of up to 0.45 T and it can produce sample temperatures in the range of 50 mK to 1500 K [86].

3.3.2 Continuous beam sources

In continuous sources, one muon is in the sample at any given time. Muons continuously arrive in the sample separated by small time intervals of about 29 μs (on average). It is possible for some of the muons to miss the sample. In this case, a backward veto

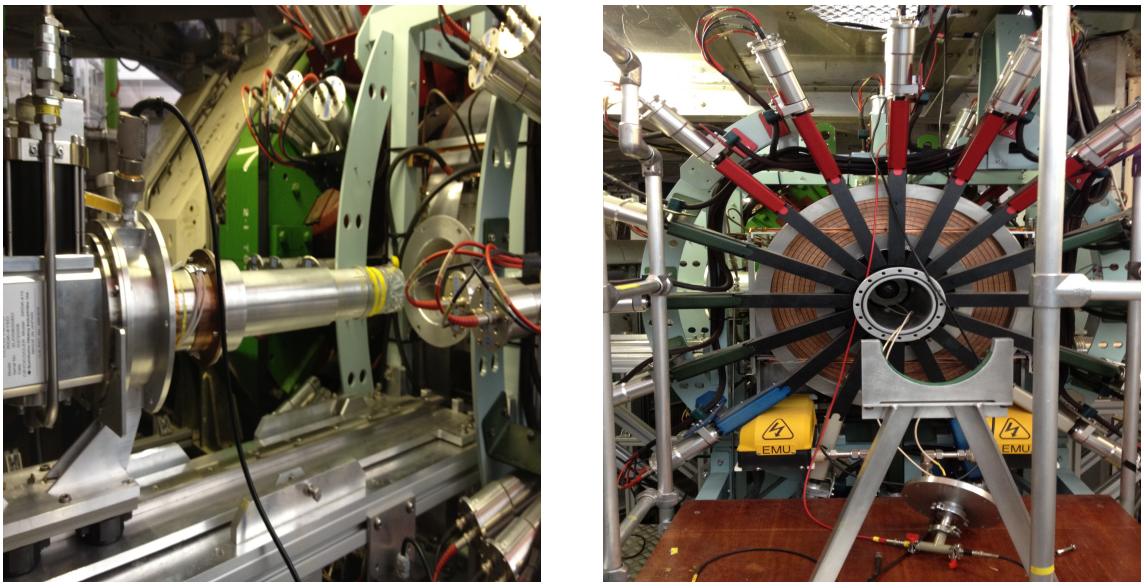

(a) (b)

Figure 3.14: a)EMU sample set up area. b)The EMU spectrometer showing some of the detectors and the main magnet coils.

detector is used to reject events coming from muons that have missed the sample and are implanted elsewhere. A forward veto detector can also be used to reject muons that do not stop in the sample, something which can occur in small samples. If all of the muons are implanted in the sample, the forward veto detector can be added to the forward detector to increase the forward solid angle. In a continuous beam the time implantation of the muons and the time of the muon decay (detection of the positron) have to be correlated and accurately determined. To achieve this, an arriving muon is detected by a muon counter which starts a clock that is stopped once the decay positron reaches the detector. Although this time interval can be determined with great accuracy, if another muon arrives in the sample within this time interval then there is no way to know from which muon the decay positron actually came and as a result, both the events must be discarded.

The fact that only one muon can be implanted in the sample at any given time, implies that the event rate and the low frequency resolution are restricted. If the rate of muon production is increased in order to increase the positron count rate, the probability of a muons arriving in between events and stop the experiment will also increase, meaning

that many events will have to be discarded. If, on the other hand, the time window for every event is increased in order to increase the low-frequency resolution, this will also result in a higher probability of new muons arriving between time intervals to stop the experiment. These two experimental parameters are therefore in competition with one another. Another disadvantage of a continuous source is the high background as a result of muons which are either not implanted in the sample or do not trigger the veto detector, which can off course result in false counts, especially at longer times. As a result, there is a limit on the experimental counting which is typically around $10\mu s$.

The basic differences between pulsed and continuous sources can be summarised as follows: The time resolution that a continuous muon source (such as the one in PSI, Switzerland) can provide in the time-differential technique, is less than 1ns while at a pulsed muon source the time resolution is limited by the pulse width (at ISIS, the pulse width is 70 ns). In a continuous source, information about very fast relaxation rates that at a pulsed source would remain hidden, may be obtained. Also, very high frequencies may be resolved at a continuous source. In contrast, pulsed sources can provide very large muon rates with very low contribution from background signals, which provides access to longer times and therefore, a way to investigate slow relaxation rates and slow frequencies.

Facilities that provide continuous muon beams include the Paul Scherrer Institute (Switzerland) and the TRIUMF Meson Facility (Vancouver, Canada).

The GPS Beamline

The General Purpose Surface instrument (GPS) at PSI (shown in figure 6.25), consists of five positron detectors: up, down, forward, backward and right. Since it is a continuous source, large numbers of individual detectors grouped in banks are not required, such as in the case of ISIS. The forward detector in this instrument can also be used as a *veto* detector, to discard those muons that fly past the sample. In this case(veto mode), the forward detector area is smaller causing a decrease in event rate, but allowing the study of small samples.

Experiments in transverse field (TF) mode, require a change of the spin directions of incoming muons which is achieved by a spin rotator, where an overlapping magnetic and high electric field, are used. The magnetic field is used to rotate the spin of the muon while the electric field maintains the momentum of the muon constant. In TF experiments, the up, down and right detectors are used. The instrument also consists of two different magnets which can be configured for any experimental geometry needed. The instrument allows measurements in a temperature range 1.6 K to 320 K.

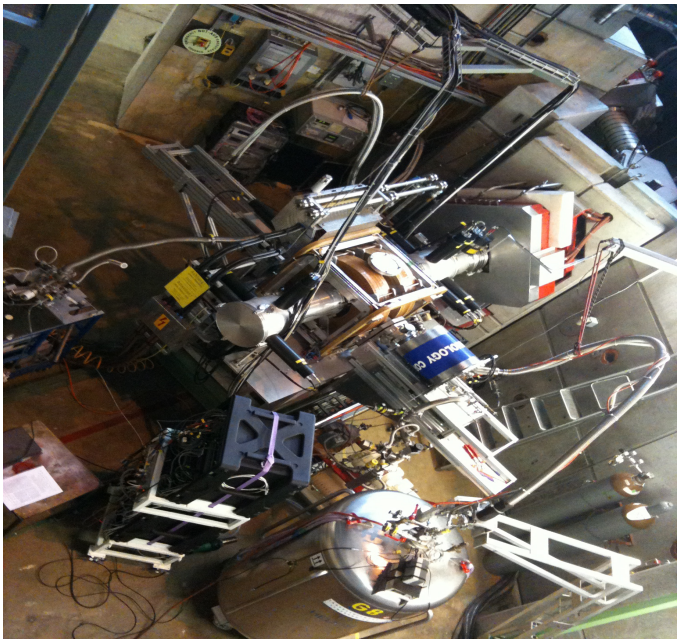

(a)

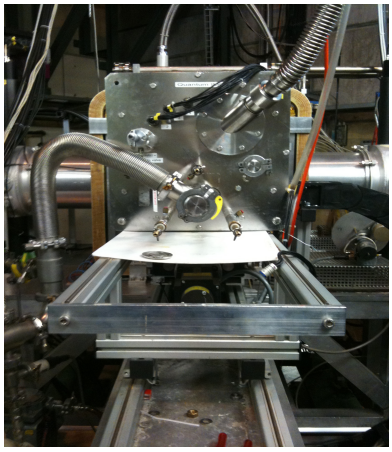

(b)

(c)

Figure 3.15: a) The General Purpose Surface (GPS) instrument. b) Sample area. c) Detector arrangement

Chapter 4

Complementary techniques

Most of the work in this thesis is based on muon measurements on multiferroic materials. However, other techniques have been used in order to corroborate the muon results and check whether results are in agreement with each other. Two of the techniques we have used are *Neutron Diffraction*, from which information about magnetic properties and spin configuration of the material being measured can be obtained, and *Resonant Ultrasound Spectroscopy*, a technique from which the elastic properties of the material can be determined. Both of these techniques are extensively used in the study of multiferroics, in our case, we use them in order to compare the results we obtained from our muon measurements. In this chapter I shall give a brief description of these two complementary techniques.

4.1 Neutron diffraction

Neutron diffraction is a technique widely used in condensed physics to investigate the internal structure and other physical properties of crystals. Neutrons are unstable subatomic particles with no electric charge and a mass $m_N = 939$ MeV/c^2. In a neutron scattering experiment, the neutrons are treated as waves with wavelength λ_{DB} as given by De Broglie's relation

$$\lambda_{DB} = \frac{h}{P} \tag{4.1}$$

where h is the Planck's constant and P is the momentum of the neutron. The fact that the wavelength of neutrons is comparable to that of the interatomic distances within a crystal, allows for diffraction to occur and the atomic structure of a crystal to be determined [30]. Neutrons can be scattered from atomic nuclei via the strong nuclear force, or from changes in the internal magnetic field within a crystal as a result of electromagnetic interactions . For this thesis, I shall focus on the latter. Even though the neutron has zero electric charge, it possesses a non-zero magnetic moment that is scattered by the magnetic moments of electrons.

In general, all diffraction techniques are sensitive to the symmetry of a material, and since magnetic ordering reduces the symmetry of the material in the ordered phase the diffraction pattern of the material above and below the magnetic transition temperature looks different. In the case of an antiferromagnet, the diffraction pattern above the Neel temperature (T_N) differs from the diffraction pattern below T_N.

When neutrons are scattered by atoms within a crystal, their wavelength λ, obey the Bragg equation which is given as

$$n\lambda = 2d\,sin(\theta) \tag{4.2}$$

where d is the separation between adjacent planes of atoms. Neutrons within an incoming beam are scattered in all directions by atoms within each lattice plane of a given sample, and although most of the scattered neutrons interfere destructively diffraction peaks are observed when the interference is constructive, something that occurs when the path difference between two scattered beams is an integer number of wavelengths. In other words, diffraction only occurs in the directions given by the Bragg condition [13]. The geometry for Bragg diffraction is shown in figure 4.1. Because of the symmetry of the crystal however, a diffraction pattern may contain less peaks than those predicted by the

Bragg equation.

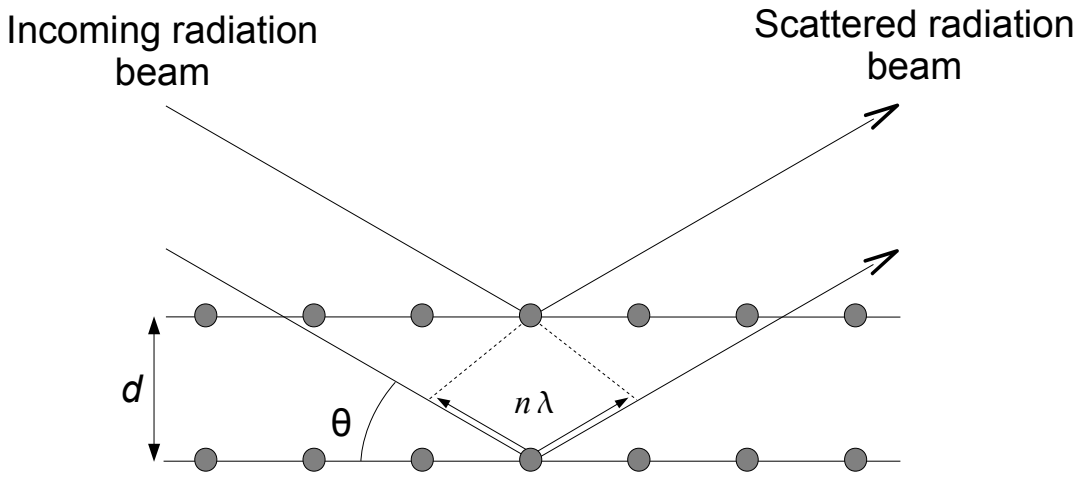

Figure 4.1: Geometry of Bragg scattering from two adjacent planes of atoms.

To illustrate this point, consider as an example the scattering of a beam of neutrons from a body-centred cubic lattice, as shown in figure 4.2 (this example is taken from reference [13]). The figure shows a set of planes containing the atoms that make the unit cell. Planes (1) and (3) correspond to the (100) planes which contain the atoms at the corners of the unit cell, and plane (2) which is the middle plane containing central atom of the body-centred cubic lattice.

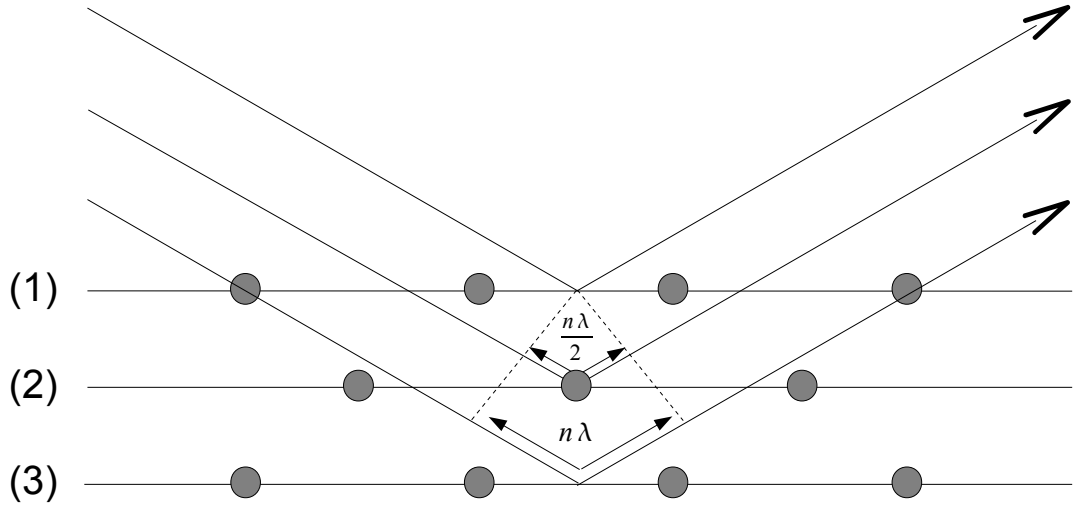

Figure 4.2: Bragg Scattering in a Body - centered cubic lattice.

For the sake of the argument, we assume that the planes (1) and (3) satisfy the Bragg condition meaning that the orientation of the crystal is such that neutrons scattered from

these planes will be in phase with one another and will therefore generate Bragg peaks. The fact that they are in phase implies that the difference between the neutron beam scattered from planes (1) and (3) has to be an integer number of wavelengths, nλ, as given by equation 4.2. But the difference in distance between neutrons scattered from plane (2) and either plane (1) or (3) is exactly $\frac{1}{2}$ the distance relative to planes (1) and (3) which also implies a half-integer number of wavelengths n$\frac{\lambda}{2}$. This means that the reflections from planes (1) and (2) (or (2) and (3)) will be exactly out of phase with respect to each other. Therefore, the scattering from these planes interfere destructively and the (100) peak cannot be observed.

If, however, the atoms within plane (2) are different from those in planes (1) and (3) the scattering intensities between the atoms in plane (2) and the atoms in planes (1) and (3) will be different and as a result the scattered neutrons will no longer interfere destructively. In such a case, the (100) peak will also appear.

This idea of different species giving different scatting amplitudes is the basis of magnetic neutron scattering. For magnetic materials, different orientations of the magnetic moments result in different scattering intensities. A material with an antiferromagnetic order, will display different diffraction patterns above and below the Neel temperature. Above T_N, the diffraction peaks will be structural peaks (Chemical unit cell) and below T_N the unit cell doubles and extra peaks will appear as a result of the onset of magnetic ordering (magnetic unit cell).

Going back to the example of figure 4.2, and assuming the atoms to be of the same species (so that above T_N the peak corresponding to the (100) plane cannot be observed) if below T_N, the moments of the atoms on the system order such that the ones on planes (1) and (3) are all spin up and the ones on plane (2) are all spin down, the scattering amplitudes will be different and the (100) will be observed. Because of this, the neutron diffraction pattern displays additional Bragg peaks when a material is cooled down below the Neel temperature. This extra peaks indicate that the material has ordered magnetically and they are known as superlattice peaks. Figure 4.3 shows the unit cell for a material above

and below the Neel temperature.

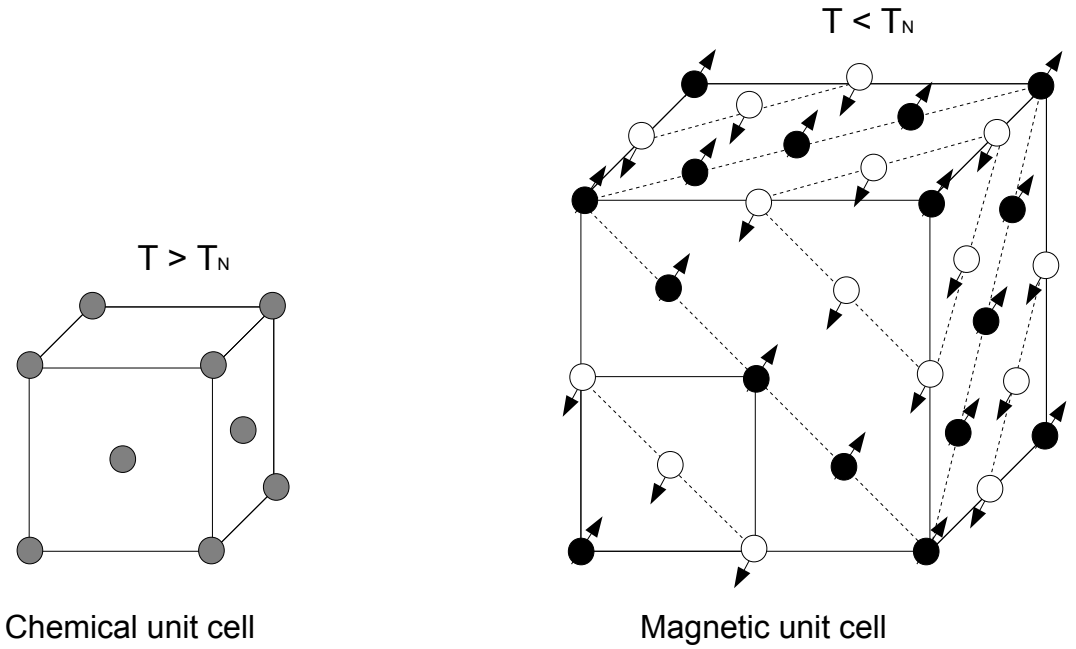

Figure 4.3: Structure of an antiferromagnetic material with a fcc unit cell above (chemical unit cell - left) and below (magnetic unit cell - right) T_N.

4.2 Resonant Ultrasound Spectroscopy

The Resonant Ultrasound Spectroscopy technique (RUS) is one of the most useful experimental methods for determining how the elastic properties of a material behave as a function of temperature. In a RUS experiment, the mechanical resonance frequencies of a sample of well defined shape (usually a parallelepiped) are measured in a frequency region $\sim 0.1 - 2$ MHz [87]. The information obtained from this measurements can then be used to determine elastic constants and mechanical dissipation of the material under study. Samples can be either polycrystalline or single crystals, and the experiments can be carried out in a temperature range of ~ 5 K $-$ 1800 K. Figure 4.4 shows a typical RUS experimental set up.

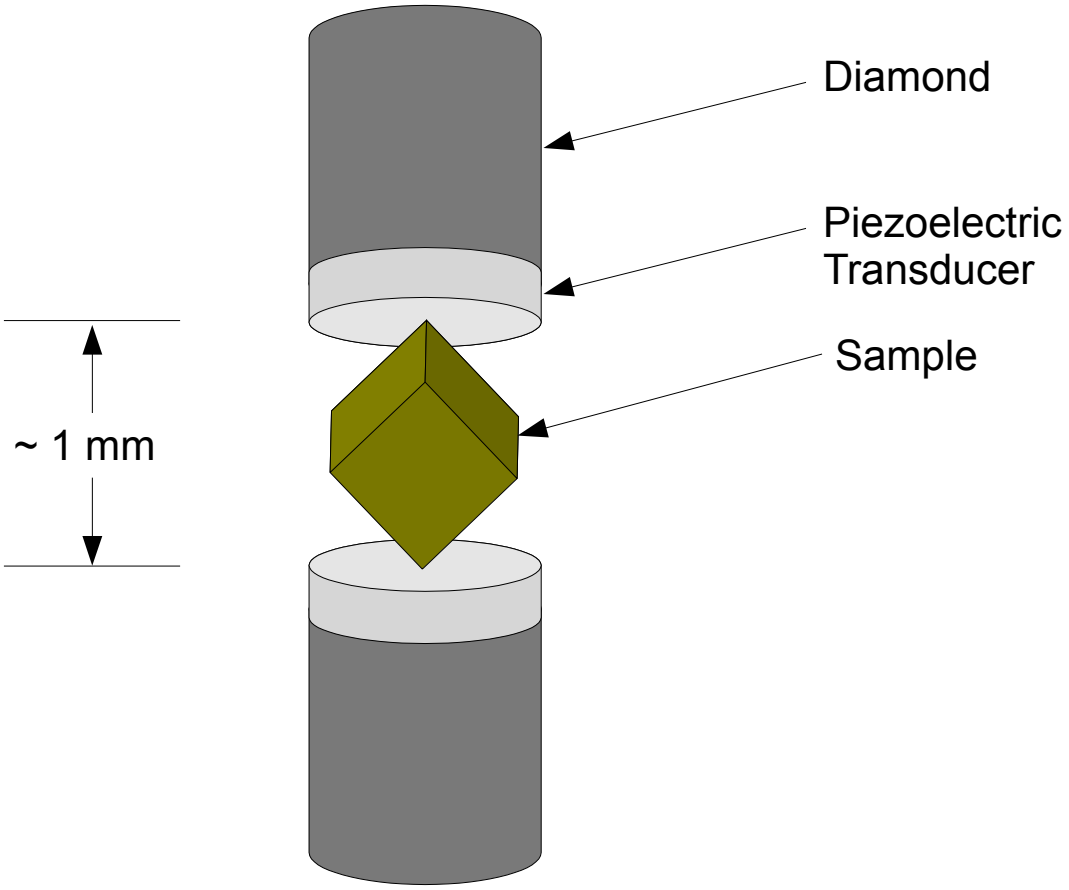

Figure 4.4: A typical RUS experimental arrangement.

As shown in the figure, a sample is placed in between two piezoelectric transducers. One of the transducers (the driving transducer) is then made to vibrate in order to excite the sample while the other detects the response of the sample to the vibration. As mentioned above, the transducer vibrates through a range of frequencies and these frequencies correspond to many vibrational eigenmodes of the sample. When the vibrational frequency of the driving transducer matches one of the sample resonant frequencies, a large response is observed in the spectrum. Resonant frequencies of a sample depend on quantities such as the elastic constants, shape, orientation of the crystallographic axis relative to the sample and the sample's density [88]. A measurement of many resonant frequencies of a sample may yield information about all these quantities. For a RUS experiment, it is usually necessary to have a complete characterisation of the sample under study. Quantities such as composition, structure and lattice parameters are essential to accurately interpret the RUS data, and since the RUS method alone cannot be used to determine

these quantities it is important to have a sample that is fully characterised with other experimental methods before performing the measurements.

For polycrystalline materials (such as the ones considered in this thesis), RUS can be used to determine values of the bulk (K) and shear (G) modulus of the material. Both of this quantities describe the elastic behaviour for of a polycrystalline sample. K is a measure of how resistant a material is under uniform compression, while G is a measure of the material's resistance to shear stress [87]. In a RUS spectrum, the resonant frequencies of the sample are identified as peaks, as shown in figure 6.22. The square of a particular frequency of any peak within the experimental spectrum scales linearly with the elastic constants. As a result, information about the evolution of the elastic constants of a material can be extracted directly from variations of resonance peaks as a function of temperature.

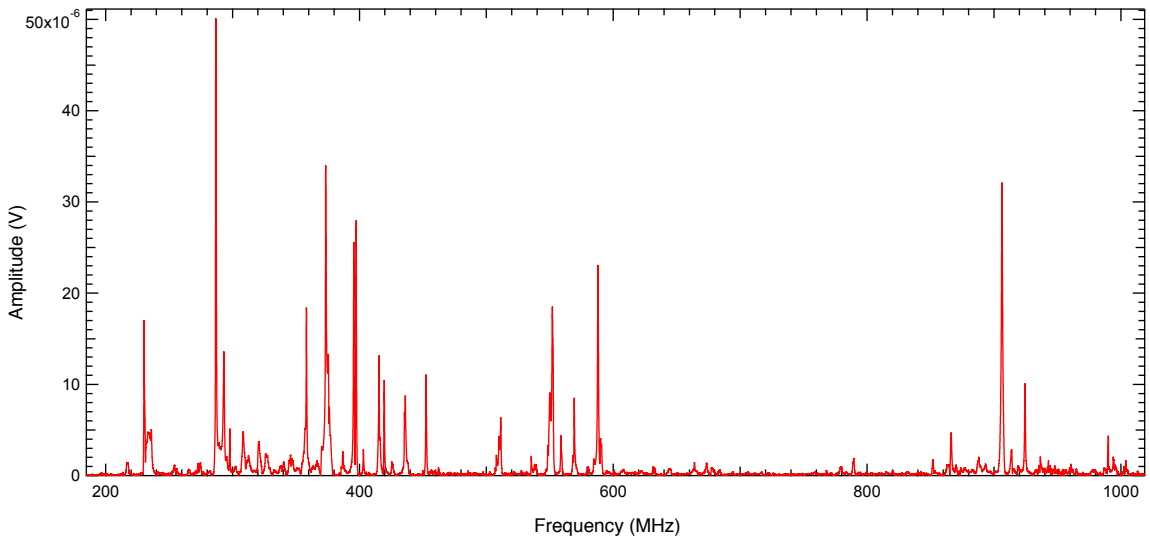

Figure 4.5: A typical RUS experimental spectrum. The sample is an irregular fragment of $Ba_{4.32}Dy_{0.68}Ga_{0.13}Nb_{9.87}O_{30}$ which is measured at $\sim$ 400 K in a frequency region 200 - 1000 MHz. The peaks in the spectrum correspond to the resonant frequencies of the sample.

Another quantity of interest that can be determined directly from an RUS spectrum, is the mechanical quality factor Q, which is a measure of anelastic dissipation. This quantity can be determined by measuring the full widths at half maximum (FWHM) of the peak resonances in order to determine the mechanical dissipation (internal friction or

loss) for every resonance. In order to determine these values, every individual peak must be fitted by using an asymmetric Lorentzian function of the form

$$a(f) = a_0 + \frac{A}{(f - f_0)^2 + B} \tag{4.3}$$

where $a(f)$ is the amplitude, a_0 is the baseline (taken to be a straight line), f_0 is the peak maximum (resonant frequency) and A and B are constants. The ratio $\frac{A}{B}$ correspond to the maximum amplitude.

The quality factor Q can then be calculated from

$$Q = \frac{f_0}{\Delta f}, \tag{4.4}$$

where Δf is the FWHM, which is obtained from the fitting process.

The acoustic dissipation within the sample can then be measured by taking the inverse of the quality factor, Q^{-1}. By plotting Q^{-1} as a function of temperature, a picture of any relaxing mechanisms in the system (ie. mechanical losses) can be constructed. Mechanical energy losses (dissipation) within a sample, is manifested in the data as a peak in Q^{-1}. Peaks are usually observed at phase transition temperatures. In general, Q^{-1} is equivalent to $\mathrm{Tan}\,(\delta)$, which is a measurement of the dielectric loss of a sample.

Chapter 5

Experimental results: Bismuth Ferrite

5.1 Overview

Research on multiferroic materials has attracted a lot of attention in the last decade, as a result of the great potential these materials have for device applications such as data storage, spintronics and microelectronic devices (among others), as well as the fascinating physics behind the coupling mechanisms between different order parameters [89, 90]. Bismuth ferrite (with chemical formula $BiFeO_3$) is by far the most widely studied multiferroic, mainly because the onset of both its magnetic and ferroelectric ordering, occurs well above room temperature, which is in turn one of the most important requirements for this class of materials to ever find useful device applications. Despite the large number of studies made on the compound, there are still a number of questions and disagreements in the literature regarding the material's magnetic, ferroelectric and structural properties [27].

In terms of the magnetic properties, which is the property of interest in our work, a number of low temperature magnetic phase transitions have been reported. Evidence of these transitions has been given in the form of magnon peaks in raman spectra for exam-

ple. Cazayous et al. first reported a magnetic transition at 140 K [91]. Independently, Singh et al. obtained consistent results as they found the same transition at 140 K and apparently a stronger one at 200 K [92]. The origin of the magnon peaks is not clear, but is was suggested that these anomalies could be related to sublattice spin reorientation below the Neel temperature, analogous to the known transitions in other magnetic orthoferrites such as $ErFeO_3$ [93, 94]. Another possible explanation for the magnon peaks is that they are related to spin-glass behaviour [95, 96]. There is a clear difference between zero field cooled and field cooled magnetization measurements beginning at 230 K, with the presence of an Almeida-Thoules transition line (which describes the stability of a spin glass at finite temperatures and magnetic fields) with an extrapolated end-point of 140 K [95]. A cusp has also been observed in the magnetic AC susceptibility [96], which corresponds to the freezing temperature T_f and is both, temperature and frequency dependent. If this is indeed the case, then $BiFeO_3$ would be an example of a rare (perhaps unique) spin glass that is ferroelectric and hence non-centrosymmetric [27]. Additional magnon cross-section divergences near 90 and 230 K have been observed, and changes in the dielectric constant at 50, 140 and 215 K, as well as anomalies at ~ 30 K [97] are also reported.

In summary, there are six cryogenic anomalies that have been found by means of a large number experimental techniques at $30, 50, 90, 140, 201$ and 230 K. However, these anomalies have all remained controversial, as bulk magnetometry and specific heat measurements have failed to show consistent results [26] and also, neutron diffraction experiments show no indication of any magnetic transitions, with apparently no change in the spin cycloid down to 4 K [98, 99]. In terms of surface effects on $BiFeO_3$, impedance analysis and grazing incidence x-ray diffraction measurements, have revealed that the surface layer of $BiFeO_3$ has a surface-confined phase transition and it was suggested that some of the low temperature anomalies found may actually be confined to the skin layer of the material [100]. Recently, a combination of a wide variety of experimental techniques, including Raman spectroscopy, resonant ultrasound spectroscopy, electron paraelectric resonance, x-ray lattice constant measurements, conductivity and dielectric response and

specific heat and pyroelectric data, the transition at $T \sim 140$ K was confirmed to be a surface phase transition [26]. The main features of this transition include a sharp volume change without actual change of symmetry, a sharp pyroelectric - like current at 140 K and maximum in conductivity consistent with a crossover between structural and magnetic disorder at the surface. Furthermore, the authors suggest that the magnetism probably has a a glassy state between 140 and 230 K.

It is clear that not all of the anomalies have been accounted for and there is still a significant number of open questions regarding their origin. To the best of our knowledge, all the work reported so far has been limited to bulk averaging techniques, such as neutron diffraction or magnetisation measurements, or surface sensitive techniques such as the ones discussed above. In this work, we have performed a combined μSR and neutron total scattering study in order to have a better understanding of the *local* structural and magnetic properties of this multiferroic. Contrary to what recent studies have suggested, namely, that the anomalies in the region of 200 K could be related to surface effects rather than bulk, our investigation, which is based on local probe techniques, has shown that there is an as yet undiscovered *bulk* local structural change causing these anomalies.

In the following sections, I shall first describe the structural, ferroelectric and magnetic properties of $BiFeO_3$, followed by a detailed description of our muon and neutron total scattering results.

5.1.1 Structural information of $BiFeO_3$

Not only have the magnetic properties of $BiFeO_3$ generated so much controversy among several groups investigating the material, but its structural properties and the different phases it displays as a function of temperature have also been the subject of debate and disagreement among many different groups. In this section, I shall give some key information about the structural properties of BFO, as well as a brief summary of some of the disagreements in the literature.

Figure 5.1 shows the unit cell of $BiFeO_3$, with the green spheres representing the bismuth

ion at the corners of the perovskite structure, the blue spheres the Fe ions and the red are the oxygen ions at the corners of the octahedra cage.

The crystal structure of $BiFeO_3$ at room temperature (RT) is rhombohedral, belonging to the space group R3c [101]. The lattice parameters of the perovskite-type unit cell are $a_{rh} = 3.965$ Å with a rhombohedral angle $\alpha_{rh} = 89.3°$ at room temperature and ferroelectric polarisation along the pseudo-cubic [111] direction [102, 103]. Since any rhombohedral unit cell representation can be transformed to an equivalent hexagonal one, magnetic and electrical properties of the $BiFeO_3$ crystal can be expressed in the hexagonal cell rather than the rhombohedral one. In this case, the pseudo-cubic direction [111], would correspond to the [001] direction in the hexagonal unit cell. At RT, the hexagonal lattice parameters are $a_{hex} = 3.96$ Å and $c_{hex} = 13.9$ Å[102, 103].

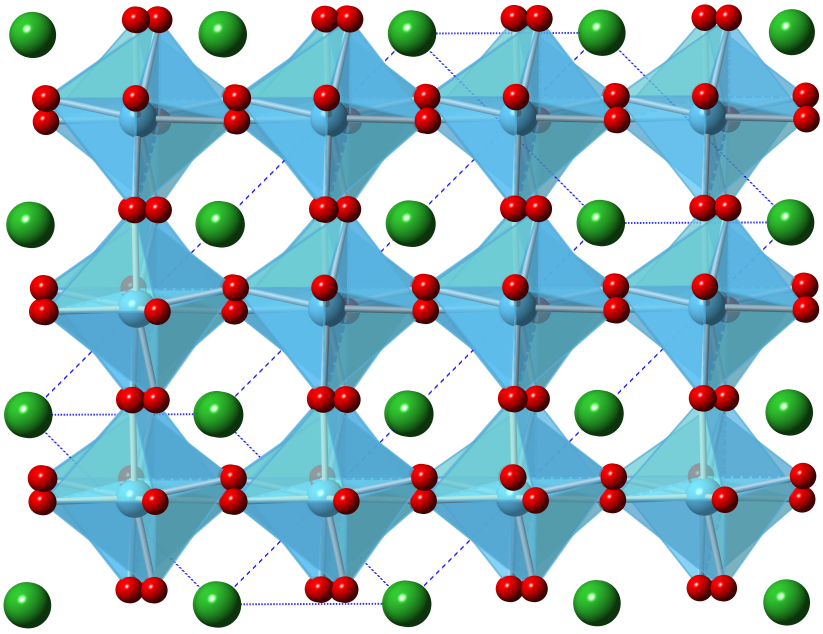

Figure 5.1: Crystal structure of bismuth ferrite. The figure shows the perovskite unit cell with a network of corner linked octahedra. The green spheres represent the bismuth ions at the corners of the perovskite structure, with the Fe ions (blue) sitting in the centre of the oxygen (red) octahedra.

$BiFeO_3$ undergoes structural changes at high temperatures, and the phase it might take due to such changes has been a subject of great debate among many different groups. A detailed phase diagram for $BiFeO_3$ was reported by Palai et al. [104] based on thermal analysis, spectroscopy, diffraction and other methods. According to their work, there is

evidence of three different phases for $BiFeO_3$ above RT and just below the melting point which is about 960 °C: a rhombohedral α-phase below T_C followed by a β-phase in the temperature region 830 - 925 °C, and a final γ-phase between 925 - 933 °C before melting. There have been many different suggestions about the symmetry of the β-phase of $BiFeO_3$. Palai et al. [104] suggested the symmetry of the β-phase to be orthorhombic. However, other authors have suggested that in fact this phase could be tetragonal (space group I4/mcm) [105, 106] although this could not be the case as domain structure dismisses tetragonal symmetry and also, each lattice constant (a, b, c) in the perovskite unit cell is different from one another [104, 107]. Many other symmetries for the β-phase have been reported by different authors including monoclinic ($P2_1/m$) [105, 107], orthorhombic [104, 108] and rhombohedral ($R\bar{3}c$) [109]. A thorough experiment was performed by Arnold et al. [108] by high resolution powder neutron diffraction (PND), and they were able to demonstrate that the phase of the β-phase crystallises in the orthorhombic Pbmn, just as the non-polar compound $GdFeO_3$.

The structure of $BiFeO_3$ discussed so far in only in the bulk, but in thin films the structure of the compound is different from that of the bulk. When grown epitaxially as a thin film using for example a $SrTiO_3$ [001] substrate, the structure changes from rhombohedral to monoclinic. This change in symmetry is the result two different mechanisms: an in-plane contraction and an out of plane elongation because of a lattice mismatch between the substrate and the film. This change in symmetry has been confirmed by various groups [110–112].

5.1.2 Ferroelectricity in BiFeO

$BiFeO_3$ is perhaps one of the multiferroic materials with the highest values of ferroelectric polarization as a result of the ferroelectricity being caused by the lone pair electrons in the $6s$ shell in the bismuth ion, which are highly polarisable [27]. In bulk, the ferroelectric polarisation of bulk bismuth ferrite is along the diagonals of the perovskite unit cell, where the Bi^{3+} ions shift away from the centre of symmetry resulting in an overall ferroelectric

polarisation.

Some of the first measurements of the ferroelectric polarization on single crystals yielded very low values of polarization ($\sim 6\,\mu C\,cm^{-1}$ [113]) which, according to the authors, was due to the limits set by a lack of saturation. The development of new methods to synthesize high quality films, ceramics and single crystals, allowed for better measurements to be made and revealed that the ferroelectric polarisation in the compound was indeed a lot higher than previously reported.

Measurements carried out in epitaxially grown thin films showed an enhancement in the ferroelectric polarisation, yielding a value of $P = 50-60\,\mu C\,cm^{-2}$ (see figure 5.2) at room temperature [5], a value one order of magnitude greater that previously reported in bulk $BiFeO_3$.

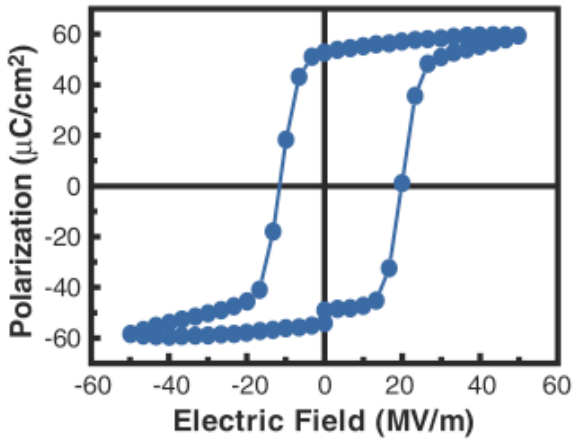

Figure 5.2: Ferroelectric hysteresis loop measured on a $200\,nm$-thick thin film of $BiFeO_3$ (reproduced from reference [5]).

The authors noted that the enhancement (confirmed by first principles calculations [114, 115]) was the result of the high sensitivity of the polarisation to small changes in lattice parameters. Although initially it was thought that the enhancement in polarization in thin films was the result of strain effects, measurements on good quality single crystals yielded polarisation values very close to those obtained from thin film measurements [116, 117] ($60\,\mu C\,\mathrm{cm}^{-2}$ perpendicular to [001] and $100\,\mu C\,\mathrm{cm}^{-2}$ along [111] in the pseudo-cubic unit cell). Large values of polarization were also reported on ceramics [118].

5.1.3 Magnetism in $BiFeO_3$

$BiFeO_3$ is without a doubt one of the most studied multiferroic materials as it is a rare example of a material displaying multiferroic properties at room temperature. In bulk,

the magnetic moments of the Fe^{3+} ions are ferromagnetically coupled within the [111] planes and antiferromagnetically between adjacent planes below the ordering temperature $T_N \sim 643K$, so that every Fe^{3+} ion is surrounded by 6 neighbouring Fe^{3+} ions all with opposite spins (G-type antiferromagnet). The fact that the direction of the moments is normal to the [111] direction, implies that the moments within the antiferromagnetic sublattices are in fact not exactly antiparallel to one another but slightly canted, resulting a macroscopic net magnetisation of the material (weak ferromagnetism). Furthermore, the antiferromagnetic sub-lattices are arranged in such a way, that the overall magnetic structure consists of cycloid-type spin configuration that is incommensurate with the crystal lattice. This cycloid has a repeat distance of about 62 - 64 nm and the propagation vector is along the [110] direction [97, 119–123]. The weak ferromagnetism arising from the canting of the moments within each antiferromagnetic sub-lattice is suppressed by the presence of the spin cycloid which in turn leads to an overall cancellation of macroscopic magnetisation of the material. It has been suggested by some groups that the cycloid may be suppressed by doping [124], or distorted at low temperatures [125, 126], although for the latter there is no data available showing the transition temperatures at which the spin reorientation might occur.

In thin films, it has been suggested that the spin cycloid might also be suppressed as a result of the film's morphology, which allows for the macroscopic weak ferromagnetism to be observed [127, 128]. This view of weak ferromagnetism in thin films as a result of this suppression is supported by first principle calculations, which show that local canting does occur and that the origin of the canting is the Dzyaloshinskii-Moriya interation [129]. According to the calculations, the value of magnetisation is $\sim 0.1\,\mu_B$ per unit cell, a value which is in good agreement with experiment[127, 130]. The magnitude of the magnetisation of the film appears to be related to the film thickness. Values of magnetisation of $\sim 1\,\mu_B$/Fe have been reported from films with a thickness below 100 nm [5].

5.1.4 Magneto-electric coupling in $BiFeO_3$

Despite the fact that the linear magnetoelectric effect (ME) is consistent with the crystal symmetry of $BiFeO_3$, the fact that the magnetic structure consists of a modulated spin cycloid implies that any linear ME effect cannot be observed experimentally [131]. Therefore, only higher order ME effects between polarisation and magnetisation in the material can exist. This is indeed the case for fields below a certain critical field, in which the polarization has been found to be proportional to the square of the magnetic field [131, 132]. Above the critical field however ($\sim$ 20 T), a dramatic change in the polarization is observed, suggesting that above this field the spin structure of the material also changes. It was initially reported that the critical field at which the spin configuration started to change was $\sim$ 5 kOe [133], but since no other group could reproduce the same result [131, 132, 134] it was clear that this was not the case and that the results were probably due to an experimental flaw. As mentioned above, above the critical field a change of sign is observed in the magnetic-induced polarisation and also, the polarisation becomes linearly dependent on the applied magnetic field. This implies that above 20 T the spin cycloid is destroyed, since if it wasn't, a linear relation between the two order parameters could not exist. Another important change above the critical field (the field at which the cycloid is destroyed) is on the magnetic field induced magnetisation, in which an increase value of magnetisation of $\sim$ 0.3 emu/g can be observed [131, 132].

The influence on the magnetic and ferroelectric properties that an applied field has on this system can be understood by looking at what actually causes the spin cycloid in the first place. If $BiFeO_3$ was still centro-symmetric below the Neel temperature, then the magnetic ordering would have an ordinary G-type antiferromagnetic spin configuration. But since the material breaks inversion symmetry and is already ferroelectric below T_N, a canting of the magnetic moments is induced by the ferroelectric polarisation through the DM interaction [129]. The canting of the moments result in a net macroscopic, weak magnetisation of 0.3 emu/g [135, 136]. Apart from the canting, the polarisation also induces the spin cycloid as a result of the coupling of the polarisation to gradients

of magnetisation, which in turn induces an inhomogeneous configuration of the spins, resulting in the spin cycloid [134]. The cycloid itself cancels the magnetisation given by the canting of the moments, resulting in a zero macroscopic magnetisation of the material. But the fact that above the critical field the cycloid is destroyed, allows for a recovery of the remnant magnetisation given by the canted moments and the linear coupling between the two order parameters (magnetisation and polarisation).

Ferroelectric control of magnetic properties on bismuth ferrite has also been explored. The groups that were able to show the behaviour of the magnetism under an applied voltage, were able to do so with very good quality crystals of $BiFeO_3$ with single ferroelectric domains which they managed to grow at temperatures below the ferroelectric transition temperature [137, 138]. They were able to show that the the moments of the Fe^{3+} ions rotate on a plane which is determined by the polarization direction (along the [111] direction) and the cycloid propagation vector (along [10-1]) [138]. A change in the polarisation direction is accompanied by a change in the easy plane of magnetisation. Measurements performed by the two groups [137, 138] showed that a 71° change in the direction of polarisation with an applied voltage corresponded to a change in the easy plane of magnetisation. Furthermore, they showed that a change in polarity (meaning a 180° change in polarisation) did not have and effect on the easy plane of magnetisation, only an overall change in direction would cause the plane to switch.

The control of plane of magnetisation with an applied voltage is indeed very important, as it opens new possibilities of ME devices where applied voltages can induce changes in the magnetisation of the material.

5.2 Experiment and results

5.2.1 Sample preparation

The single phase $BiFeO_3$ sample used for this study was produced by Donna Arnold (University of Kent) using the leaching method, as described in reference [108].The reaction

was made at a temperature of 800° for 5 hours and involved stoichiometric ratios of pure phase Fe_2O_3 and Bi_2O_3 with a 6 mol % excess of Bi_2O_3. The material was then ground into a powder and leached with 2.5 M of nitric acid and stirred continuously for a period of 2 hours. The powder was then thoroughly washed with distilled water and put to dry at a temperature of 400° for 1 hour. Pellets of $BiFeO_3$ were then made pressing the powder at approximately 1.5 tonnes using the pellet die and press (figure 5.3). XRPD measurements confirmed the sample to be phase pure $BiFeO_3$ [108]. It is important to note that according to the authors, after further research they found that the best pellets were the ones prepared at 850° for 3 hours.

Figure 5.3: Bismuth ferrite pellet used for our experiments.

5.2.2 μSR Measurements

As described in chapter 3, the μSR technique is particularly useful in the study of the magnetic properties of materials. Our μSR measurements were made on a $BiFeO_3$ disk of diameter 10 mm and thickness 1 mm (figure 5.3), placed inside a 50 μm foil packet and

suspended between two silver forks with thin mylar tape. Neither the Al foil or mylar tape was of sufficient thickness for the muons to stop in them, and the silver support forks were sufficiently far enough away from the centre of the beam for very few muons to stop in them. Thus, any muons not hitting the $BiFeO_3$ sample continued on to the active-veto detector and were ignored.

Figure 5.4 shows representative spectra of the ZF μSR measurements at several different temperatures, which were fitted for all temperatures with the following model

$$P(t) = A_{BFO}\left(\frac{2}{3}J_0(\omega_0 t + \phi)e^{-\lambda_1 t} + \frac{1}{3}e^{(-\lambda_2 t)^\beta}\right) + A_{bg} \tag{5.1}$$

where A_{BFO} and A_{bg} corresponds to the asymmetry from the muons stopping in the main BFO phase and elsewhere, respectively. For the first term of the BFO fraction, J_0 is a zeroth-order Bessel function with a characteristic precession frequency ω_0, which reflects the intrinsic distribution of internal fields associated with the spin cycloid [139]. An additional Lorentzian relaxation with a relaxation rate of λ_1, is required to describe the data at all temperatures, suggesting an additional form of disorder is present to the disorder intrinsic to the spin cycloid. The second term, with a relative fraction of 1/3, accounts for those components where the muon's spin that lie parallel to the local magnetic field at the muon site in a polycrystalline material (and would therefore not be expected to give rise to a measurable oscillatory signal) [140]. We have found that this term also relaxes, with a relaxation rate of λ_2, which is characteristic of systems with temporal fluctuations [141]. Below $T = 150$ K, we found that a Lorentzian distribution is most appropriate to describe the data, but at higher temperatures, the most appropriate function is a "stretched exponential", with the stretch parameter β varying significantly from 1 (corresponding to the Lorentzian relaxation rate observed at low temperatures).

As can be clearly seen from the data presented in figure 5.4, the fitted model also displayed indicates that the model describes the data extremely well over the full temperature range measured. The χ^2 value at the top of each figure gives an indication about the quality of the fit to the experimental values. It is normalised by the number of degrees of freedom

and it should approach one if the estimation of the errors is correct and the fit to the data is good. The χ^2 value provides and indication of the deviation of the value from unity in the fit. Taking the low temperature data first, the fast oscillation is clear evidence for the presence of sizeable quasi-static electronic magnetic moments, as would be expected in an AFM. Moreover, it indicates that there is a single muon site or set of magnetically equivalent muon sites, as has been shown in $BiMnO_3$ [142] It also shows that all the muons experience a very similar internal field, which is indicative of the high quality of the BFO material used, although, the relaxation rate of the oscillation may be indicative that there might be some inhomogeneities associated to the precessing part of the signal. However, since the relaxation rate (for both components) has exponential form, it is more likely is related to some sort of dynamic process [140, 143]. As shown in figure 5.5, the fast oscillation of ∼90 MHz persists up to ∼200 K, with little deviation from the expected mean-field reduction in the internal field as the temperature is increased (shown by the blue line). For second order phase transitions, the mean-field reduction describes the temperature dependence of the internal field in the proximity of the transition temperature, and has the phenomenological form [144]

$$\nu(T) = \nu(0)\left[1 - \left(\frac{T}{T_C}\right)^{\alpha}\right]^{\beta} \tag{5.2}$$

for $T < T_C$, where T_C is the transition temperature and β is a critical exponent. Fitting the above function to the data, produced $\alpha = 1.99 \pm 2.16$ and $\beta = 0.40 \pm 0.74$. The fact that there is only a small deviation from the mean field, indicates very little magnetic changes between the lowest temperature and 200K. The relaxation rate of the oscillation, λ_1, shown in Figure 5.6 is also temperature independent up to ∼200 K, which also supports this conclusion. As can be seen from figures 5.7 and 5.8, the relaxation rate λ_2 and stretch parameter β of the 1/3 tail, which are related to dynamics of the Fe spin, gradually drift from their low temperature values as the temperature is increased. This indicates that spin fluctuations are slowly increasing as the temperature is raised.

Now moving onto the higher temperatures, it is immediately clear in figure 5.4 that the

100 K spectrum is quite different from the spectra at 210 K and above, with a reduced amplitude oscillation and increased relaxation rate readily observable in the raw data.

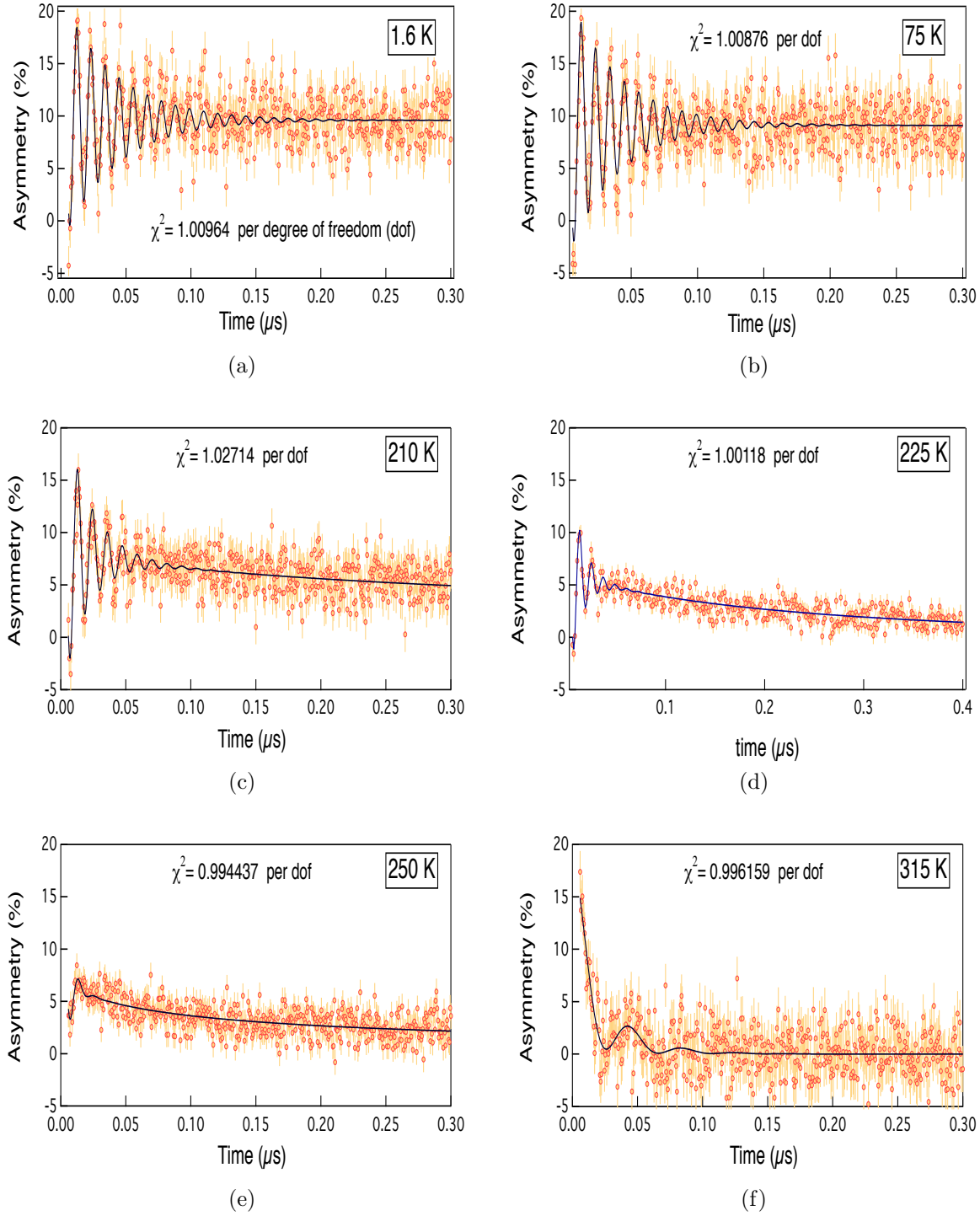

Figure 5.4: Representative muon spectra for a series of temperatures showing the evolution of the muon signal with temperature. The solid red line corresponds to the fit to the data. a) 1.6 K spectrum. b) 75 K spectrum. c) 210 K spectrum. d) 225 K spectrum. e) 250 K spectrum. f) 310 K spectrum.

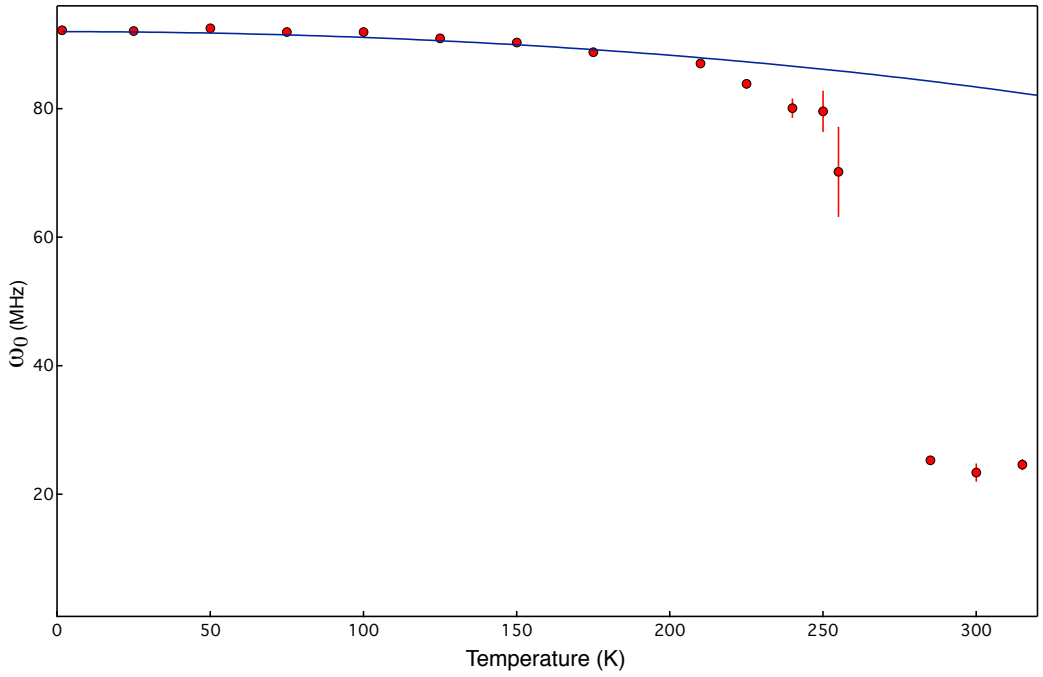

Figure 5.5: Plot of the muon oscillation frequency (ω_0) as a function of temperature. A dramatic decrease in precession frequency can be observed from $\sim$ 90 MHz down to $\sim$ 20 MHz, between 220 K (where the onset occurs) and 260 K, suggesting that the material undergoes a phase transition in this temperature range.

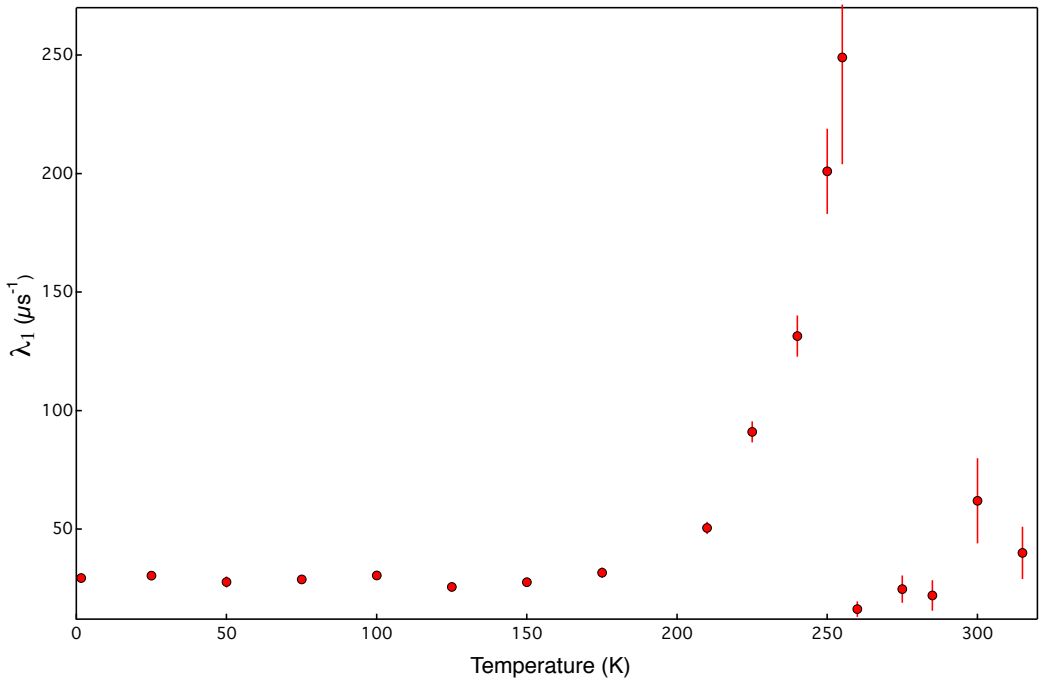

Figure 5.6: Plot of the relaxation rate λ_1 as a function of temperature. The data shows a deviation from the linear trend at $\sim$ 220 K, and a peak in the relaxation at $\sim$ 260 K, consistent with what figure 5.5 shows.

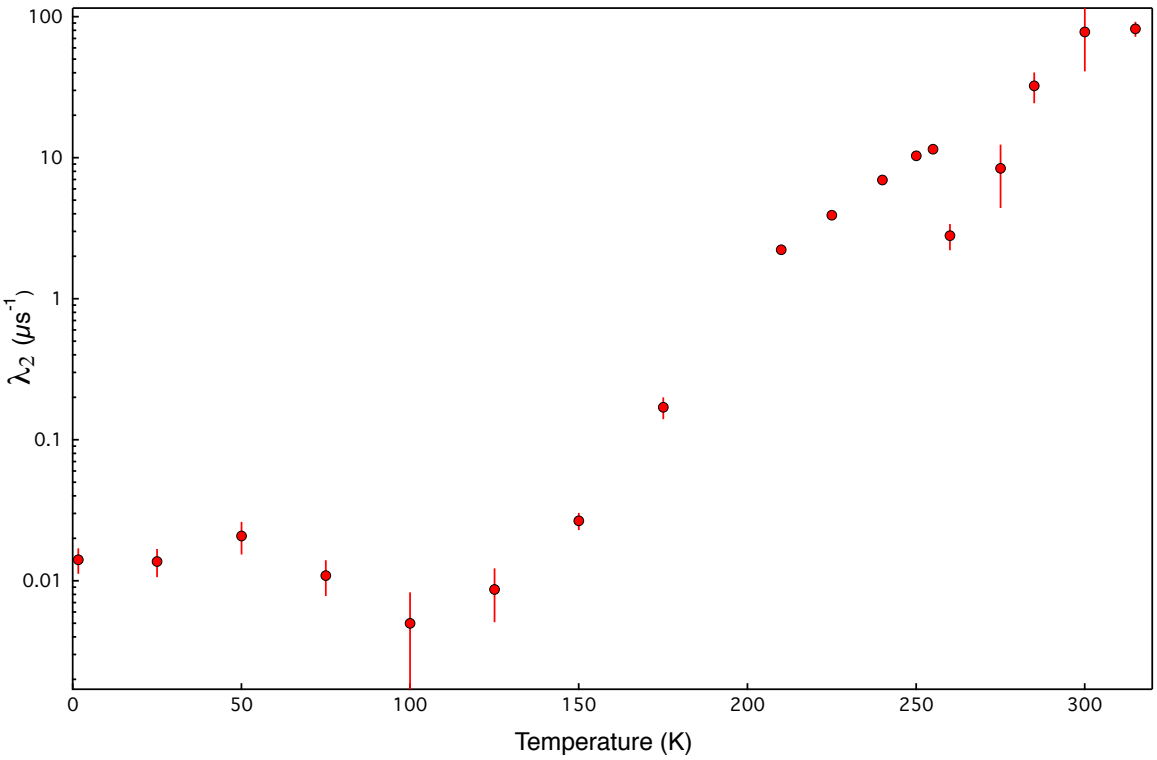

Figure 5.7: Plot of the relaxation rate for the second component, λ_2, as a function of temperature.

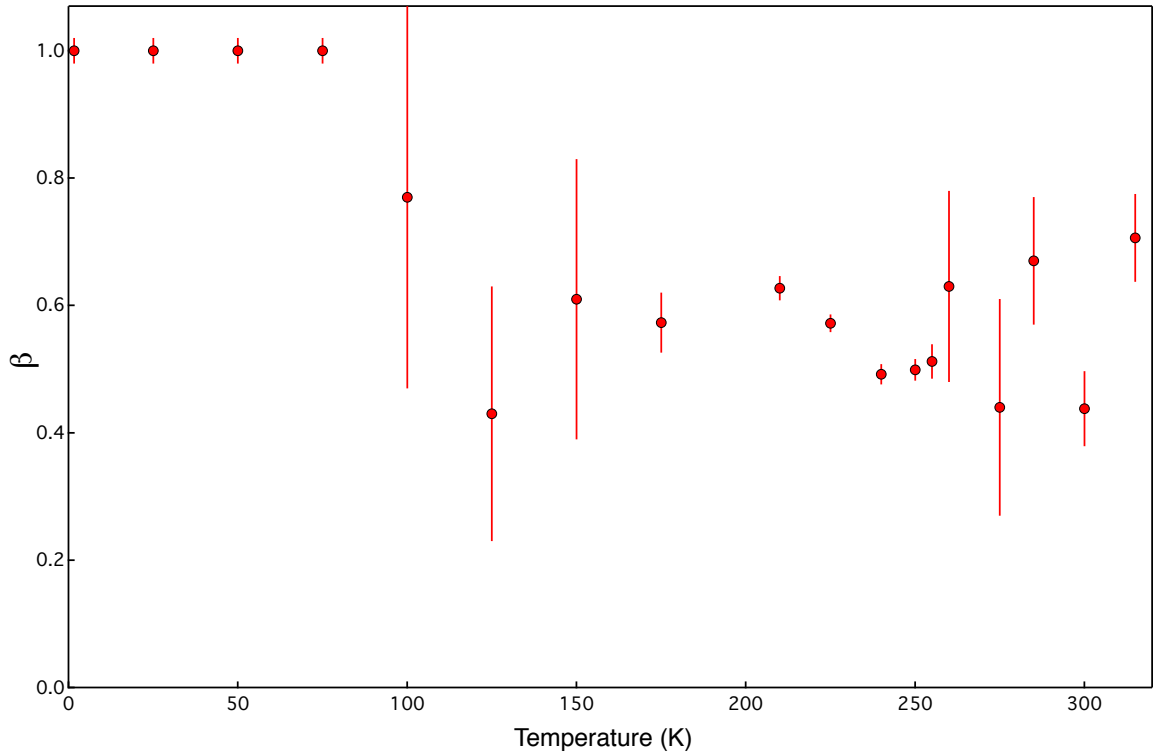

Figure 5.8: Plot of the stretch parameter β as a function of temperature.

It is most clearly seen, however, in the fit parameters displayed in figures 5.5 and 5.6. The frequency begins to drift away from the expected behaviour as predicted by equation 5.2 (solid blue line) above 200 K, with a dramatic reduction to around 25 MHz above 250 K. Moreover, the relaxation rate increases from around 200 K with a peak at 250 K. These rather dramatic changes in the muon spectra correspond to roughly the same temperature that anomalies in the dielectric constant [145], magnetisation [96] and Raman magnon peaks [92] are obverved, suggesting they may be of the same origin. It is worth noting here that these significant and abrupt changes occur in almost entirely the whole sample volume, which can be identified from the muon signal (figure 5.4) and the fact that muons stop uniformly throughout the entire sample. At low temperatures, all the muons experience the same field with an associated relaxation of the signal as a result of the sample being a polycrystal. As the temperature is increased, the oscillating component of the signal starts to decrease until eventually at 250 K the oscillation is almost entirely absent. The fact that the changes happen in the whole volume of the sample, strongly suggests that the anomalies in the magnetisation and Raman spectra (at 230K and 200K, respectively) are bulk phenomena.

Having established the anomalies covering 200 K to 230 K are likely a bulk phenomenon, we now discuss the possible origins of it. A peak in the relaxation rate and a change in frequency is often indicative of a magnetic phase transition [80, 140, 142]. Whilst the the magnon peaks at 140 K have been convincingly shown to be an interface effect [26, 100], which is consistent with our muon results (we see little happening in our data and muons aren't particularly sensitive to surface phenomena), no such firm conclusion can be made for the anomalies in the region of 200 K. As mentioned in the introduction, the origin of the 200 K magnon peak and other phenomena close to this temperature is not clear, but one suggestion is that they could be related to a sub-lattice reorientation below the Neel temperature, analogous to the known transitions in other magnetic orthoferrites (e.g $ErFeO_3$) [93, 94]. However, no such evidence (for example in the form of neutron diffraction) has been presented [98, 99]. Indeed, low temperature neutron diffraction experiments were performed in the WISH instrument at the ISIS Pulsed Muon and Neutron

Source, and little evidence was found for any change to the spin-cycloid [1]. Any large-scale bulk magnetic phase transition, whether from a cycloid reorientation or spin glass, *would* have a very observable effect on the neutron scattering spectra. We therefore believe it is unlikely that the origin of the observed changes in our muon data is either of these.

The large changes observed in our muon data in the region of 200 K could also be of a technique specific origin. The muon itself could be diffusing, as is quite common in magnetic oxides or there could be a thermally driven change in muon site [146, 147], both of which can be driven by, for example, a local structural change in the material. Previous muon experiments on orthoferrites show data that have similarities with the data presented here; there is a dramatic increase in relaxation rate and change in precession frequency as the temperature is increased [146, 147]. In five orthoferrites ($MFeO_3$, where M = Eu, Dy, Y, Ho or Er), the muons are shown to be localized in long-lived metastable muon-oxygen bonding states below 360 K, but above this temperature, local diffusion between two or more sites sets in, and only at much higher temperatures (in excess of 500 K) does global long-range diffusion occur. For the case of $SmFeO_3$, the local diffusion sets in above about 300 K [146, 147]. The similarities between the data presented in this thesis and that of the other orthoferrites is compelling enough for us to believe that muon diffusion is the origin of the dramatic changes in our data.

However, there are some items of note that warrant this investigation of the local structure of $BiFeO_3$ to be concluded. The temperature at which the muons begin to diffuse is significantly lower than in other orthoferrites with similar crystal structures. Granted, one may expect differences; $BiFeO_3$ is a ferroelectric and the Coulomb interaction plays an important role in determining the eventual stopping position of the muon. Moreover, the crystal structure of $BiFeO_3$, whilst similar to the orthoferrites, is not exactly the same. However, the muon diffusion temperature also happens to correspond to the anomalies observed in several other techniques, which have no muon involved. This raises the following question: is there some underlying change in the bulk of the material that is driving the muon diffusion at 200 K, or is it merely an intrinsic property of the particular

[1] This experiment was performed by one of our collaborators and is outside the scope of this thesis

muon site in $BiFeO_3$?

5.2.3 Total scattering measurement of the pair distribution function

In order to answer the question above, total neutron scattering measurements were performed on our sample. In the μSR technique, muons are used as local probes to find information about the magnetic properties of materials. Neutron scattering on the other hand, uses neutrons as a probes to investigate the average structure (either crystal or magnetic) of a given material. In order to corroborate our muon experiment results, we need a probe that can also measure local structure and although neutrons are not conventionally used this way, they can also be used as local probes by analysing the atomic pair distribution function (PDF) of a total scattering experiment. The PDF technique has been in use for many years to study systems with a lack of long-range order such as liquids and glasses [148]. But as a result of high power X-rays and neutron sources that can provide shorter wavelength particles (high energy X-rays and epithermal neutrons) and thus increase the range of the scattering vector magnitude Q_{max}, as well as major improvements in computing methods such as Rietveldt refinement and Monte Carlo modelling analysis, becoming more readily available, the technique has been further extended to be used in crystalline materials. Conventionally, information about the underlying structure of materials can be obtained by means of crystallographic methods in which the analysis of Bragg reflections is sufficient to determine what the structure of the material is. But when disorder in a material is the part of interest, the diffuse scattering component of the total scattering can no longer be ignored as it contains all the information related to local deviations or imperfections at the nanocrystalline level.

Following, I shall give a brief description about the technique and the experimental details for our $BiFeO_3$ sample. For more detailed information about the PDF technique, see references [148–151].

Background

In a total scattering experiment, the overall scattering intensity includes information about the global structure of the material (Bragg peaks), the static local structure (elastic diffuse scattering) and also, information about atom dynamics. The diffuse scattering component of the overall pattern is the object of interest in our case since, just as with μSR giving information on the local magnetic environment, it provides information about localised structural changes in a material that are otherwise hidden from conventional X-ray or neutron scattering. The PDF, which is often written as the reduced PDF, G(r) (see [148, p. 59]) is defined as

$$G(r) = 4\pi r[\rho(r) - \rho_0] \tag{5.3}$$

where $\rho(r)$ is the atomic pair density, ρ_0 is average atomic number density and r is a radial distance (see reference [148, p. 8] for a detailed mathematical definition of $\rho(r)$).

The PDF of a diffraction pattern is a histogram displaying interatomic separations and it describes the weighted probability of finding pairs of atoms separated by a given distance r. The PDF can be found experimentally by taking the sine Fourier transform of the total scattering structure function S(Q) in reciprocal space, which yields

$$G(r) = \frac{2}{\pi}\int_0^\infty Q[S(Q) - 1]\, sin\, Qr\, dQ \tag{5.4}$$

where S(Q) is the normalised, diffracted intensity from the sample and Q is the scattering vector with magnitude $Q = 4\pi\, sin\, \frac{\theta}{\lambda}$ [151]. In this sense, the technique takes advantage of the link between measurable diffraction intensities and the real space arrangement of atoms through Fourier transforms, which makes it possible for the PDF to be defined directly in real space in terms of atomic coordinates [151].

The fact that the PDF and the diffraction pattern are linked by a Fourier transform, implies that the two functions must contain the same information [148, 152]. The global structure within the diffraction pattern is attributed to the Bragg component, while

the diffuse scattering dominates at higher scattering angles and contains information regarding local deviations from the average structure. PDF methods make use of the diffuse scattering contribution to the diffraction pattern in order to investigate any local deviation from the average structure in real space.

One of the most straightforward and indeed, useful features of the PDF method, is the fact that a proper analysis of the data can be used to determine changes in bond lengths directly from the PDF [152]. Just like in conventional diffraction pattern, a PDF pattern displays a set of peaks, but unlike conventional structural analysis in which the obtained bond lengths from each peak correspond to the average position between pairs of atoms, in a PDF pattern each peak correspond to a certain bond length distribution for a given pair of atoms, ie. they represent the average distance between the positions of a given pair of atoms in the unit cell.

A proper fit to the data in the PDF can give two important pieces of information in terms of local structure. First, the coordination number (number of nearest neighbours) can be determined by looking at the area under the peak. Second, the width of each peak can tell us the degree of static of dynamic changes in bond lengths, which is in turn directly related to the vibrational energies of the material under study [153]. A peak with a small width is a strong indicative of conserved bond lengths, which implies high vibrational frequencies. Large width peaks on the other hand, are indicative of bond lengths that are weakly conserved and low vibrational frequencies in the system.

Experiment

This work was done in collaboration with Dr. Anthony Phillips and Miss Juan Du who performed the neutron measurements on the $BiFeO_3$ sample. Total scattering measurements were performed on the General Materials (GEM) powder neutron diffractometer [154] at the ISIS Pulsed Muon and Neutron Source with the assistance of the beam line scientist David Keen. The neutron source at ISIS is a spallation source in which pulsed beams of protons are fired into a heavy-metal target (usually tantalum or uranium). The

collision of the beam of protons with the atomic nuclei of the target causes neutrons to be knocked off with very high kinetic energy. In order for the neutrons to be useful for experiments their kinetic energy has to be reduced, so to accomplish this, moderators are placed between the target and the sample area. The Gem diffractometer uses a liquid methane moderator at a temperature between 100 and 110 K to thermalise the incoming neutron beam [154]. The Gem instrument is a time of flight instrument where the intensity of the neutron beam is recorded as a function of flight time (see reference [30, p. 126] for details on the TOF neutron technique). The flight path distance of the instrument is 17 m from moderator to sample.

GEM can be used to perform high intensity, high resolution experiments to study the structure of both disordered materials and crystalline powders, with the most important component being the detector array which has a very large area of 7.270 m^2. It comprises eight detector banks with a wide scattering angle range from 1.1^o to 171.3^o [154, 155]. This very wide range in scattering angle, 2θ, leads to a very wide range in Q values, giving a great advantage in the investigation of disordered materials.

Results

Shown in Figure 5.9 is the pair distribution function of real-space interatomic distances, $D(r)$, for $BiFeO_3$ as a function of temperature. It is immediately noticeable that all but one peak shifts slightly to higher r and broaden as the temperature is increased. This is just the result of a small increase in bond length and the thermal motion of atoms increasing as the sample is heated, which is to be expected. However, the peak at ∼2.5 Å corresponding to the Bi-O bond broadens significantly more than the other peaks as the sample temperature is increased, entirely disappearing at 236 K. This is strongly indicative of an as-yet unreported change in the local structure of the material at low temperatures involving the Bi- O Bond length, which is in turn driving the muon diffusion that is observed in our muon data above 200 K.

To confirm this experimental results, reverse Monte Carlo analysis (RMC) was performed

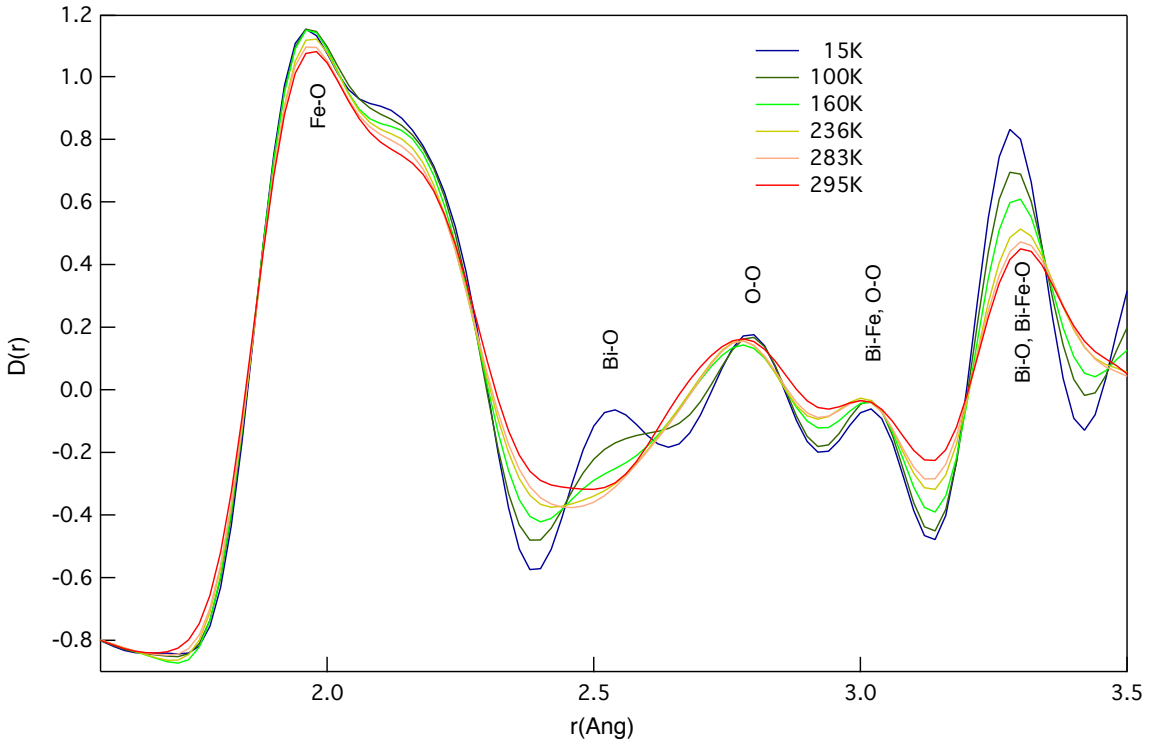

Figure 5.9: Plot of of the pair distribution function, D(r), Vs r for a number of different temperatures. The second set of peaks from left to right, which corresponds to the Bismuth-Oxygen bond, is the part of interest in the plot. The peak disappears above $\sim 160K$ suggesting a new structural change in the material above this temperature.

on the experimental data focussing on the peak at 2.5 Å (figure 5.9) which as mentioned earlier, corresponds to the Bismuth-Oxygen bonds. The analysis was done in order to have a better understanding about the dynamics of the system in terms of the change in distance between Bi-O pairs above 200 K. I would like to stress that the RMC analysis was all carried out by Dr Anthony Phillips and Miss Juan Du from Queen Mary University London, and all the figures presented in this thesis involving the PDF and RMC analysis were reproduced with their permission in order to be able to explain the results from our μSR experiment.

Figure 5.10 shows a plot of $D(r)$ versus r for different temperatures, as obtained from the RMC analysis. The first two peaks at ~ 2.5 Å corresponds to the nearest and next nearest neighbours relative to the bismuth ion, and are labelled 1 and 2 respectively. Figure 5.11 shows a schematic representation of the positions of the neighbouring oxygens and their associated distance to the bismuth ion (green corresponds to the nearest neighbours and

blue to the next nearest neighbours, also labelled in the sketch as 1and 2 respectively).

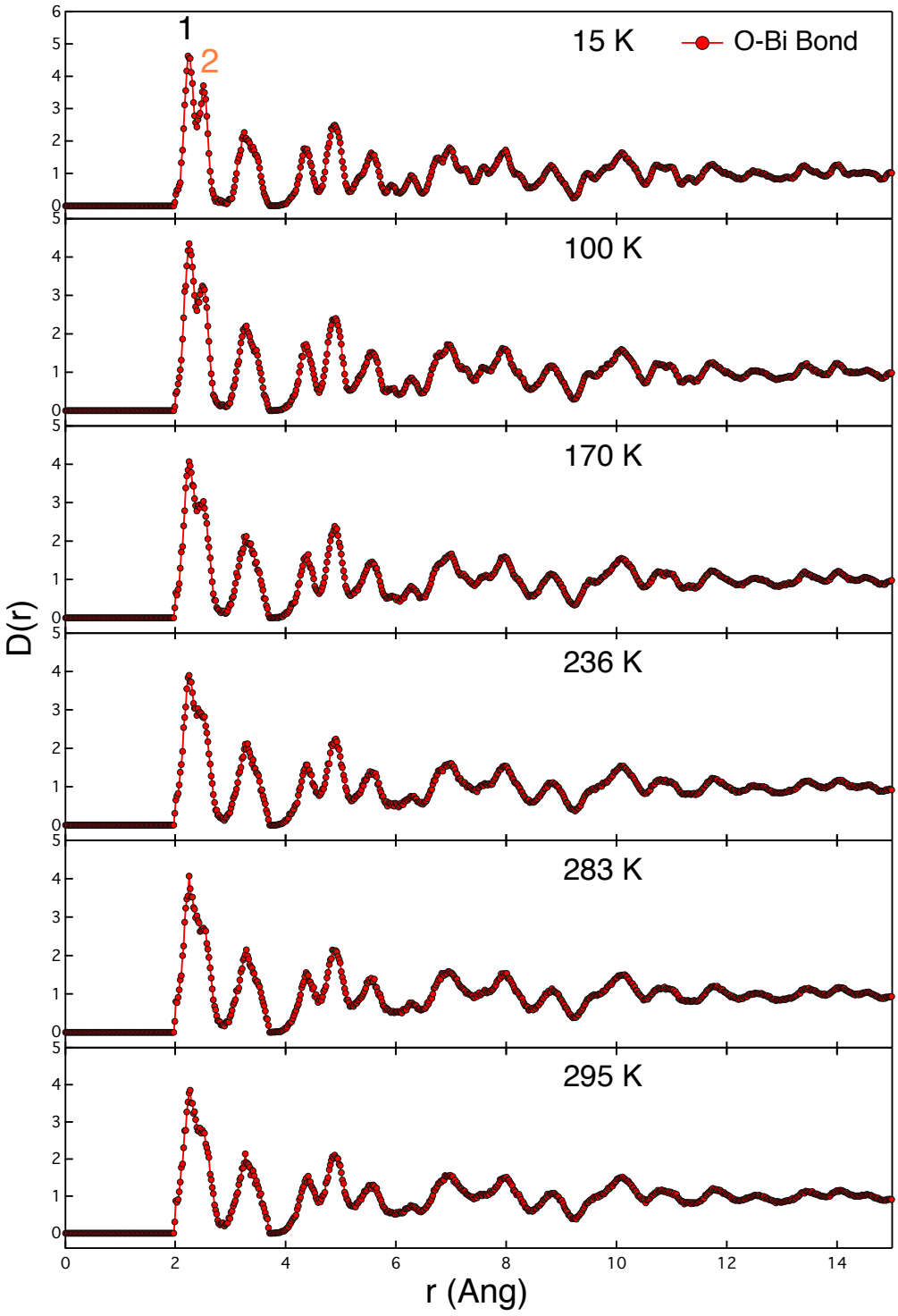

Figure 5.10: Plot D(r) as a function of r for a number of temperatures. The nearest (1) and next nearest (2) neighbours relative to the bismuth are indicated on the top graph.

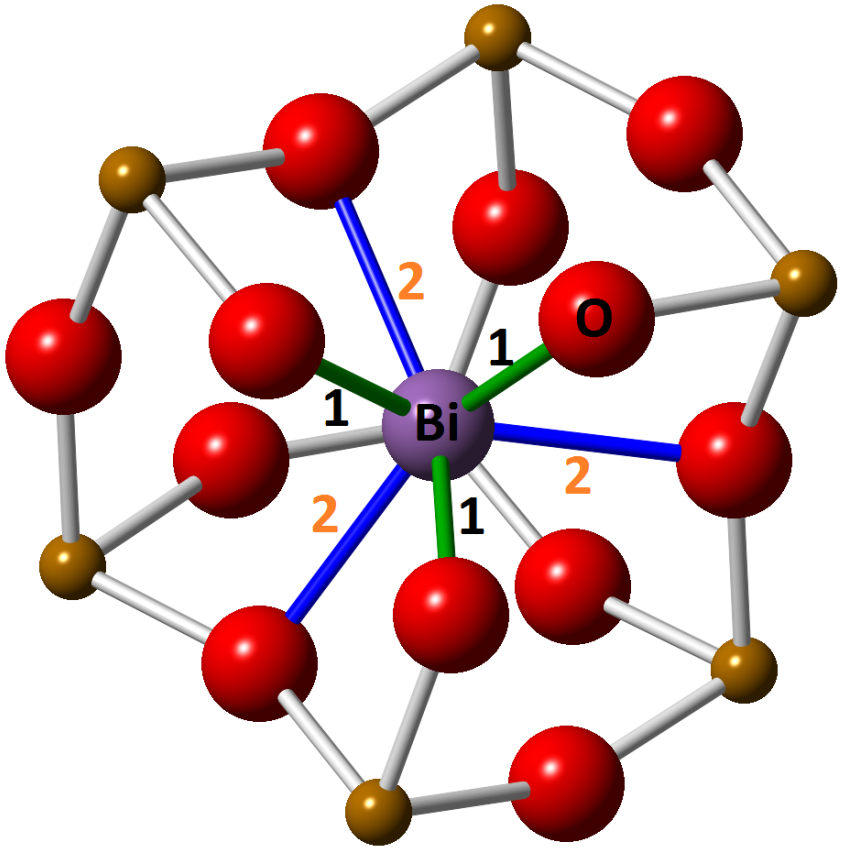

Figure 5.11: Schematic representation of the nearest and next nearest oxygen neighbours with respect to the bismuth ion. The nearest neighbours as labelled as 1 (green bonds) while the next nearest neighbours are labelled as 2 (blue bonds). The numbers correspond to the peaks (also labelled 1 and 2) on figure 5.10 at $\sim$ 2.5 Å.

It is clear from the data shown in figure 5.10, that while the peak corresponding to the nearest neighbours remains the same with increasing temperature, the peak corresponding to the next nearest neighbours increases in width with increasing temperature. At low temperatures, the second peak has a narrow width, meaning that the bond length between the oxygen and bismuth ions is conserved. however, as the temperature is increased, the peak starts to get broader until eventually at some temperature above 200 K the peak is so broad that it seems to disappear, which indicates that the bond length corresponding to the bismuth and the next nearest neighbours is no longer conserved and also, that there are large local deviations that are driving the muon diffusion in the material. Furthermore, the temperatures at which the peak gets broader is consistent with the temperatures at which the muon diffusion sets in.

This is indeed consistent to what is observed the muon data. The fact that the muons

used in experiments are positively charged, implies that the muon site will most likely be in areas of large electron density which in this case would be close to the negative oxygen ions (usually about 1 Å away from the oxygen ion). At low temperatures, there is only one muon site (or a number of magnetically equivalent muon sites) in the material. As the temperature is increased, thermal fluctuations trigger a change in the local configuration of the oxygen ions with respect to the bismuth ion, with the larger deviations being on the next nearest neighbours, as shown on the PDF data. At ∼200 K, the thermal fluctuations are such that the oxygen next nearest neighbours start to move around in a way that also changes continuously the potential minima and therefore the muon site, and as a result the muon diffusion sets in.

5.3 Conclusion

To conclude, we have performed μSR and total neutron scattering measurements on a $BiFeO_3$ sample in order to investigate some of the low temperature anomalies reported in the literature that are still unaccounted for. Our analysis on the muon data obtained from our BFO sample, has shown anomalies in the temperature region $T \sim 200$ K, which is consistent with the temperatures at which other anomalies have been reported using different experimental techniques, although, just as the other techniques, the muon data alone can not explain the source of the anomaly. From a combined analysis of muon, and neutron data, as well as RMC analysis of the PDF, we have been able to show that this anomaly is actually linked to a yet undiscovered low temperature change in the local structure of the material involving the Bi-O bond, which is driving the muon diffusion observed in our data above 200 K. Total neutron scattering measurements performed on the sample as well as RMC analysis corroborates our muon results. Preliminary analysis of the pair distribution function shows that the bond length between the Bi-O ions increases with increasing temperature and above 200 K the peak disappears altogether, signalling the onset of the local deviations of the oxygen next nearest neighbours with respect to the bismuth ion. Also, the muon's sensitivity to volume fractions indicates that the anomaly

is in fact a bulk phenomena occurring in almost the entire sample. The similarities in temperatures between the local structural change reported in this thesis and the anomalies in the dielectric constant, Raman spectra, magnetisation and AC-susceptibility, which are all in the region of 200 K, suggests they are related. We see no evidence of any further changes at lower temperature, suggesting that the anomalies at 30 K, 50 K, 90 K and 140 K are either impurity based or restricted to surface effects. Despite the large number of studies on this material, this local change in the structure, as identified by out muon and neutron data has never been observed. These results are due to be published within two months.

Chapter 6

Experimental results: Magnetoelectric behaviour on the Tetragonal Tungsten Bronze $Ba_4Dy_{0.87}Nb_{10}O_{30}$

6.1 Overview

As mentioned in the introduction of this thesis, research on multiferroic materials has increased dramatically in the past decade as a result of the potential applications in novel multifunctional devices, such as actuators, transducers, sensors and memories [13, 16]. One of the main objectives of the research in this field is to find materials with a strong coupling between ferroelectricity and magnetism. Materials research focuses on two major thrusts; single-phase and composite multiferroics, the latter involving the design of novel multiferroics by combining magnetostrictive and electrostrictive materials (ie. ferromagnets and piezoelectric materials). The fact that ferroelectricity and magnetism tend to be chemically contraindicated implies a very difficult challenge in terms of the synthesis of single phase multiferroics. The study of single phase MF has primarily centred on mate-

rials with perovskite structure such as $BiFeO_3$ and $BiMnO_3$ due to their relatively ease of synthesis and also their well known and relative simplicity of their structure [5, 156–158].

Magnetoelectric effects in single phase materials can be the result of a number of different effects, from domain wall clamping such as the case of $GdFeO_3$ [159], or magnetoelectric effects in helical magnets where the electric polarisation couples to the magnetism via the spin-orbit interaction [160]. Composite materials, which are either thin film heterostructures of magnetic-ferroelectric oxides or bulk ceramic composites with micron-sized grains, are often coupled via strain effects [161]. ME coupling so far observed in the ceramic composites is at least ten times lower than predicted, due to atomic inter-facial diffusion and reaction problems, thermal expansion mismatch between two ceramic phases, a small surface area (between grains) compared to volume of each grain and leakage due to semi-conductive magnetic oxides [161]. The tetragonal tungsten bronze (TTB) structure with chemical formula $A1_2A2_4C_4B1_2B2_8O_{30}$, is closely related to perovskite structure and therefore, the structure also offers similar compositional flexibility [162, 163]. The TTB structure (shown in Figure 6.1) offers extra degrees of freedom for compositional tuning of properties by accommodating non-stoichiometry with vacant C-sites and more than 20% A-site vacancies. Additionally, it has crystallographically distinct sites on both A- and B- cation sublattices, which is of particular interest as it offers the opportunity to selectively order magnetically and ferroelectrically active ions on A- and/or B-sublattices by co-operative doping. This essentially allows an atomic composite approach to develop novel multiferroic materials, which has the potential to overcome many of the limitations with traditional composites, possibly exhibiting strong magnetoelectric coupling.

6.1.1 Synthesis and structural characterisation

The following study on this TTB compound was made in collaboration with several individuals from universities across the United Kingdom as well as beam line scientists at the ISIS laboratory. The material used for this study was synthesised at the University of St. Andrews by Dr Donna Arnold. I want to acknowledge that some of the neutron

data presented in this chapter was collected and analysed by our collaborators, and I have noted where this is the case.

In this study, a Dy substituted TTB material was synthesised based on the nominal composition $Ba_3Dy_2GaNb_9O_{30}$ using methods previously described on references [162, 164]. Stoichiometric ratios of $BaCO_3$, Nb_2O_5, Ga_2O_3 and Dy_2O_3, (all Aldrich, 99+%) were ball milled in ethanol for 5 mins at 400 rpm. After drying, the powders were exposed to a temperature of 1000 °C for a period of 4 hours followed by an extra 6 hour period at 1250 °C. The heating rate was about 20 °C/min. The powders were then quenched to room temperature, reground and re-heated at 1300 °C for another 6 hours.

X-ray measurements were performed on the resulting powder using Cu Kα_1 radiation (40 kV and 30 mA with wavelength $\lambda = 1.54413$ Å) over a range $20 < 2\theta < 60$, and phase formation was confirmed with the measurements. Neutron diffraction measurements on the powder samples were performed at the ILL (France) on the D2B beamline with neutrons of a constant wavelength $\lambda = 1.5943201$ Å. The data was collected at room temperature with the compound placed into vanadium can.

The neutron data was analysed by Dr Finlay Morrison and Dr Donna Arnold from the University of St Andrews and the University of Kent, respectively. The data collected was refined in the polar tetragonal space group P4bm and lattice parameters were found to be $a_T = b_T = 12.4617$ Å and $c_T = 3.9511$ Å. The analysis of the collected neutron and X-ray data, also showed material was not in fact single phase but that there were two secondary phases, namely Ga_2O_3 and $DyNbO_4$. Based on multiphase refinements, the quantities of each of the three phases were found to be 74 wt% TTB (main) phase, 23% $DyNbO_4$ phase and 3% Ga_2O_3 phase. Attempts were made to include Dy^{3+} ions onto the B-site as a result of the ion's relatively small ionic radii (0.91 Å) [65]. This however, proved not to be possible; analysis of the data resulted in nonsense values for fractional occupancies strongly suggesting that the Dy^{3+} is in fact distributed exclusively on the A-site. The analysis also indicated tha the Ba^{2+} only occupies the pentagonal A2-site.

Despite the fact that our material is a multi-phase material, neither of the impurity

phases, Ga_2O_3 and $DyNbO_4$, exhibit unusual electrical or magnetic behaviour. Ga_2O_3 is a diamagnetic ($3d^{10}$) wide band-gap semiconductor with a low dielectric permittivity ($\epsilon_r \sim$ 10 [165]) and as noted above, is only present at trace amounts of the sample. Electrical and AC susceptibility measurements of $DyNbO_4$ show that it is an electrical insulator with a temperature-independent permittivity, $\epsilon \sim 20$, and has an antiferromagnetic order temperature no greater than 1.6 K, above which it is paramagnetic [166]. We therefore conclude that the magnetic and ferroelectric behaviour that will be described later in the text, describes that of the main TTB phase.

The structure of TTB under study is shown in figure 6.1. The figure shows a schematic representation of the crystal structure of the compound, where the green squares represent the NbO_6 octahedra, the blue spheres represent the Dy^{3+} ions and the brown spheres represent the Ba^{2+} ions.

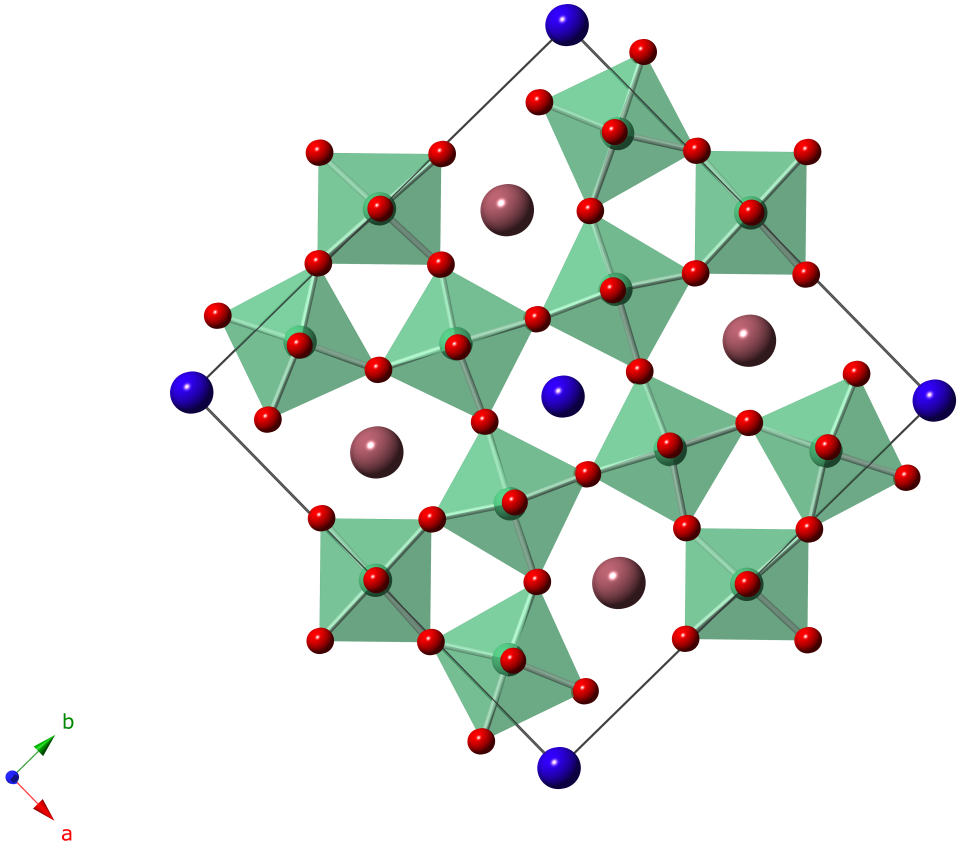

Figure 6.1: Crystal structure of the TTB $Ba_4Dy_{0.87}Nb_{10}O_{30}$. The green squares represent the NbO_6 octahedra cage on the B-site, the blue spheres represent the Dy^{3+} on the perovskite A1 site and the brown spheres represent the Ba^{2+} on the pentagonal A2-site.

Further analysis of the neutron data also revealed a large displacement of the Nb^{5+} ions on both the B1 and B2 sites, along the c-axis. A close inspection of the Nb-O bond lengths from the data, shows a heavy level of anisotropy suggesting that the Nb^{5+} is indeed moving away from the centre of symmetry of the oxygen cage, which is consistent with ferroelectricity.

6.1.2 Structural origin of ferroelectricity

In order to determine the ionic displacements that lead to the ferroelectricity in this compound, the data was analysed and refined in the polar (P4 bm) and non-polar (P4/mbm) tetragonal models. The analysis shows that there is indeed a spontaneous ferroelectric displacement along the c-direction and also, very little atomic motion in the a/b plane. A calculation of the magnitude of the polarisation from the atomics displacements was carried out, using the methodology used in reference [167] as

$$P = \sum_i (m_i \times \Delta x_i \times Q_i)/V \tag{6.1}$$

where m_i is the site multiplicity, Δx_i is the atomic displacement along the c axis from the central position in the non-polar tetragonal structure, Q_i is the ionic charge in the ith ion and V is the volume of the unit cell. An overall polarisation of $P = 1.82\,\mu C/cm^2$ was observed for $Ba_4Dy_{0.87}Nb_{10}O_{30}$ which is in good agreement with P(E) measurements performed in the sample and which will be shown later in the text.

6.2 Ferroelectric characterisation

In order to investigate the ferroelectric properties of the material, dielectric measurements were carried out by Dr Finley Morrison at the university of St. Andrews using HP4192A and Agilent 4294A impedance analysers over a frequency range of 5 Hz-10 MHz and a temperature range of approximately 50 - 1000 K. Polarization-field (P(E)) loop measurements were also carried out using an aixACCT:TF2000 analyser over a temperature range

293-423 K.

Figure 6.2 shows a plot of relative permitivity as a function of temperature for different frequencies and the associated dielectric loss (tan δ) for $Ba_4Dy_{0.87}Nb_{10}O_{30}$. The plot shows a peak in the relative permitivity at $T \sim 470\,K$ as well as the associated minimum in dielectric loss around the same temperature. Such behaviour is characteristic of a paraelectric to ferroelectric phase transition, strongly suggesting that the material is indeed ferroelectric. A closer inspection of the data (especially in the dielectric loss) also reveals some other subtle changes at 50, 165 and 300 K as shown in figure **??**, where the plots show zoomed in regions of the data at these temperatures to see the changes more clearly. The changes at 50 and 165 K are associated with changes in the magnetic behaviour in the material, which will be discussed later in the text. The anomaly at 300 K corresponds to a change in the frequency dispersion in the permitivity and might suggest a commensurate-incommensurate transition on cooling as have been observed in other ferroelectric TTB oxides [168].

Measurements of polarization as a function of electric field (P(E) loops), confirm the ferroelectric behaviour of the material. The Polarization-field measurements were taken under different conditions. Figure 6.3 is a plot of polarisation as a function of increasing field at room temperature ($T = 300K$) showing the development of polarisation. In figure 6.4 , the polarisation is measured as a function of temperature, and it shows the slimming of the polarisation loop as the transition temperature ($T \sim 470K$) is approached. Finally, figure 6.5 shows a plot of Polarization Vs electric field at a number of frequencies at room temperature.

From these graphs, the value of the remnant polarisation $P_r = 1.94\ \mu$C/cm which is indeed consisted with the value of 1.82 μ C/cm, calculated from the refined crystal structure at the same temperature. The polarisation-field data displays the expected behaviour in terms of the field, temperature and frequency dependence, which is consistent with a displacive ferroelectric with a ferroelectric Curie temperature $T_C = 470$ K.

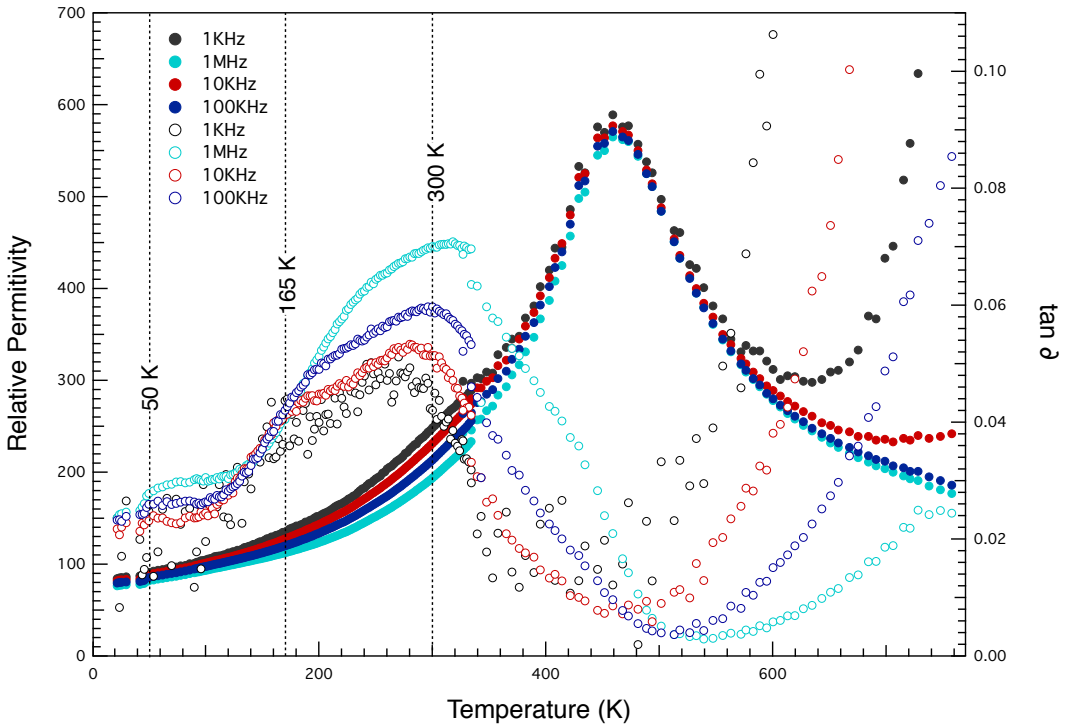

Figure 6.2: Relative permitivity and associated dielectric loss as a function of temperature. The peak in the permitivity and drop on tan δ signal the onset of ferroelectricity below the transition temperature T$\sim 470K$.

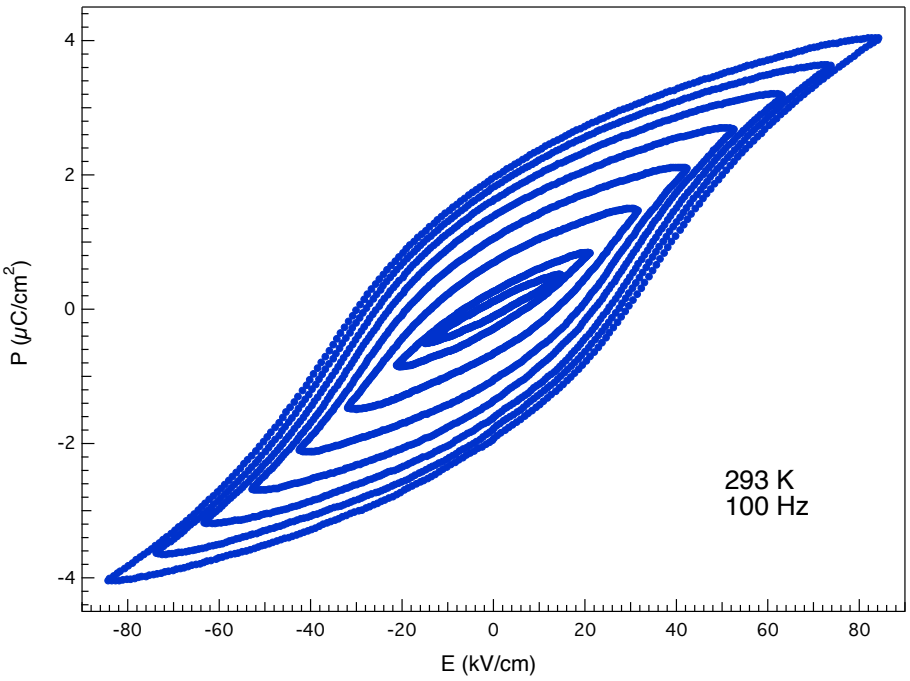

Figure 6.3: Polarisation as a function of applied electric field. The loop is taken at 300 K and a constant frequency of 100 Hz. The graph shows the development of polarisation with increasing E-field.

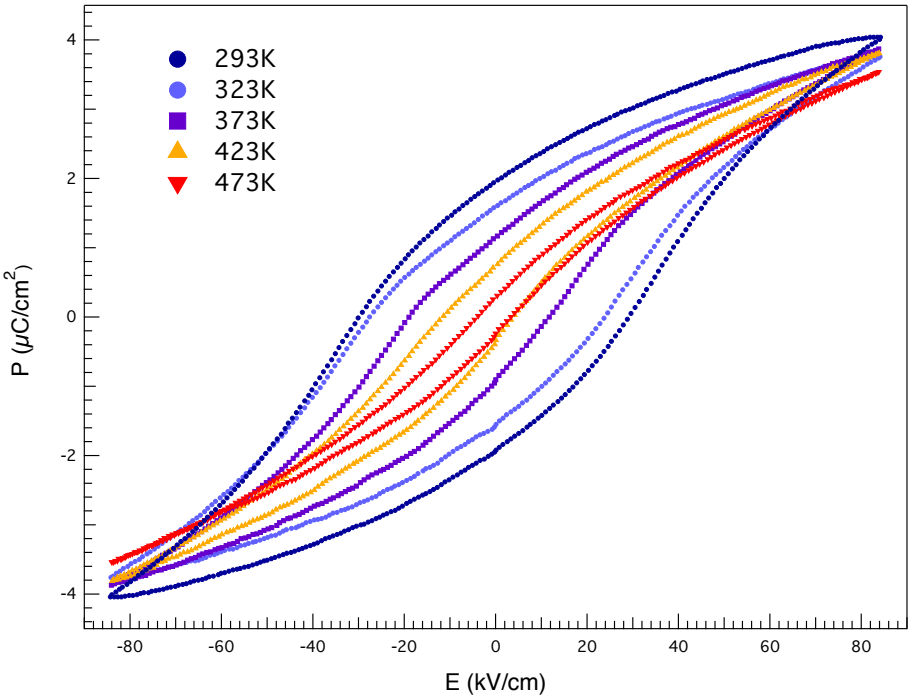

Figure 6.4: Polarisation-Field loop as a function of temperature. The slimming of the loop can be seen as T_C is approached.

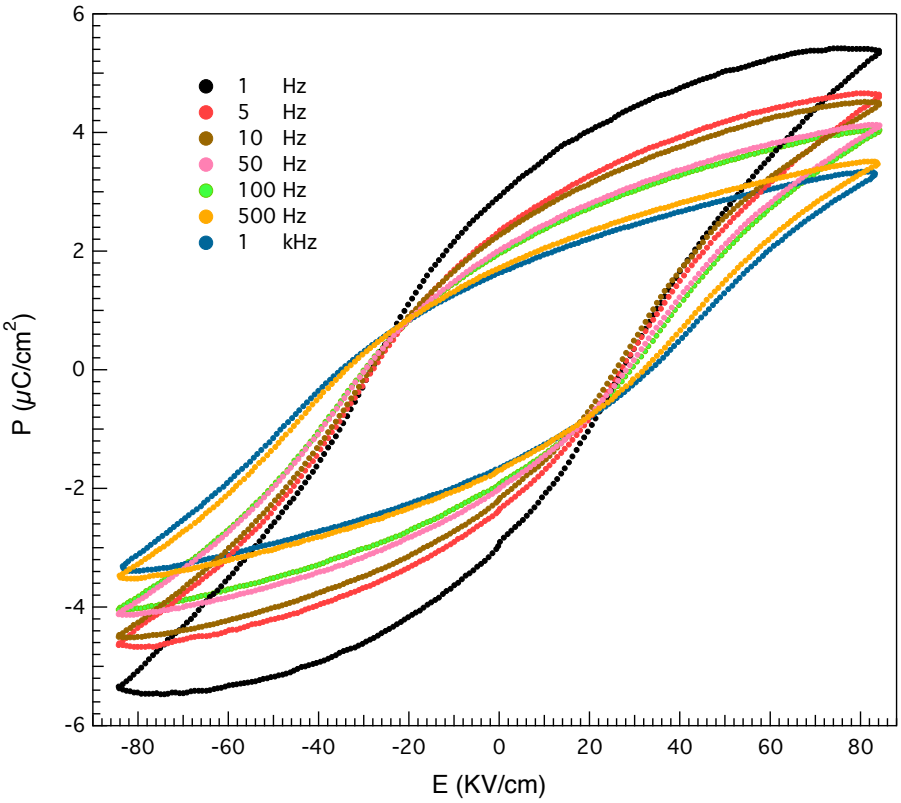

Figure 6.5: Polarisation-Field loop for a different number of frequencies at 300 K. The graph shows that the change in frequency does not affect the shape of the loop.

6.3 Magnetic susceptibility measurements

The magnetisation measurements for this compound were carried out at ISIS on a Physical Properties Measurement System (PPMS) using the Quantum Design Vibrating Sample Magnetometer option (VSM). This instrument is able to provide sample environments in a temperature range of 1.9 K- 400 K and magnetic fields of up to 16 T. In order to carry out the measurements, the sample is placed in a small capsule which is held in place using a piece of cotton (to prevent the sample from moving as a result of the oscillations) and it is then attached to the end of a sample rod. The rod is then inserted into the cryostat with the position of the sample being within a set of detection (pick up) coils. The actual measurement is performed by mechanically oscillating the sample of interest inside an inductive pick up coil and measuring the induced voltage. The instrument uses a compact gradiometer pick up coil configuration which allows for a large oscillation amplitudes (1-3 mm) and a frequency of oscillation of about 40 Hz [169].

The magnetic susceptibility measurements on our sample were performed using the direct current (DC) option, where the sample is made to oscillate at a frequency of a few Hz. The sample was zero field cooled (ZFC) and data was collected while warming. As a result of a problem with the cryostat, the the sample could not be cooled down to base temperature $\sim$ 4 K and the lowest possible temperature we could reach for this measurements was $\sim$ 20 K.

Figure 6.6 shows a logarithmic plot of magnetic susceptibility as a function of temperature. In the plot, the collected data is shown by the red markers while the solid black line represents the Curie-Weiss law [13, p. 52] fitted to the data obtained. From the plot, It is quite clear that a good fit is only obtained at high temperatures; at low temperatures there is a clear deviation from the paramagnetic Curie-Weiss law.

The deviation from the Curie-Weiss law is better observed by plotting the difference between the fit and the data, as shown in figure 6.7. This plot reveals a magnetic anomaly at =165 K and a further change in gradient at low temperatures.

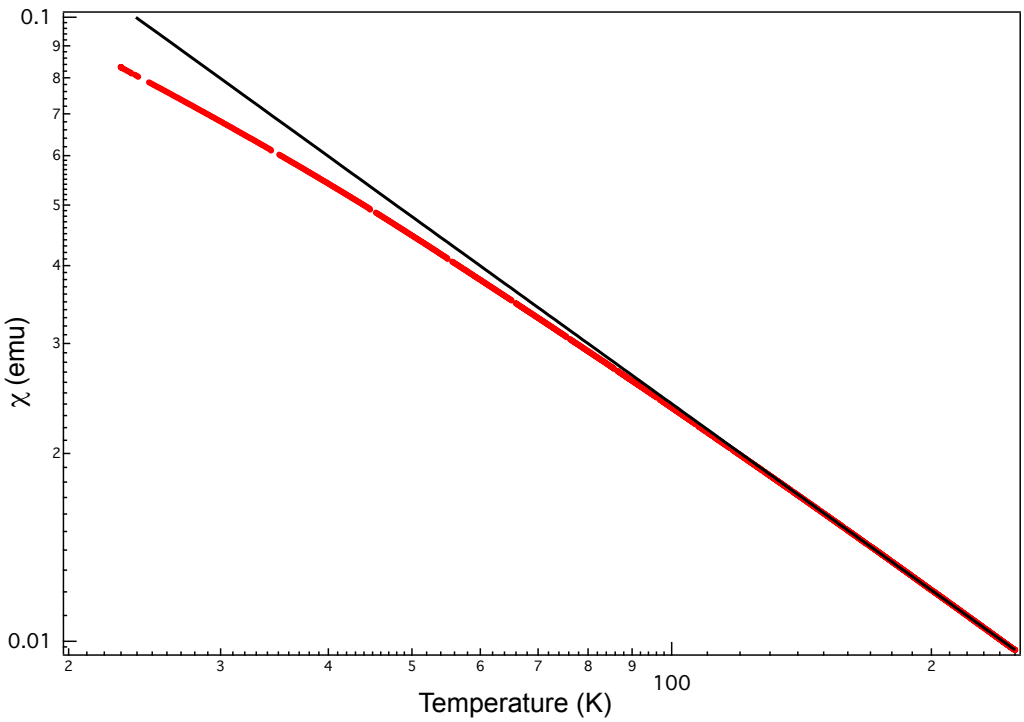

Figure 6.6: Temperature dependence of the magnetic susceptibility. The data (red) shows a clear deviation from the Curie-Weiss law [6] (black solid line).

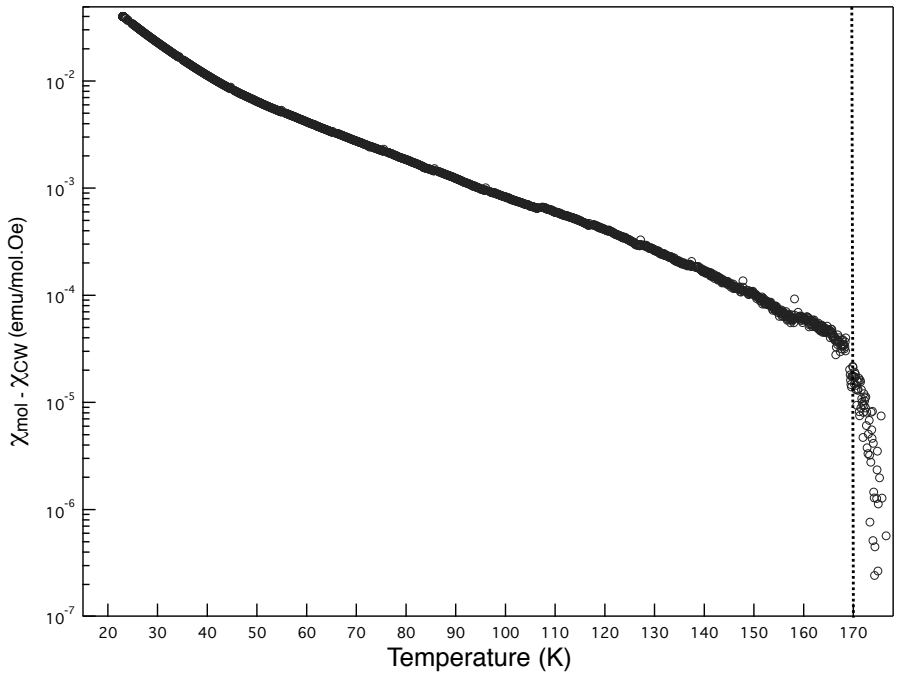

Figure 6.7: Plot of the difference between the magnetic susceptibility and the Curie-Weiss law. The plot shows the change in trend at $T \sim 165$ K.

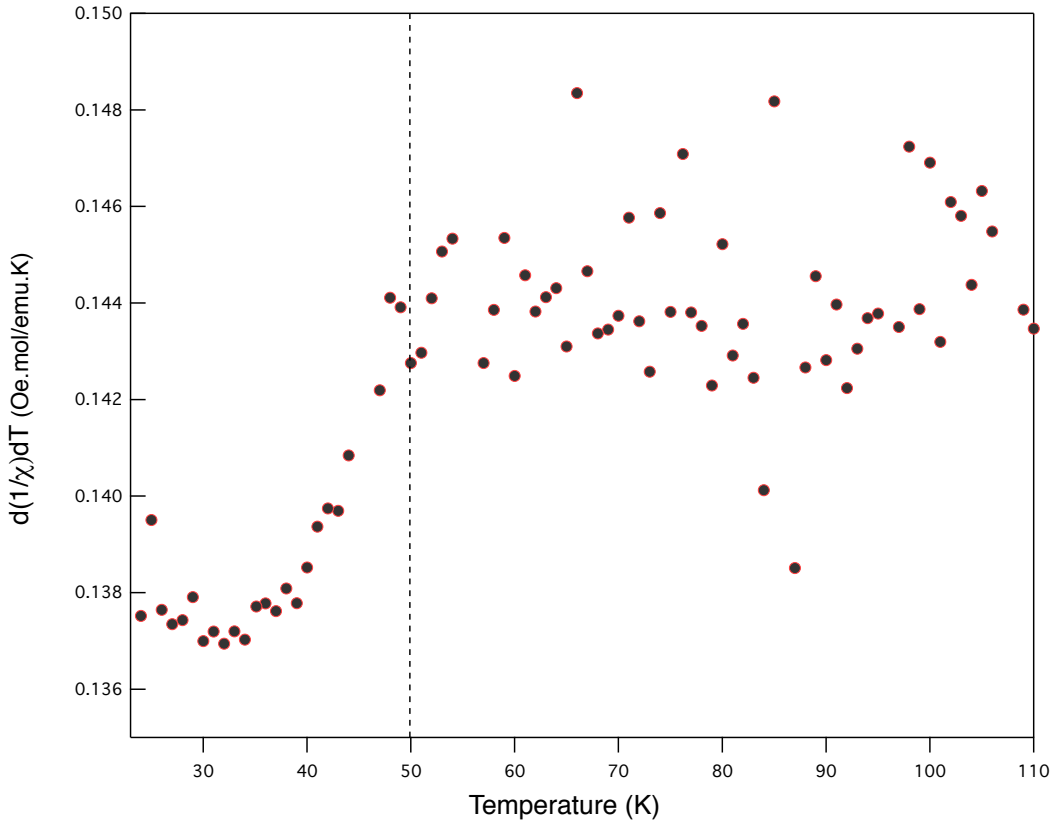

Figure 6.8: The first derivative of $1/\chi$ with respect to temperature, as a function of temperature. The plot reveals another anomaly at 50 K of unknown origin.

This further low temperature anomaly, occurs at around 50 K and can be seen more clearly by plotting the first derivative of the susceptibility with respect to temperature, which is shown in figure 6.8. These preliminary results indicate the existence of two magnetic anomalies, one at 165 K and a second one at 50 K whose origin cannot be understood from the susceptibility measurements alone. To corroborate these results, we have performed muon measurements on the sample to check for anomalies at the temperatures at which changes can be observed in the susceptibility data.

6.4 Muon measurements on $Ba_4Dy_{0.87}Nb_{10}O_{30}$

The muon measurements performed on this material are at the core of the investigation of the magnetic properties as well as the multiferroic behaviour (electric field control of magnetism) of the compound. Despite the fact that many measurements have been

made in order to have a clear view of the type of magnetism we are dealing with, the magnetism in this material has proved to be far from trivial and has made us rethink many of our initial conclusions based on the susceptibility measurements. Following, I will give a detailed description of the data collected on numerous experiments on this and other materials of the same series, the analysis of the data and finally, I will include a detailed discussion about the potential magnetic mechanisms that could explain the data we have collected.

6.4.1 ISIS muon data

In order to further investigate the magnetic properties of this material, we performed muon spin rotation (μSR) measurements in zero magnetic field (ZMF), using the EMU instrument at the ISIS Pulsed Muon and Neutron Source [86].

6.4.2 Experimental set up

To performed the experiment, a new sample holder had to be designed so that electric field measurements could be performed on the sample. The $Ba_4Dy_{0.87}Nb_{10}O_{30}$ sample (figure 6.9) was shaped into a 19 mm diameter disk of thickness 0.59 mm. The disk was then clamped between an aluminium rear plate and a 50 μm thick titanium foil. The titanium foil was thin enough to ensure that all of the muons stopped in the sample. By applying large voltages to the two plates, an electric field of up to 80 kV/cm could be applied in order to investigate the coupling between the ferroelectricity and magnetism of the sample, using muons. The figures below (6.10, 6.11, 6.12, 6.14, 6.13) show pictures as well as schematic diagrams with detailed descriptions of the sample mounting and the overall set up for the experiment.

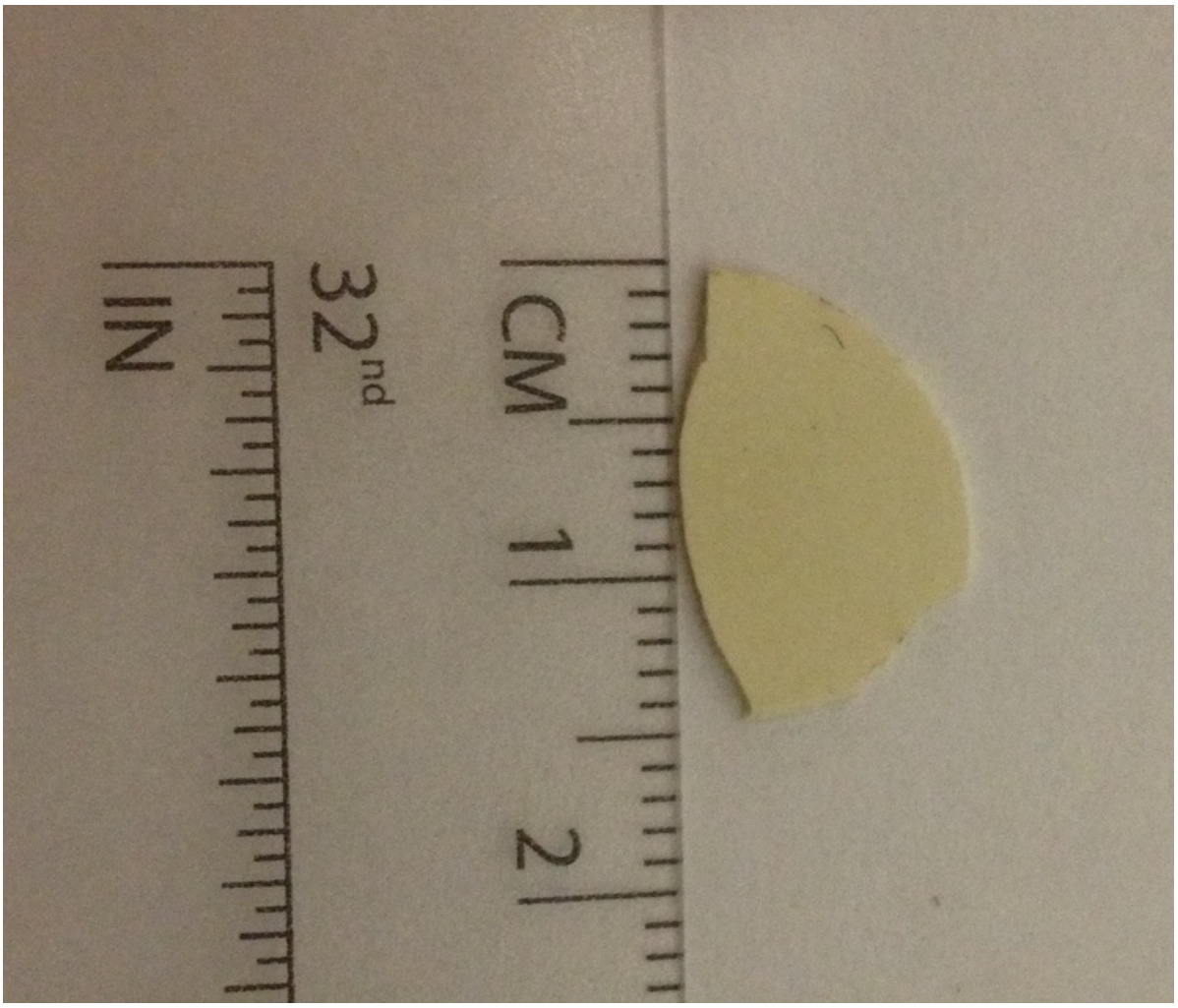

Figure 6.9: A fragment of the $Ba_4Dy_{0.87}Nb_{10}O_{30}$ sample. The sample used for our μ SR measurements was originally a 19 mm diameter disk, but because of the other series of measurements that had to be performed, the disk was cut into a number of fragments

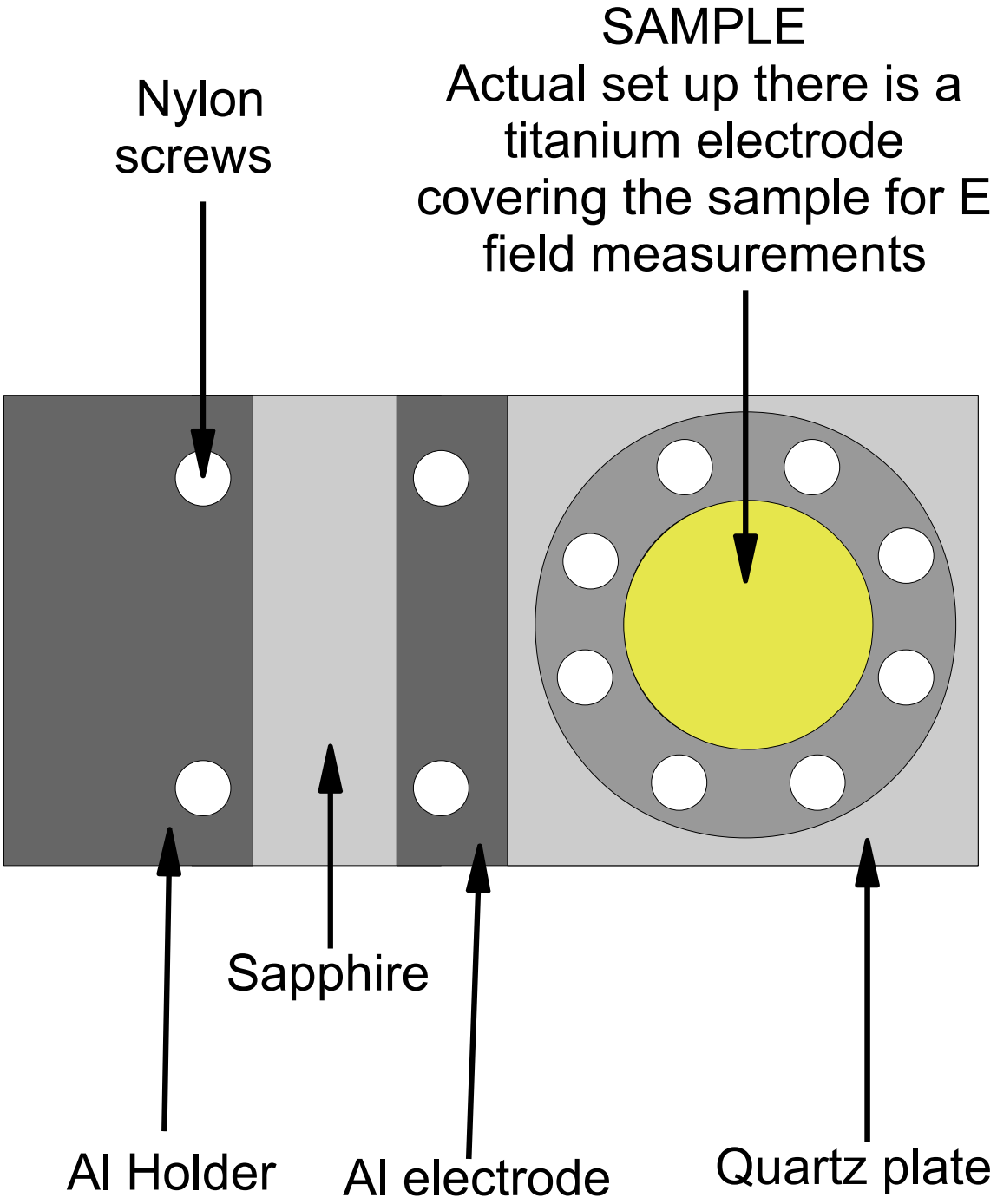

Figure 6.10: 2-dimensional sketch of the sample holder used for the muon experiments as seen from above. For the electric field experiments, a titanium disk is clamped between the clamping ring and the sample (see figures below)

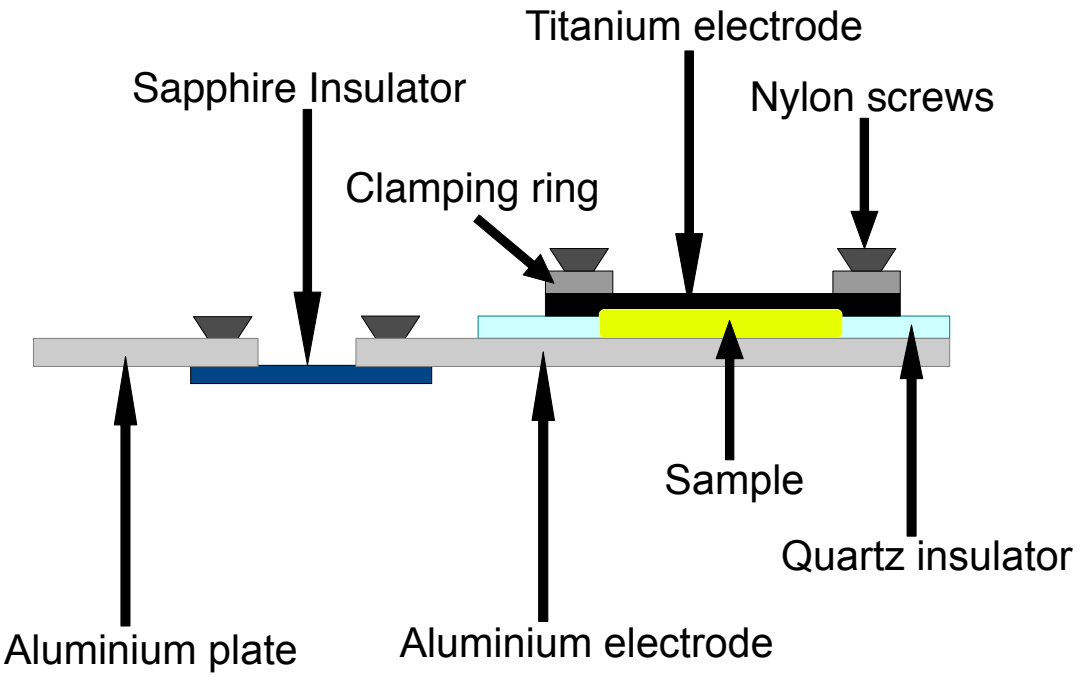

Figure 6.11: 2-dimensional sketch of the sample holder used for the muon experiments (side view).

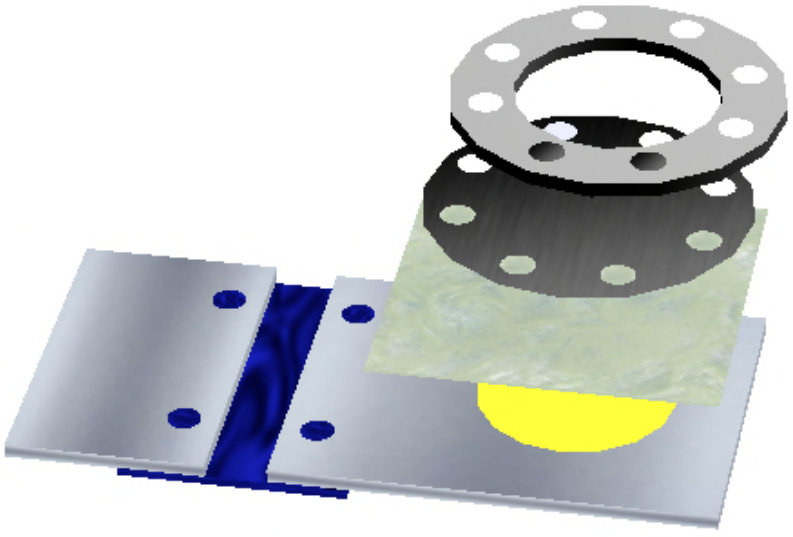

Figure 6.12: 3-dimensional sketch of the sample holder showing the mounting of the sample onto the holder.

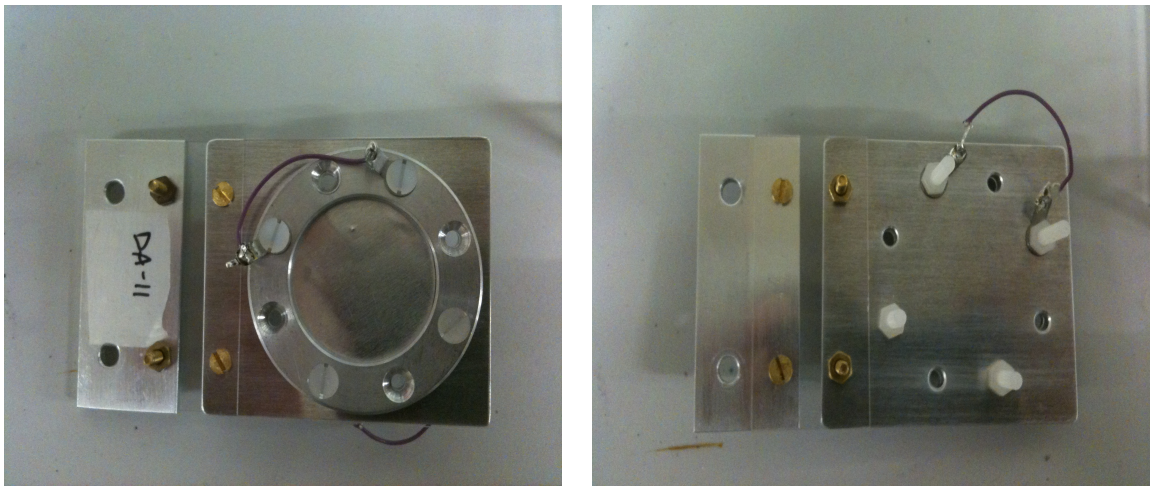

(a) (b)

Figure 6.13: a)A picture showing what the front of sample holder looks like after mounting the sample. The wires for the electric field experiments can be seen in the picture. b)The back of the sample assembled sample holder showing the Sapphire plate used as electrical insulator.

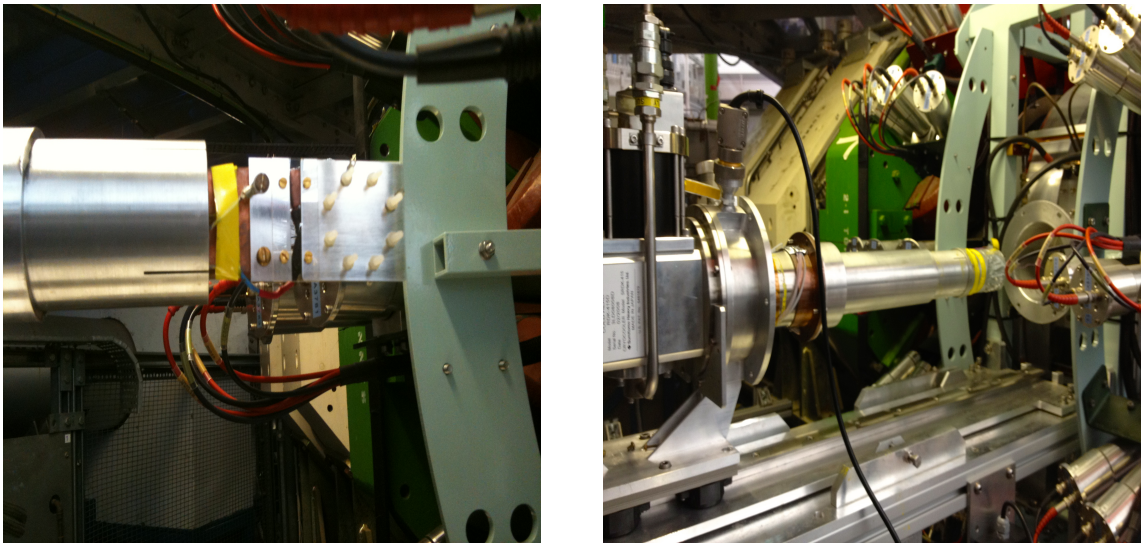

(a) (b)

Figure 6.14: a)Sample holder mounted on the sliding arm of the EMU instrument. b)The picture shows the sample holder covered with the Aluminium window ready to be inserted into the cryostat to start the measurements.

6.4.3 Analysis of the μSR data

To start with, we characterised the magnetic ground state of the material. Figure 6.15 shows representative spectra obtained in both, zero magnetic and electric fields (ZMF and ZEF), prior to the application of either field. Following the evolution of the relaxation data with temperature immediately reveals that there are several components to the signal at low temperatures, comprising a damped oscillation and a separate relaxation. This tells us that for this material, there are at least two different muon sites, corresponding to the oscillation and the separate relaxation. While the oscillating component is from a single muon site (or a number of magnetically equivalent muon sites), the relaxation component may be composed of several signals from different sites within the main phase, impurities or disorder as a result of the non-stoicheometry of the compound.

We note that $DyNbO_4$ is the only impurity in our sample that is magnetic; it is an antiferromagnet with a $T_N = 1.6$ K [166], above which it is paramagnetic. We therefore conclude that the oscillation in the data comes from the sample's main phase, namely, $Ba_4Dy_{0.87}Nb_{10}O_{30}$. It is immediately clear from the data that the muons are precession at a relatively low frequency, suggesting that either the associated muon site is a considerable distance away from any Dy^{3+}, or that it is situated at a nearly magnetically symmetric location. From the high temperature data in figure 6.15, it is also clear that the relaxation is Kubo-Toyabe like, related to the presence of randomly oriented nuclear moments [170]. The solid lines in figure 6.15 therefore show fits to the time dependent experimental data, with the following function

$$A(t) = A_0 \left[f_1 \, e^{(-\lambda_{rel} t)^\beta} + f_2 \left(\frac{1}{3} + \frac{2}{3} cos(2\pi F t + \phi) \right) e^{(-\sigma_{osc} t)^2} + f_3 \, G_{KT}(t) \right] + A_{BG} \quad (6.2)$$

The model used to describe the above data consists of 3 different fractions including an oscillating component that is only visible below 165 K. In equation 6.2, the first term with a fraction f_1 describes a relaxation process that is present at all temperatures. The

stretched parameter β is necessary to fit and describe the ISIS data, and it is often used to describe either a distribution of spin fluctuations timescales, quasi-static disorder or more than one muon site contributing to the signal. For our analysis, it is likely the latter.

The second term with a faction of f_2 represents the static or quasi-static ordered electronic moments, or short range correlations that give rise to the oscillation observed in the data. In this term, F corresponds to the precession frequency of the muons, which is directly proportional to the internal field at the muon stopping site, σ_{osc} represents the level of disorder and ϕ represents the phase of the muon's initial spin direction. This oscillating term is only visible in the data below 165 K, and f_2 is fixed to zero above this temperature.

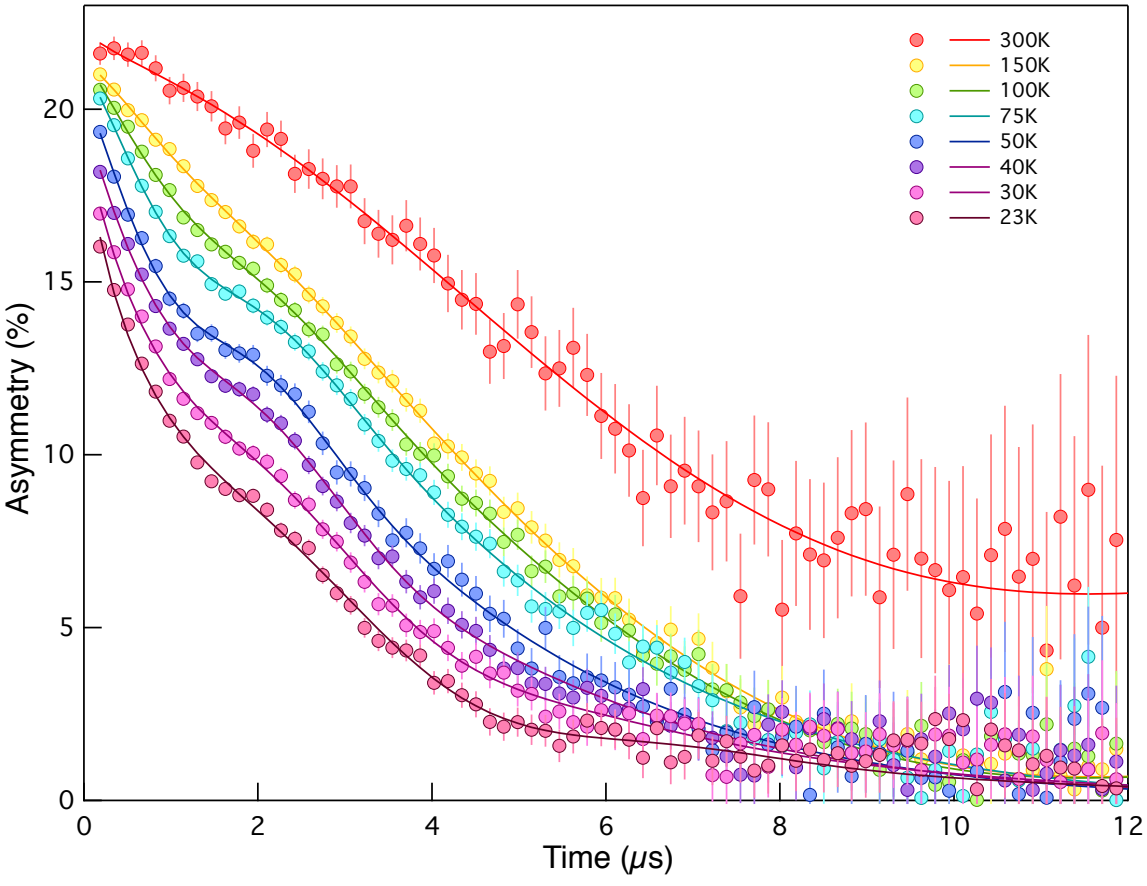

Figure 6.15: ZMF muon spectra as a function of temperature, where a clear oscillation develops at low temperatures consistent with the susceptibility data in figure 6.6

The third term with a fraction f_3 corresponds to the randomly ordered quasi-static nuclear moments and is only present at high temperatures, being fixed to zero below 165 K.

We note that even at 300 K it is not possible to fit the data to a single Kubo-Toyabe function which is expected from random orientations of quasi-static nuclear moments; the relaxing component f_1 must be included to properly fit the data representing a relaxation from muons experiencing weakly fluctuating electronic moments. Finally, to account for signals coming from a proportion of muons that miss the sample, implanting instead in the metallic parts of the sample holder, a background fraction was included, fixed to $f_{BG} = 0.05$ for all temperature, corresponding to the value obtained to fits at high temperature data.

Figures 6.16, 6.17, 6.18 and 6.19, are the fitted parameters at different temperatures for the data presented in figure 6.15. The internal field below 160 K (figure 6.16) follows a smooth increase with decreasing temperature, signalling the first transition which is also observed in the susceptibility data, but at $T \sim 50$ K, there is an unexpected departure from this behaviour. Similarly, the relaxation rate σ_{osc} (figure 6.17) displays a relatively constant (flat) behaviour until it reaches $T \sim 50$ K, below which it begins to significantly lower. For the non-oscillating component (figures 6.18 and 6.19), we find that the stretch parameter β slowly increases from around 0.5 at room temperature to around 1.5 at $T \sim 50$ K, below which it reduces again to 0.5. Furthermore, λ_{Rel} increases at 160 K, where there is then a plateau until $T \sim 50$ K. There is then a dramatic rise in λ_{Rel} as the sample is cooled below $T \sim 50$ K.

We therefore conclude that in addition to the first anomaly at ~ 165 K, a second magnetic anomaly takes place at around $T \sim 50$ K, with the most notable change being in the oscillation frequency. This shows that there is a significant reduction in the internal field experienced by the muons, the origin which requires further scrutiny and discussion.

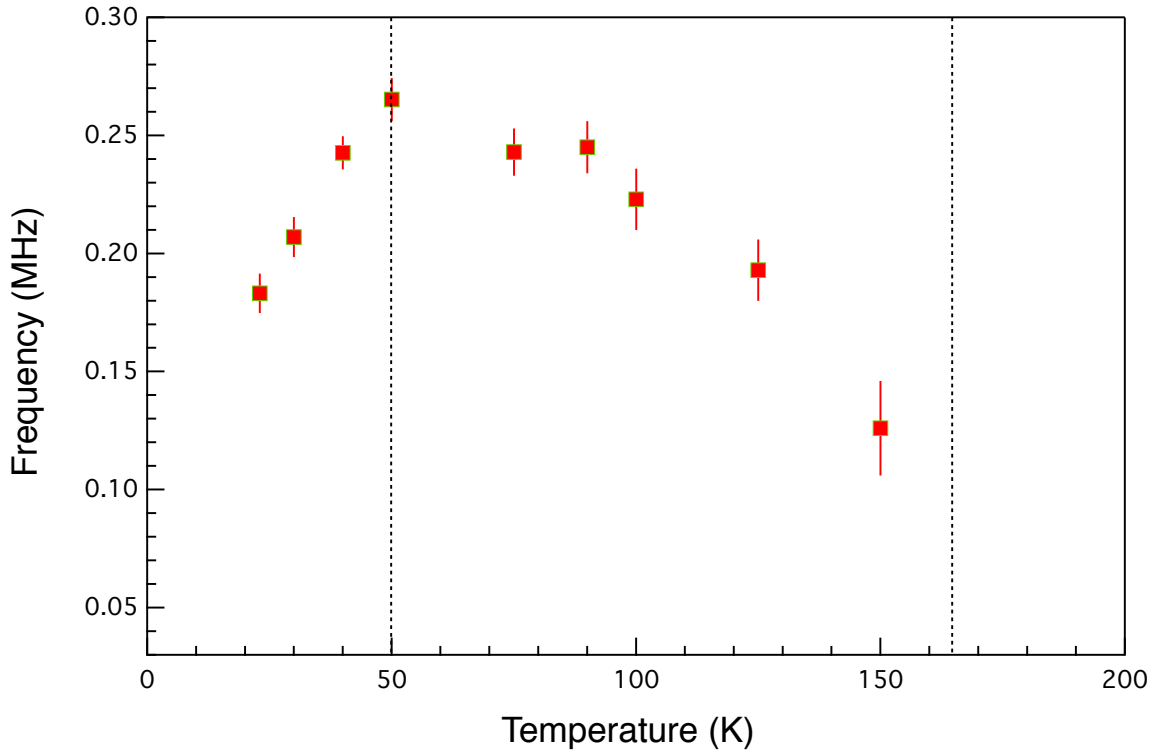

Figure 6.16: The frequency of the oscillating component as a function or temperature, with a transition temperature of $\sim$ 165 K. The expected trend deviates from the expected behaviour below 50 K, which is consistent with the anomaly observed in figure 6.8.

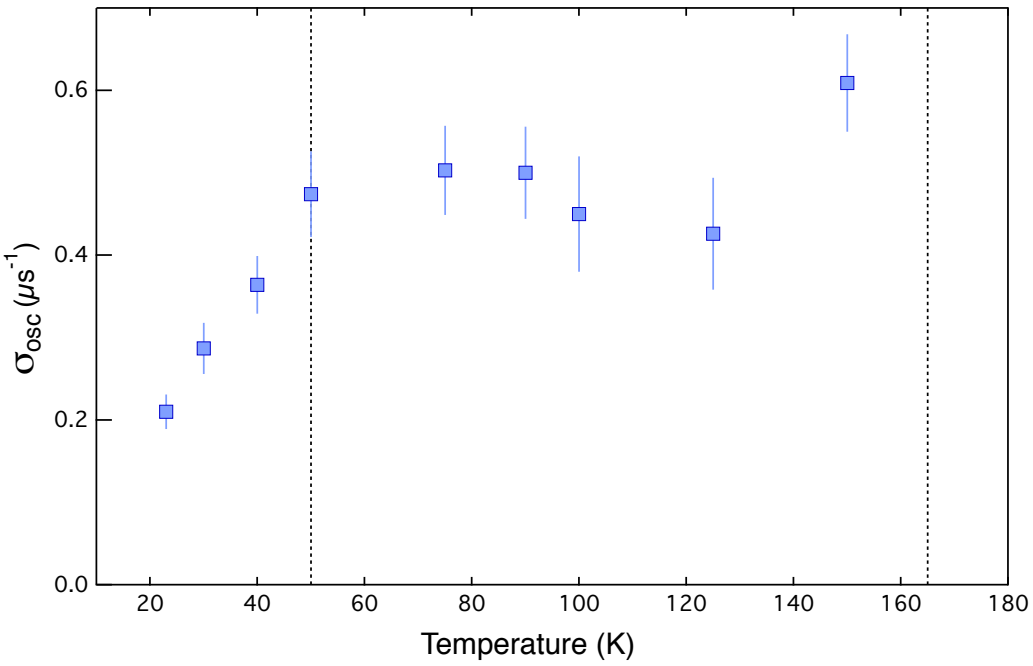

Figure 6.17: The relaxation rate of the oscillating component, also indicating a magnetic anomaly at 50 K.

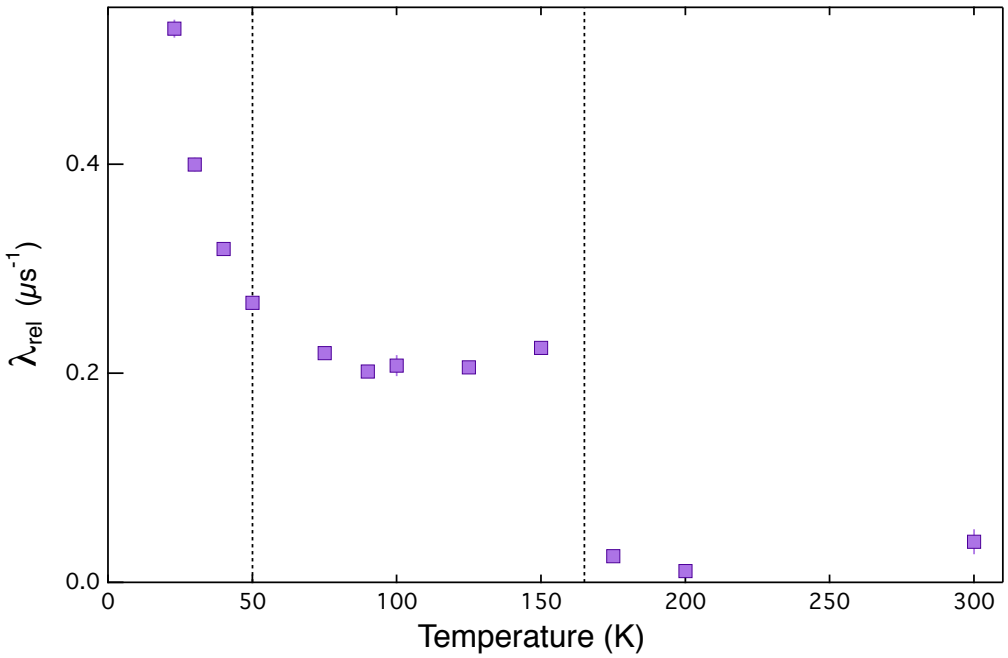

Figure 6.18: Relaxation rate of the non-oscillating component, also showing magnetic anomalies at 50 and 165 K.

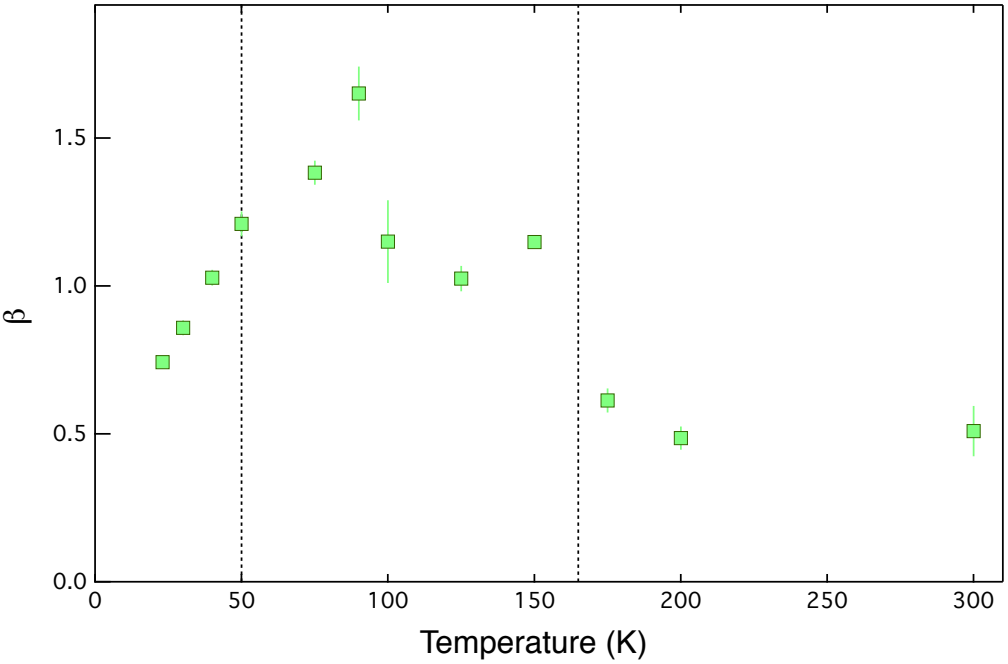

Figure 6.19: The stretch parameter

6.5 Magneto-electric coupling in $Ba_4Dy_{0.87}Nb_{10}O_{30}$

The fact that this material exhibits both, magnetic phenomena and ferroelectricity, and that there also is a clear coexistence between the two phenomena, to investigate any possible magneto-electric coupling we have performed ZMF μSR measurements at 40 K in an applied electric field. Figure 6.20 shows a plot of oscillation frequency as a function of applied electric field. From the figure, it is immediately obvious that the muon's precession frequency, and therefore the internal field of the sample, is systematically modified by the application of the electric field. As the electric field was increased from zero to 60 kV/cm (blue points and arrow showing the direction), the internal field gradually increases as the polarisation of the material increases. The electric field was then increased to $\sim$ 75 kV/cm polarising the sample further but which unfortunately also led to dielectric break down. The sample was therefore removed, inspected and lucky for us, the damage was at the very edge of the disk (the damage was identified as a black spot at the edge), which allowed us to remove the region of breakdown without compromising the rest of the sample. Once the damage was removed, the sample was remounted and placed in the cryostat to continue with the measurements (red data points). As can be see in the figure, the remounting procedure of the sample did not affect the observed frequency, further indicating that the majority of the sample was unaffected by the localised damage due to dielectric breakdown. On reducing the electric field further (red points and arrow showing the direction of field change), it is clear that the internal field remains relatively flat until the electric dipoles begin to switch to the opposite polarisation, at negative fields. Unfortunately, leakage current limited the applied voltage to -40 kV/cm, so we were unable to perform a symmetrical hysteresis loop. As a consequence, the muon's precession frequency at -40 kV/cm has almost the same value as before applying any electric field to the sample, suggesting that there is only a small net alignment of the electric dipoles. Nonetheless, as we increased the electric field again, the internal field remains flat (green points and arrow showing the direction of electric field change) until the polarisation again begins to switch, where the internal magnetic field increases.

Whilst the clear hysteretic behaviour of the internal magnetic field with applied electric field at 40 K, (as shown in figure 6.20), rules out many direct effects that the electric field might have on the positively charged muon, one must nonetheless be careful in coming to any firm conclusions without further confirmation. For this reason, we performed a similar hysteresis loop at 75 K. This 35 K difference in temperature should not radically change the role that the electric field has on the positively charged muon, but the magnetism at this temperature is considerably different as it is above the temperature at which the is clear change in the magnetism and one might expect there to be a difference in the coupling between the two phenomena. This is shown in the inset to figure 6.20, where it is clear that the electric field dependence is considerably reduced if not completely absent, thus ruling out any potential role that the electric field has on the muon itself. The hysteretic effects can then only be explained by a direct magnetoelectric coupling in this material. Despite this convincing evidence, two questions remain: Does the sample holder itself play a role on the coupling? Will the electric field have an effect on a sample of different stoichiometry?

The bulk of the analysis concerning the role that different sample holders play on the muon signal will be dealt with in a different section. However, since those measurements also involve electric field experiments its more adequate to discuss those results on this section. To answer these questions, we performed EF experiments on a sample with different chemical composition and also, a different sample holder (see section 6.6 for further details) The electric field experiments were performed on $Ba_{3.2}Dy_{1.8}Ga_{0.9}NbO_{30}$ and they reveal an interesting result. Figure 6.21 shows a plot of the relaxation rate λ as a function of temperature, using the shapol holder masked with silver. To show the effect an applied electric field has on the relaxation, the figure shows the relaxation rate at zero (already shown in figure 6.32), as well as applied electric field. Interestingly, under an applied the electric field the behaviour of the data changes. At high temperatures ($T > 50$ K) the data shows the same trend for both, zero and applied fields. But below 50 K, while at zero applied field the relaxation increases, an applied field seems to somehow modify the material causing first a drop in the relaxation followed by an increase to roughly the

same value of relaxation as that obtained at 50 K. We are therefore convinced that the hysteresis shown in figure 6.20 is indeed coming from the sample. i.e. the sample shows intrinsic ME coupling.

This change in the relaxation rate as as result of an applied electric field, gives yet more evidence that there is a strong coupling between the ferroelectric and magnetic properties of the material. Furthermore, the fact that these changes occur below 50 K, regardless of what sample holder is used, suggest that the transition at 50 K is somehow related to the anomaly below this temperature, that can in turn be tuned with an electric field.

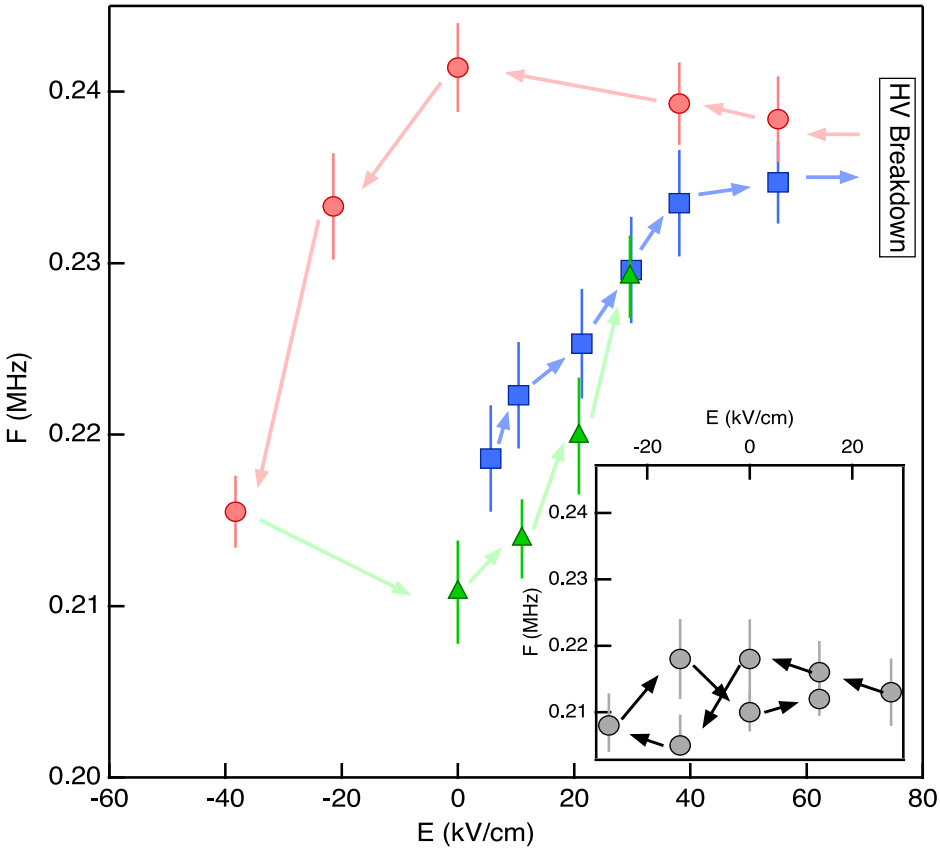

Figure 6.20: A hysteresis loop of the internal field measured by the muon in an applied electric field performed at 40 K. Blue points are the starting brach of the loop, the red points are as the electric field is reduced from the maximum applied field and the green pints are the electric field increasing again. The coloured arrows show the direction in which the electric field is changed. The looped arrow indicates the highest electric applied field and point at which the sample suffered dielectric breakdown. Inset: the internal field measured with the muons as a function of electric field at 75 K, plotted on the same y-axis scale as the main panel. the arrows show the direction in which the electric field was changed. no hysteresis or systematic change in the internal field can be observed.

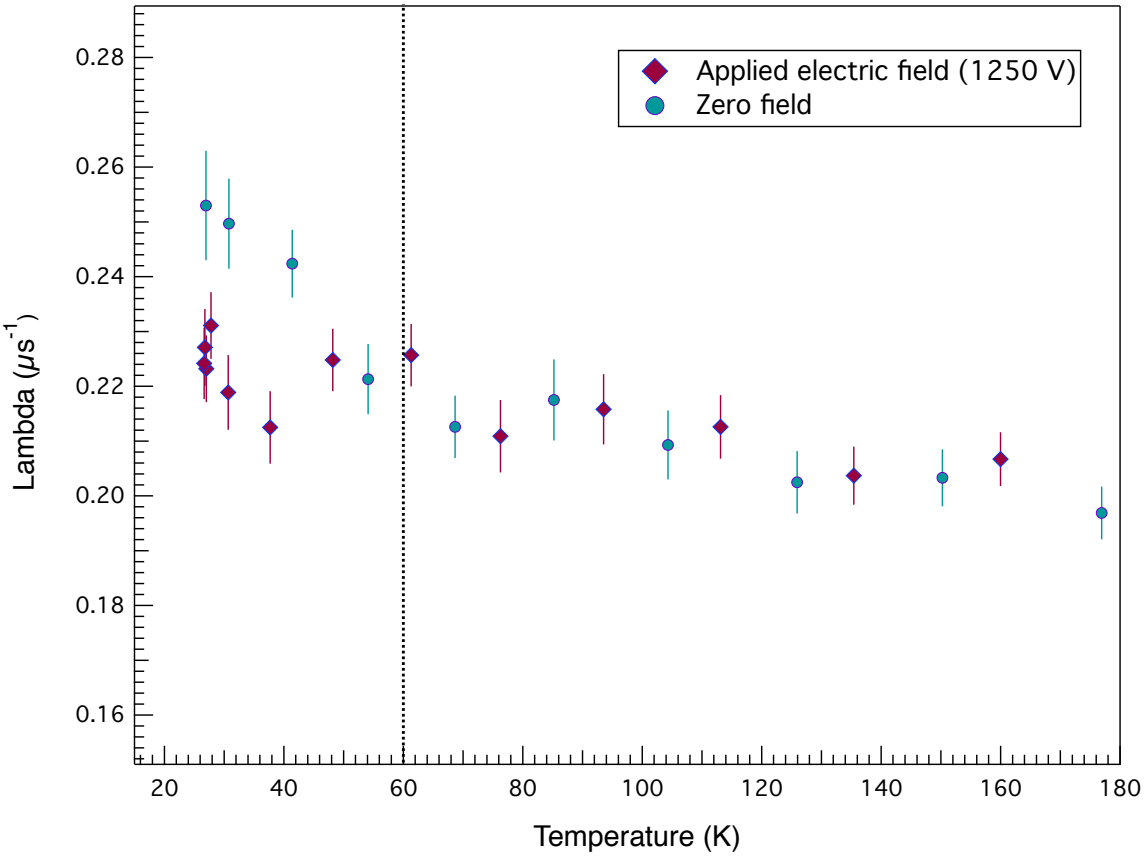

Figure 6.21: Plot of the relaxation rate versus temperaure for $Ba_{3.2}Dy_{1.8}Ga_{0.9}NbO30$ in both, zero and applied electric field. There is a clear change in the relaxation below 50 K when the electric field is applied

6.5.1 RUS measurements

Many of the potential ME coupling mechanisms are highly dependent on the crystallographic orientation and symmetry with respect to the applied electric field, which one would naively think should not result in a coherent change that is observed in the data. One of the most pertinent examples is coupling mediated by strain [171], where for example the crystallographic unit cell shape or size alters under an applied electric field due to the piezoelectric effect, which in turn alters the magnetism. We note than in order to observe a chance in frequency, every muon at the relevant site should experience the same change in internal field. This implies that the ME coupling mechanism is not mediated via the crystal structure, as our material is polycrystalline, although we are unable to rule it out entirely. A strain coupling mechanism could occur if the magnetic and fer-

roelectric order parameters each coupled with spontaneous strains that then overlapped. Strain/order parameter coupling of this type can give rise to changes in elastic constants of 10's of percent [172]. Therefore, to completely rule it out, we have investigated elastic and an elastic relaxations associated with the magnetic and ferroelectric phase transitions using Resonant Ultrasound Spectroscopy (RUS) on the same sample as was used for the muon measurements.

I carried out the RUS measurements with the guidance of Professor Michael Carpenter using the RUS instrument at Cambridge University. For this study, the sample was an irregular fragment of a thin polycrystalline disc, ~ 0.6 mm thick and weighing 0.047 gm. Spectra ($50,000$ data points, $10 - 1200$ kHz) were collected in a heating sequence at low temperatures using a helium flow cryostat. The sample sat with the two transducers against each of the large faces in an atmosphere of a few mbar of helium gas. Temperature was monitored using a silicon diode, and a period of 10 minutes was allowed for thermal equilibration at each temperature before data collection. High temperature spectra ($65,000$ data points, $50 - 1200$ kHz) were collected in air in both heating and cooling sequences, with the sample held lightly across a pair of corners between the tips of alumina rods protruding into a horizontal resistance furnace. In this case a period of 15 minutes was allowed for thermal equilibration at each temperature. Spectra were analysed offline using the software package Igor (Wavemetrics). Individual resonance peaks were fit with an asymmetric Lorentzian function, as illustrated for a peak near 360 kHz in figure 6.22 for successive spectra collected between 808 K (top spectrum) and 289 K (bottom spectrum).

Figures 6.24 and 6.23, show results from the frequency, f, and the inverse mechanical quality factor, Q^{-1}, for individual mechanical resonances in the vicinity of 0.4 MHz, for the low and high temperature runs respectively. $1/f^2$ scales with elastic compliance, which is analogous to permittivity in a dielectric experiment, and Q^{-1} is a measure of acoustic loss analogous to the dielectric loss, $\tan\delta$. Strikingly, there is no detectable change in compliance at the ferroelectric transition (figure 6.23), signifying essentially no strain relaxation. Similarly, there are no obvious changes in compliance associated with

the magnetic anomalies at ∼50 K and ∼165 K (figure 6.24), and the only evidence for any influence on the elastic behaviour is very small anomalies in Q^{-1} at these temperatures. An importance difference between the TTB structure and the perovskite structure in this context, is perhaps the flexibility with respect to accommodating shear strains by polyhedral rotations. In a non-cubic perovskite shearing is easily achieved via rotations of the corner sharing octahedra against each other analogous to displacements involved in rigid unit modes [173]. The more complex arrangement or corner sharing octahedra with two distinct octahedral sizes, such as occurs in the TTB structure, might provide bracing against such easy (low energy) displacements with the result that any strain coupled to ferroelectric and magnetic ordering is constrained to be small.

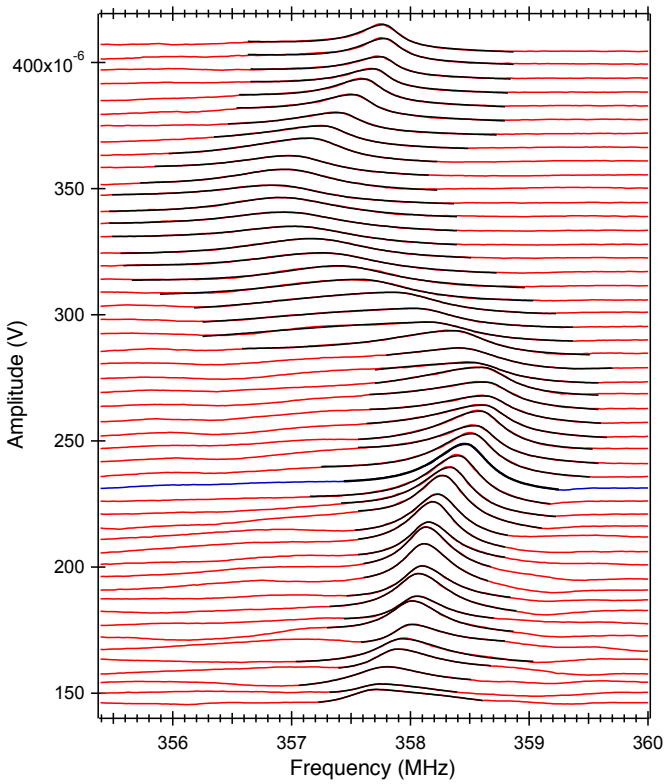

Figure 6.22: Segments of spectra collected at high temperature, illustrating fits to individual resonance peaks. The vertical axis is amplitude, but the spectra have been offset in proportion to the temperature at which they were collected: top spectrum= 808 K, bottom spectrum= 289 K.

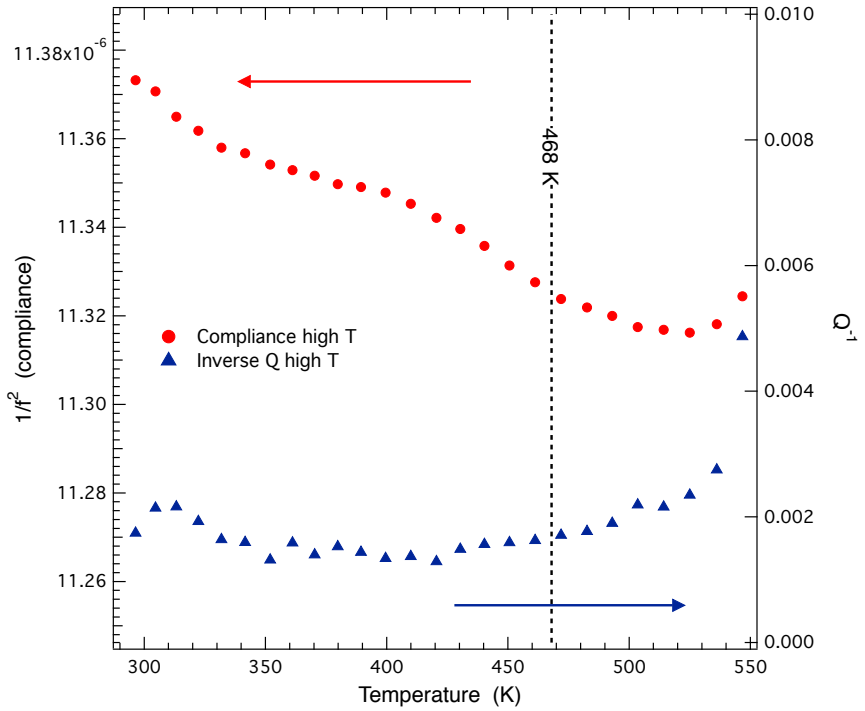

Figure 6.23: The compliance and the inverse mechanical quality factor, Q^{-1}, as a function of temperature, using the high temperature RUS configuration. No change in the compliance can be observed at the ferroelectric transition temperature.

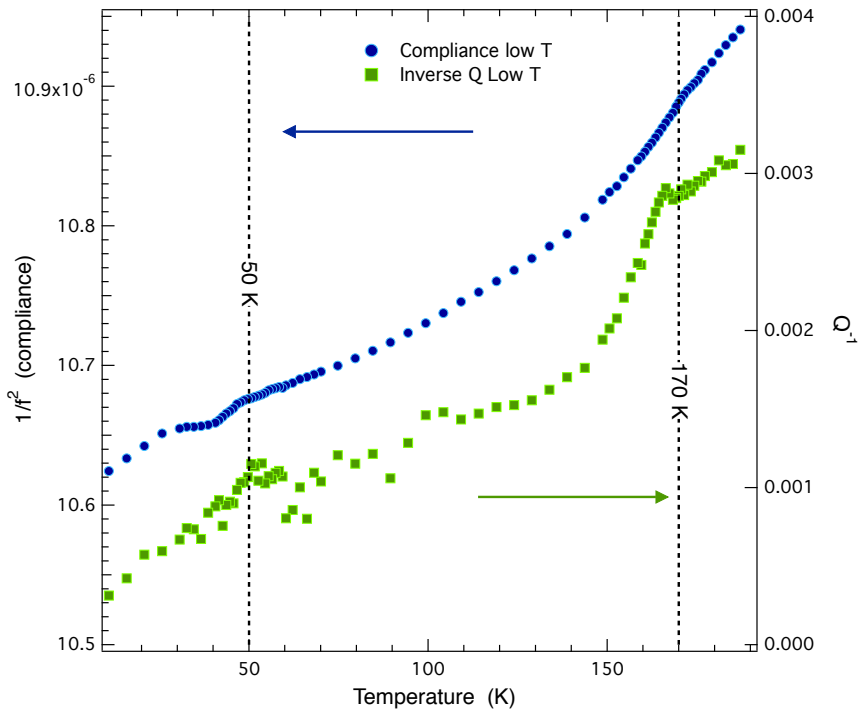

Figure 6.24: The compliance and the inverse mechanical quality factor, Q^{-1}, as a function of temperature, using the low temperature RUS configuration. Small anomalies in Q^{-1} can be observed at 50 and 165 K.

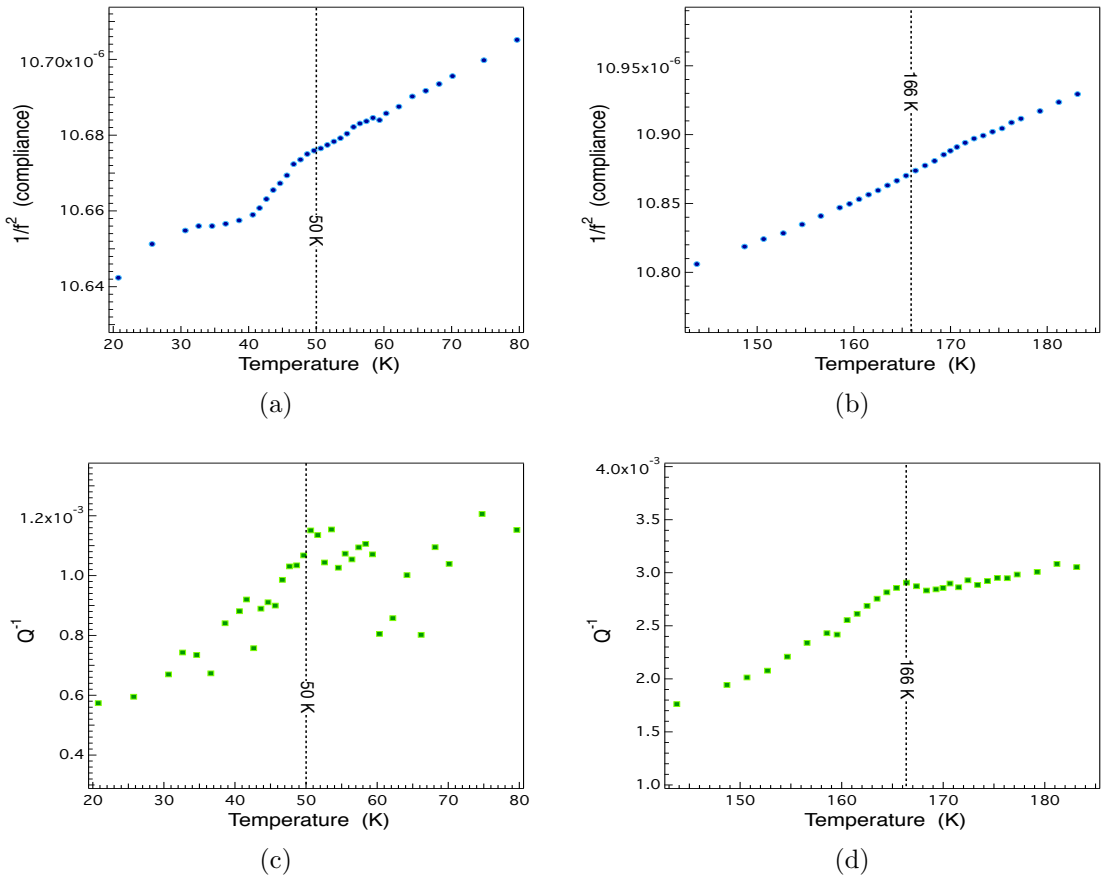

Figure 6.25: Figures a and b show zoomed in regions in the compliance, and figures c and d on Q^{-1}, as shown in figure 6.23 at 50, and 170 K respectively, to show more clearly the subtle changes in both variables at these temperatures.

6.6 Discussion

All the work and the analysis on the ZF muon data for this compound, as well as the way in which the electric field experiment has been analysed and interpreted, has been under the assumption that the muon is undergoing a low frequency spin precession as a result of the internal field it is experiencing. Although a muon spin precession may imply the existence of long range order, the fact that the magnetism in this material has low dimensionality (1D chains) and that the magnetic species within the chains is a rare earth (Dy) makes this long range magnetic ordering scenario very unlikely. In order to have a better understanding of the magnetic structure of our material and completely rule out long range order, we decided to perform magnetic neutron scattering measurements. The

sample on which the neutron measurements were performed had a nominal composition $Ba_4Dy_{0.87}Nb_{10}O_{30}$. However, detailed chemical analysis was not performed as it was meant to be a quick check on whether the material had long range ordering. The neutron scattering experiment was performed using the WISH instrument at ISIS. The WISH instrument is a long-wavelength diffractometer designed mainly for powder diffraction experiments at long d-spacing in magnetic and large unit cell systems [174].

Figure 6.26 shows a plot of neutron intensity versus time of flight for $Ba_4Dy_{0.87}Nb_{10}O_{30}$ for different temperatures above and below 165 and 50 K, the temperatures where we see changes in the susceptibility and muon data. As can be seen from the figure, the spectra above as well as below these temperatures looks the same, and there is no evidence of any magnetic peaks developing or changes in intensity, which would be expected if indeed the material ordered magnetically. This also raised the question of whether or not the oscillation observed on the ZF muon data was in fact an oscillation or merely a sum of two different relaxations.

In order to determine whether the oscillation in the muon data is real, we re-analysed the ZF muon data using a number different models based only on relaxations, without including the oscillating component to test whether or not a good fit could be obtained. Figure 6.27 shows the raw data obtained at 50 K fitted with different models. Note that the fit in figure 6.27 A was obtained using equation 6.2, which as shown in the figure, results in a reliable fit to the whole data set, including the oscillation in question.

Starting with figure 6.27 B, this data was analysed with the function

$$A(t) = A_0 \left[f_1(G_{KT}(t) + e^{(-\lambda t)^\beta}) + f_2(G_{KT} + e^{-(\sigma t)^2}) \right] + A_{BG} \tag{6.3}$$

where we assumed that the signal consists of two different relaxations corresponding to a transition between low temperature, where the electronic moments dominate and a Kubo-Lorentzian relaxation gives the best description to the data, to a high temperature regime, where due to thermal fluctuations the interaction between electronic spins vanishes, nuclear moments dominate and the data is better described with a Kubo-Gaussian

relaxation. Although this model gives a simple and accurate explanation about what might be physically going on in the material, the model doesn't really fit the data properly.

It is very clear that the fit (solid blue line) in the figure, fails to produce a reliable fit in the region of $\sim$ 1.5 - 2.5 μs, which is the region where the oscillation is observed. Figures 6.27 C, D and E, were all fitted using the same assumption as with the fit shown in figure 6.27 B, but with different models on the relaxation. For instance, figure 6.27 C was fitted with a stretched exponential and a square Gaussian relaxation, figure 6.27 D with a stretched exponential and a lorentzian and figure 6.27 E with two stretched exponential relaxations.

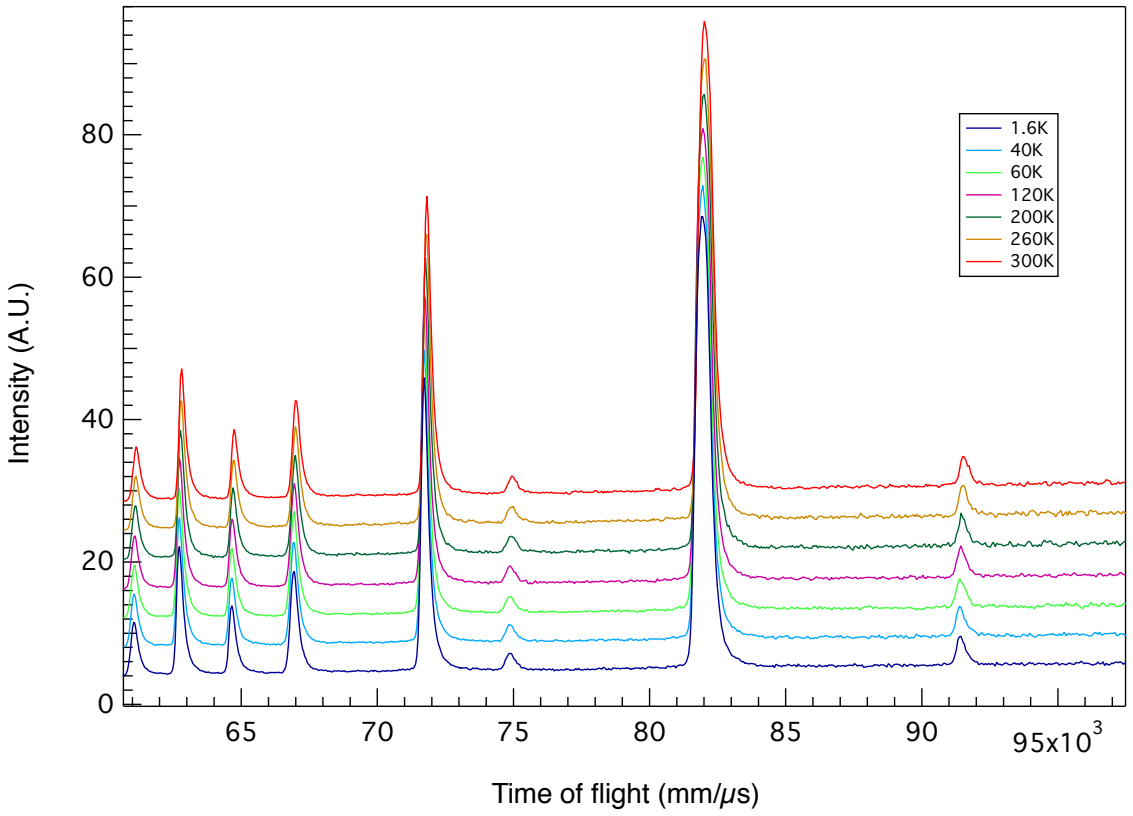

Figure 6.26: Neutron diffraction pattern of $Ba_4Dy_{0.87}Nb_{10}O_{30}$ at different temperatures. The data shows no evidence of extra peaks (magnetic peaks) or changes in intensity at low temperature, something that would be expected if there was a transition to long range order in the material below a well defined temperature.

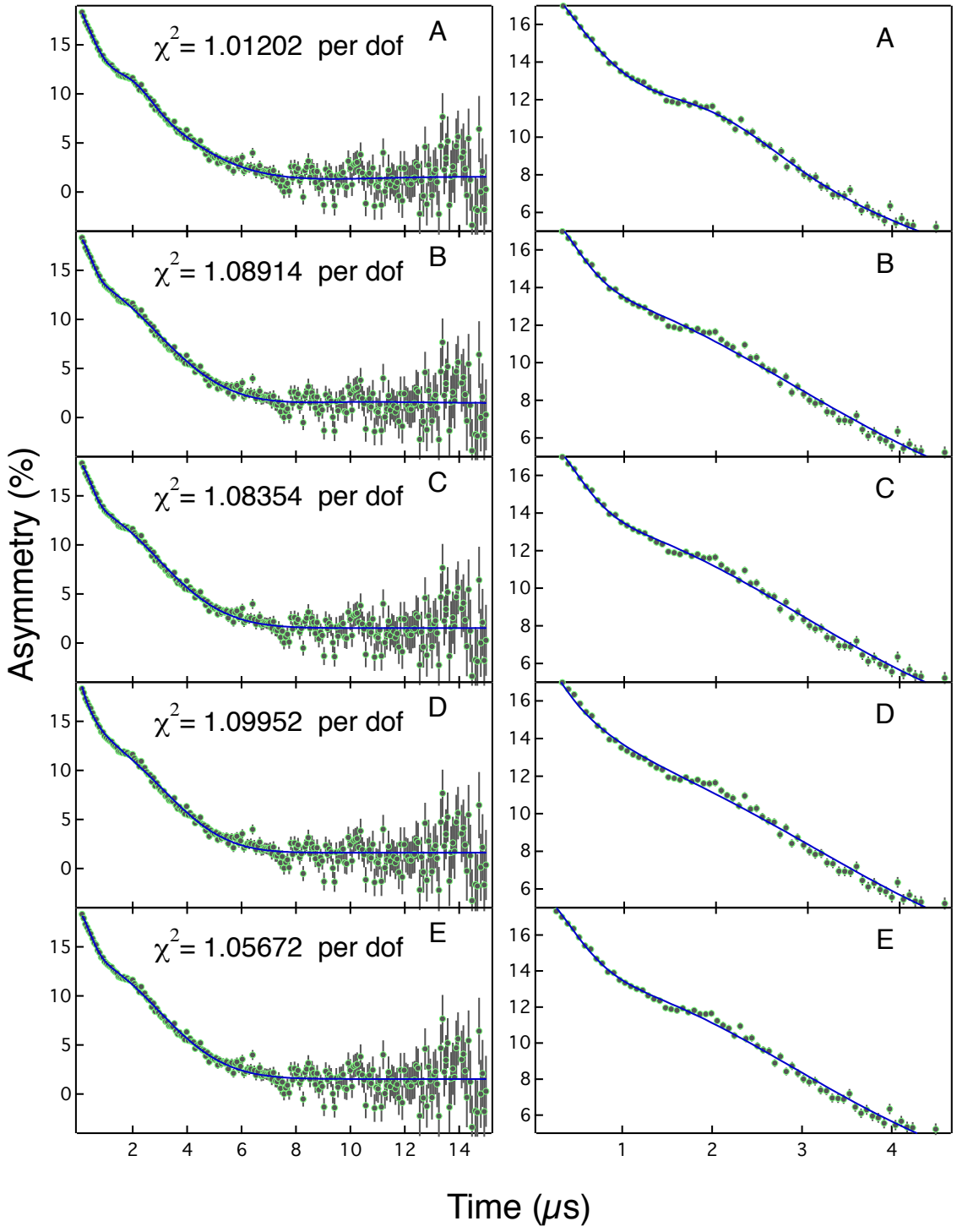

Figure 6.27: Figures A-E on the left hand side of the panel show ZF raw data of $Ba_4Dy_{0.87}Nb_{10}O_{30}$ at 50 K fitted with different models. The figures on the right hand correspond to a zoom in of the data at short times which is the area of interest in the plot. Figure A shows a proper to the data, obtained by assuming an oscillation at short times.

All of these models fit the data, but just as with the model in figure 6.27 B, they all fail to

give a reliable fit to the oscillation at short times. Note that these are just four examples out of about a dozen different alternative models we used to try and fit the data based on the transition between high and low temperature relaxations, but again, the models did not provide a proper fit to the data compared to that obtained when considering the oscillation.

Having analysed the data using many different models that failed to provide reliable fits, we concluded that the anomaly on the data that starts developing below$\sim$ 160 K is indeed an oscillation.

However, for our muon measurements at the ISIS facility, the sample holder we designed was composed of a series materials that would allow us to carry out the measurements in zero, as well as applied magnetic and electric fields (see figures 6.11 and 6.13). Although the holder design was well suited for our measurements, it raised the question of whether or not the experimental spectrum was somehow "contaminated" with signals coming from some other part of the holder, which would of course have a significant influence on the overall interpretation of the data. For most experiments, silver is the material of choice to mount the sample on to the sample holder as a result of silver having very low nuclear moments, which ensures a very low background signal coming from the holder itself. So to rule out any contribution to the muon signal coming from any of the components in our sample holder, we decided to repeat the zero field and applied electric field measurements using the original sample holder and an alternative sample holder to compare the signal and the fit parameters. For the alternative holder (a ceramic known as shapol), we used a silver mask in order to minimise any potential background signal coming from the sample itself.

Because of the number of muon measurements, as well as the other experiments that were performed on the original sample (some of the experiments required a small fragment of the sample, for example), the original sample was no longer suitable for further μSR measurements and hence, another sample of the same series, but different stoichiometry had to be used to test the effects of the holder, namely, $Ba_{3.2}Dy_{1.8}Ga_{0.9}NbO_{30}$. Since the aim of the experiment was to check the influence of the holder on the muon signal, the

sample change was not really an issue, as measurements of the new sample on different holders would give the information required to find whether the different holders would have a significant effect on the experimental spectrum. Figure 6.28 shows a schematic representation of the shapol holder used for this experiment. The simplicity of this set up made it easy to mask all the area around the sample with silver. To compare the results, a set up identical to that shown on figure 6.10 was used.

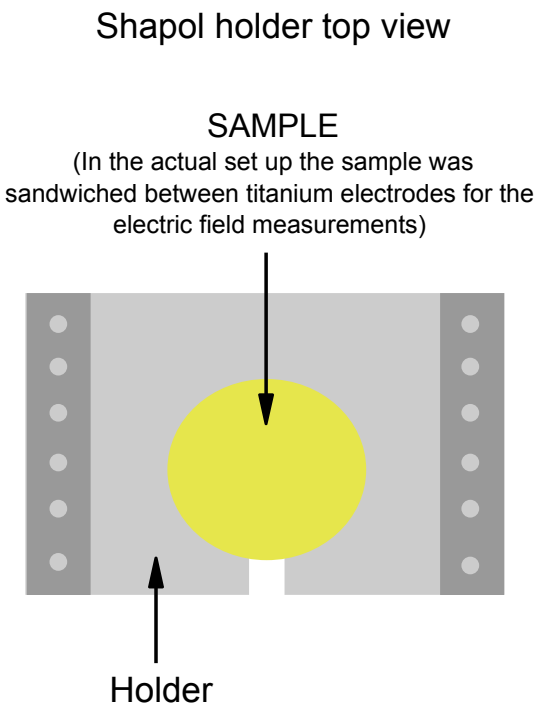

Figure 6.28: Shapol holder. For all the measurements, a silver mask was used to to cover the area around the sample and thus minimise the background signal coming from the sample holder. For the electric field experiment, titanium plates were used as electrodes.

The measurements were performed in the following set ups: For the original sample holder (figure 6.10), zero electric and magnetic field measurements (ZF) were performed with and without a silver mask. For the shapol holder (figure 6.28), ZF and applied electric field measurements were performed using a silver mask.

The data for both experiments was analysed using the following function:

$$A(t) = A_0 \left[f_1 e^{(-\lambda t)^\beta} + f_2 e^{-(\sigma t)^2} \right] + A_{BG} \tag{6.4}$$

where the second component with a fraction f_2 was only present at low temperatures

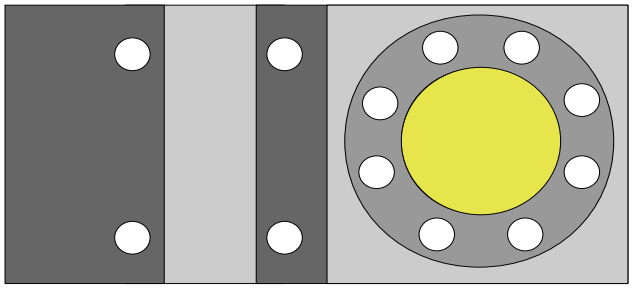

(a)

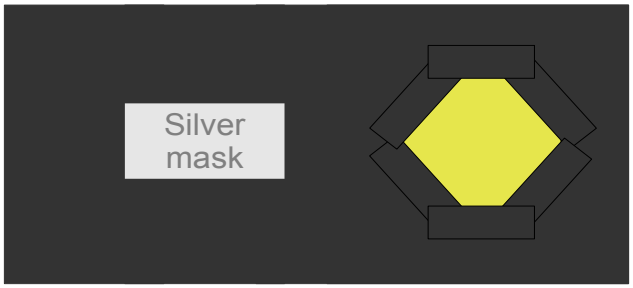

(b)

Figure 6.29: a) The original sample holder. b) The same holder masked with silver.

and made up only a small fraction of the overall asymmetry spectrum. We shall consider first the results with the original sample holder. Figure 6.30 shows the raw data at 50 K for the original sample holder with and without a silver mask. It is obvious from the two spectra that a faster relaxation rate is observed for the holder with no silver mask. The difference in initial asymmetry (amplitude) of the the two signals can be explained by considering how the sample holder was masked in order to perform the experiment. The fact that the sample was shaped into a disk and the silver mask had a square shape implies that the corners of the part of the holder within the mask were still exposed to the muon beam. Since the whole point was to isolate the holder signal, the mask had to be modified, that is, extra pieces of silver were placed in each corner of the mask, which meant that $\sim 40\%$ of the sample was also covered by the silver. As a result, the amplitude of the two signals differed because of the missing part of the sample and the influence of the silver mask on the signal itself. Figure 6.29 shows a schematic representation of the set up described above.

In figure 6.31, the corresponding relaxation rate, λ, is plotted as a function of temperature for both, the holder without a silver mask (blue markers) and with a silver mask (red

markers). At high temperatures, the relaxation rate shows a very similar behaviour. From room temperature down to $\sim$ 60 K, the relaxation rate is fairly constant. Below 60 K however, a dramatic increase in the relaxation rate can be observed, indicating the onset of the transition observed in the susceptibility data and muon data on the $Ba_4Dy_{0.87}Nb_{10}O_{30}$ sample (see figures 6.8 and 6.18).

Moving on to the shapol holder, in figure 6.32 the relaxation rate is plotted as a function of temperature in ZF. Fits to this data were obtained using the same function we used to fit the data collected for the original sample holder (equation 6.2), which provided a good and reliable fit, as shown in figures 6.34 and 6.35, where the asymmetry is plotted as a function of time for the data collected at 40 K and 100 K respectively. Note that the data in figure 6.34 shows a small anomaly at $\sim$1 μs that looks similar to the more pronounced oscillation in figure 6.15 at short times. For the ZF experiment, once again the data shows pretty much the same behaviour as that obtained with the original holder. The relaxation rate at high temperatures is relatively flat and constant, but at 50 K there is a clear deviation from this trend, and the relaxation rate undergoes a sudden increase, just as the one displayed with the data on figure 6.30 and 6.31. In figure 6.33 the relaxation rates for all the different measurements are plotted within the same figure so that the different sets can be compared.

Apart from the difference in amplitudes, there is no significant change in the signal as a result of the change in sample holder. What's more interesting, is the fact that regardless of the sample holder or sample stoichiometry we use for the experiment, the data shows consistency in terms of the temperatures at which changes can be observed. We therefore conclude that despite the slight deviations in the parameters, and the difference in amplitude of the raw data, the sample holder does not have a real significant effect on the signal and we can therefore be sure that the signal is indeed the result of muons stoping in our sample, and that any changes in the signal with temperature are not related to the holder.

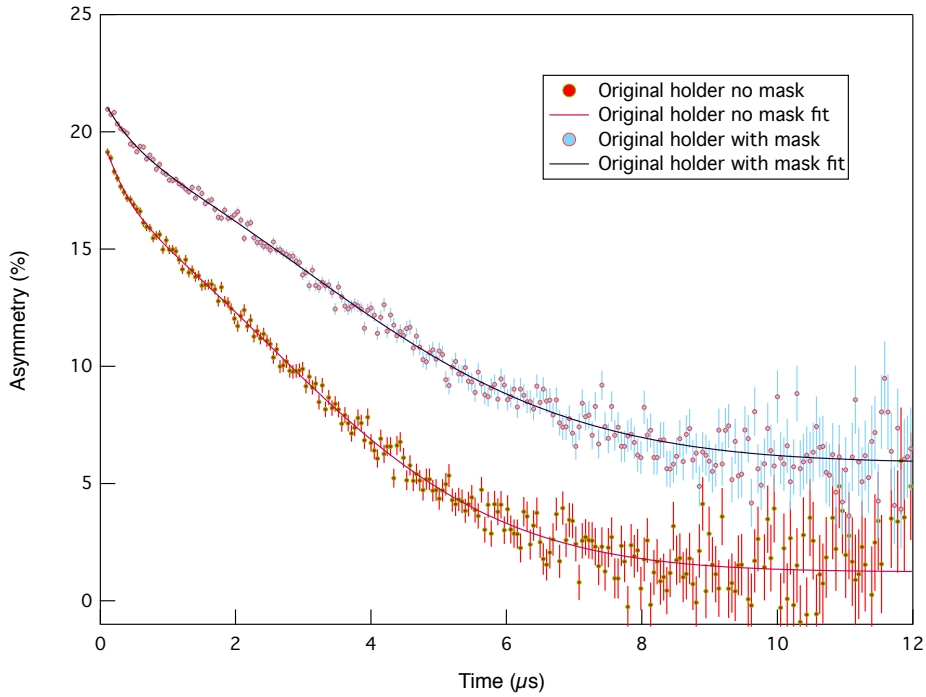

Figure 6.30: Asymmetry as a function of time, for the original sample holder set up, with and without a silver mask at 50 K. The signal itself shows a larger relaxation for the holder with no mask, but the actual shape of the signal appears to be the same for both set ups.

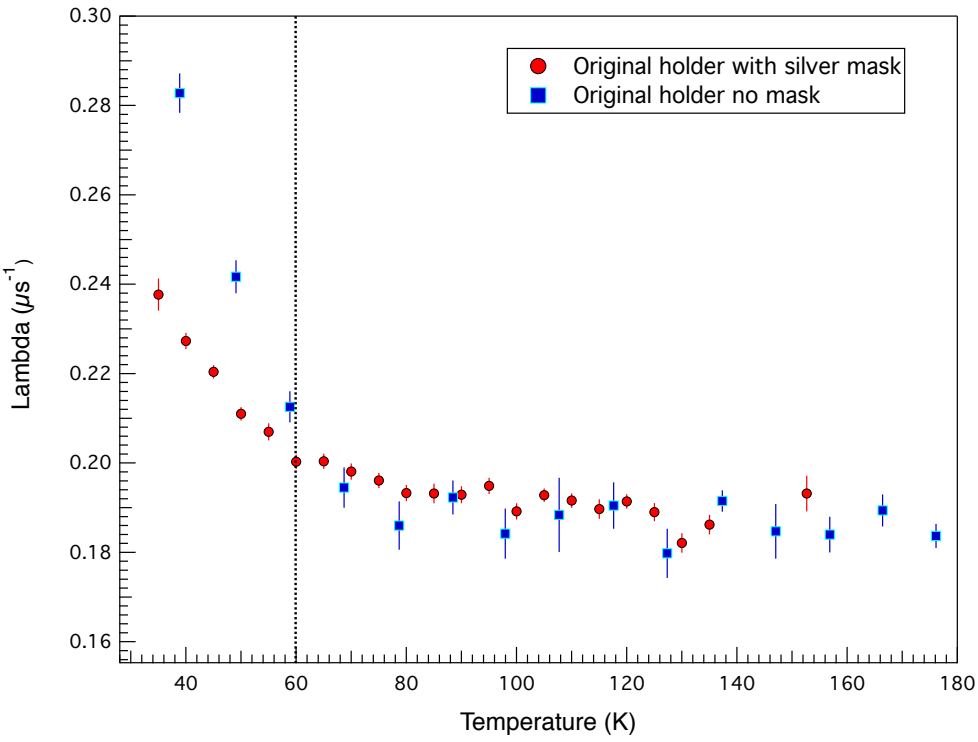

Figure 6.31: Relaxation rate as a function of temperature using the original sample holder. The blue markers correspond to the sample holder with no silver mask while the red markers correspond to the holder with a silver mask around the sample.

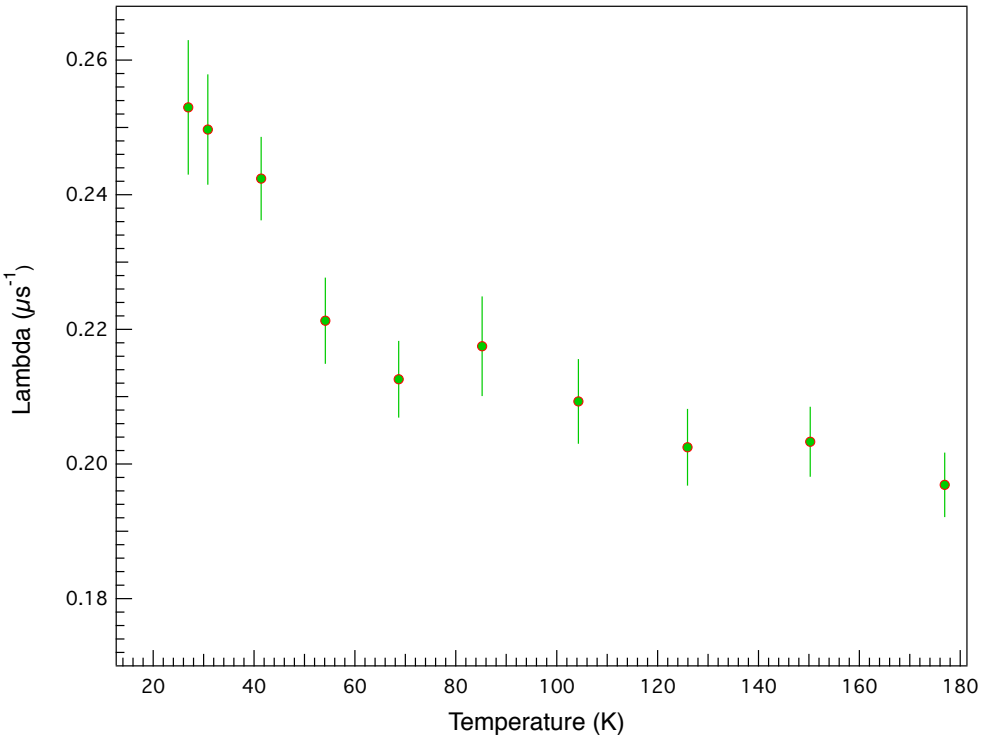

Figure 6.32: The corresponding relaxation rate versus temperature using the shapol holder with a silver mask. The green markers represents the relaxation obtained in ZF.

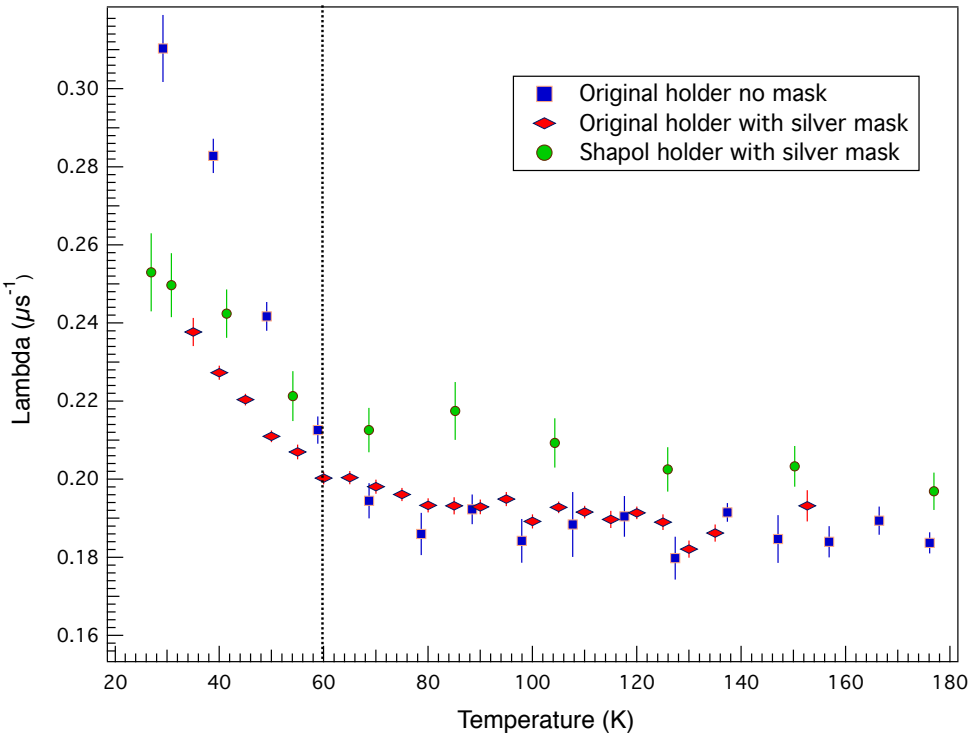

Figure 6.33: A summary of all the data collected on for this experiment. The relation rate for the different holders are all plotted in the same graph to allow a comparison of the data.

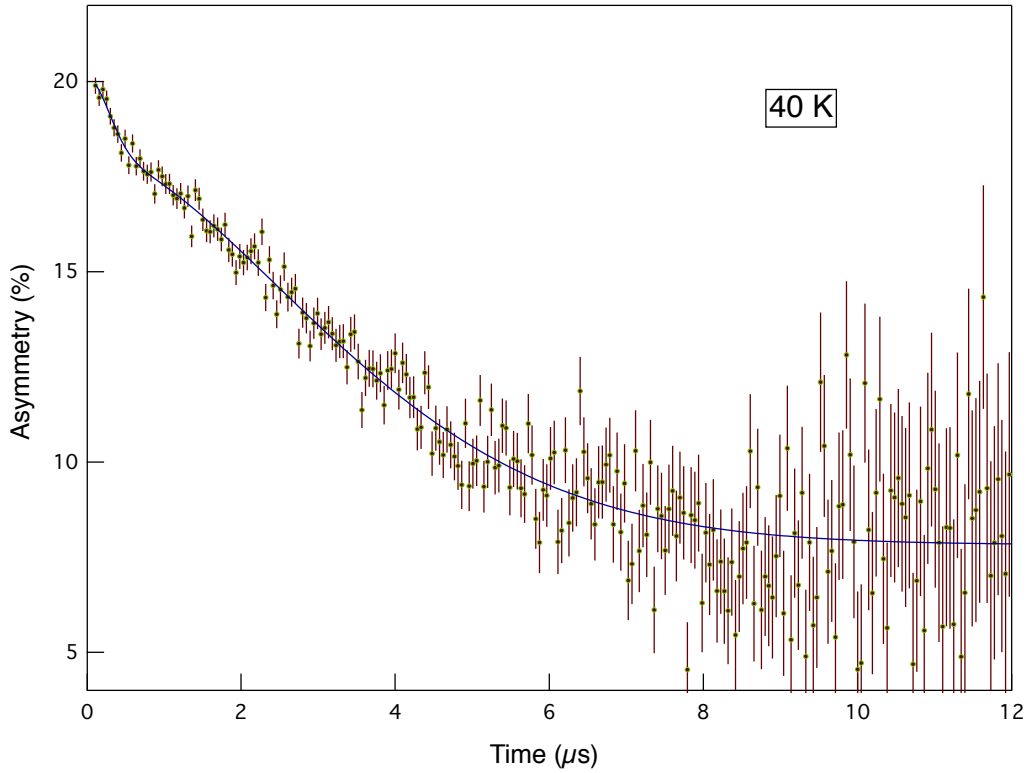

Figure 6.34: The asymmetry as a function of time at T=40 K, using the shapol holder. The solid blue line represents the fit to the data.

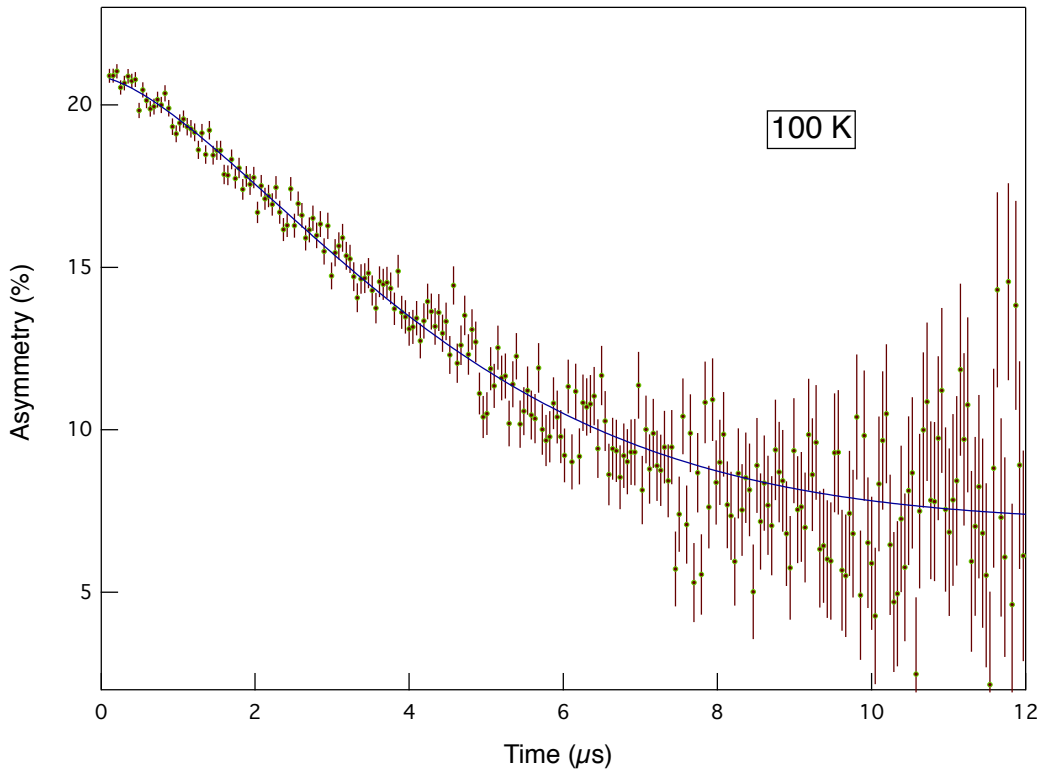

Figure 6.35: The asymmetry as a function of time at T=100 K, using the shapol holder. The solid blue line represents the fit to the data.

As one final check on the sample holder or even the spectrometer, we performed measurements on another sample at the Paul Scherrer Instutute (PSI) in Switzerland and although the data did not show an oscillation, we did observe a relaxation. The measurements at PSI were made using the Dolly spectrometer with active veto, which is almost an exact copy of the GPS muon instrument described in chapter 3.

For this experiment, the experimental set up was the same as that with the $BiFeO_3$ sample described in the previous chapter. A disk of nominal composition $Ba_4Dy_{0.87}Nb_{10}O_{30}$ (detailed chemical analysis was not performed), 10 mm in diameter and 0.59 mm thick, was wrapped inside a 50 μm foil packet and suspended between two silver forks with thin mylar tape. Just as with the $BiFeO_3$ sample, neither the Al foil nor the mylar tape were of sufficient thickness for the muons to stop in them and the silver forks were far enough away from the centre of the beam to ensure no muons would be implanted in them.

First, we cooled the sample down to base temperature ($T = 1.5$ K) and did a temperature scan with approximately 10 million events per temperature. The raw data was fitted using two simple exponentials above 50 K, corresponding to two different muon sites in the sample. Below 50 K, the data was fitted with a simple exponential and a stretched exponential with a $\beta = 2$.

Figures 6.36 and 6.37 show plots of the fitted parameters extracted from the fit functions at different temperatures. Figure 6.36, in which the relaxation rate λ_1 is plotted as a function of temperature, shows a relatively flat trend up to about 60 K, where it is clear that the relaxation rate undergoes a dramatic increase with decreasing temperature. The plot in figure 6.37 shows a rather similar behaviour to what is seen in figure 6.36, only in this plot the relaxation changes from a simple exponential with relaxation rate λ_2, to a stretched exponential with relaxation relaxation rate λ_2 and stretch parameter $\beta = 2$ above 50 K. Despite the change, the figure shows roughly the same trend; the relaxation rate remains fairly flat and constant with decreasing temperature, but below 50 K, there is a sudden increase in the relaxation which is the same behaviour as what figure 6.36 shows.

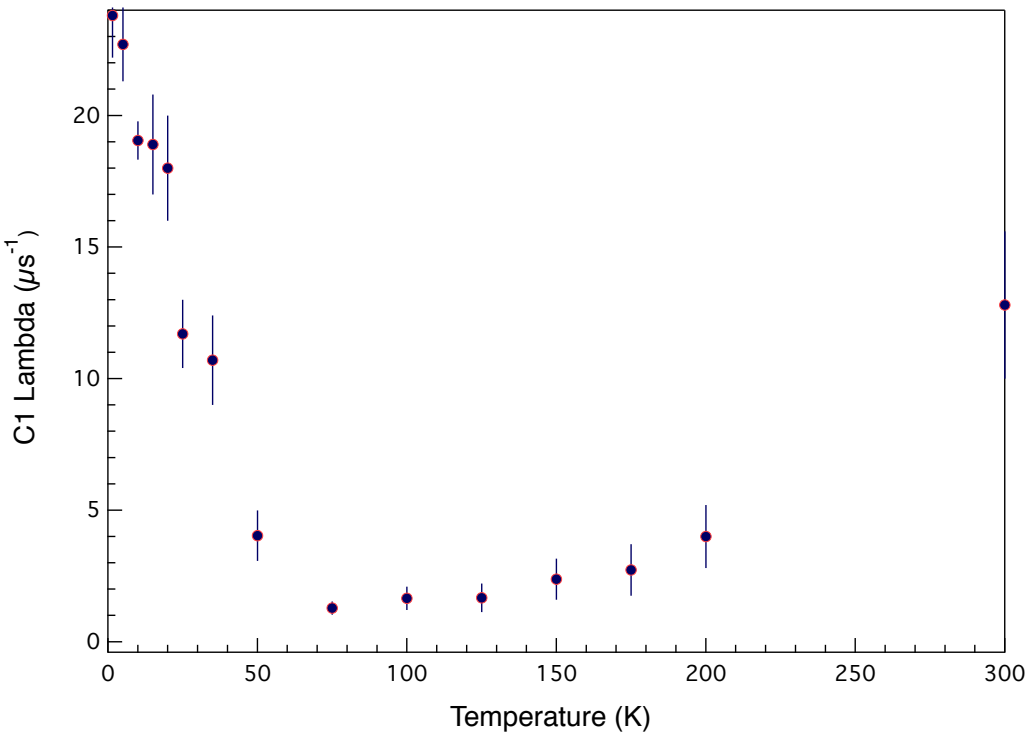

Figure 6.36: Plot of the relaxation rate λ versus temperature for the first component of the muon signal. The relaxation rate remains relatively flat from room temperature down to around 60 K, where a sudden, large increase in the relaxation can be can be observed.

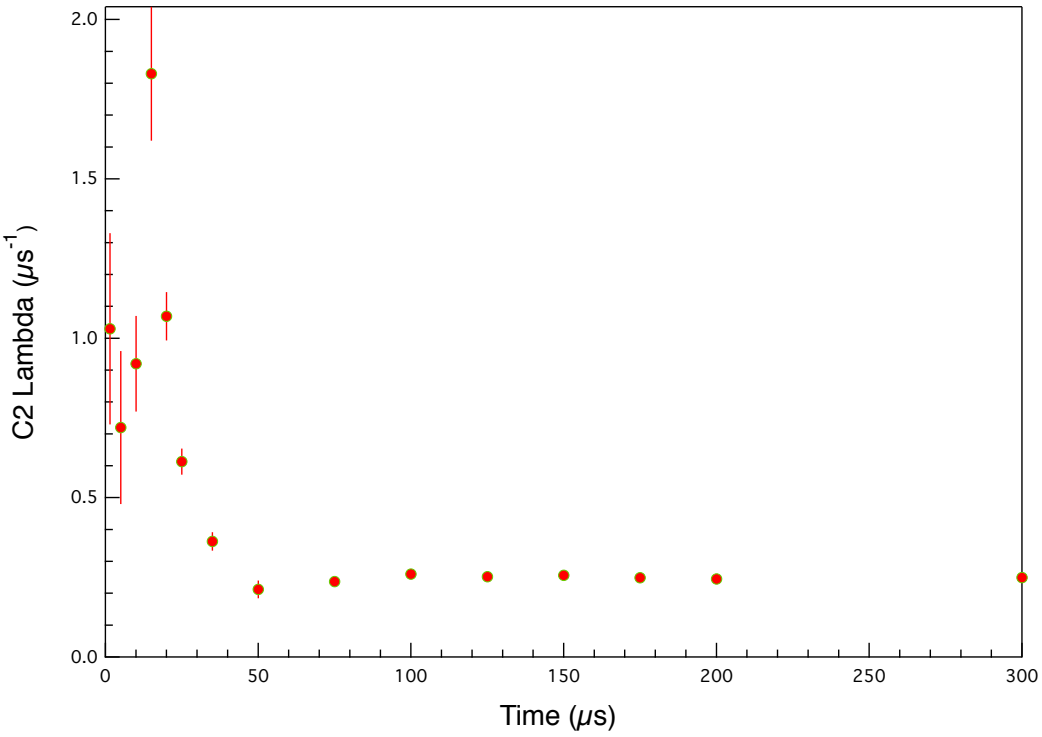

Figure 6.37: The relaxation rate for the second component of the muon signal. The data clearly shows a transition at 50 K, consistent with what is observed in the first component and other experiments.

Despite the fact that no oscillations can be observed in the data, as well the models to fit the two sets of data at high temperatures differ, there is consistency between the two sets of data in terms of the temperatures at which anomalies can be observed. Both, ISIS and PSI show a sudden change in the magnetism of the material at 50 K, confirming that the magnetic effects are independent of the sample holder and the spectrometer.

Having confirmed that the oscillation is the result of the sample, we now discuss the possible origins of the oscillation. There are a number of mechanisms that could give rise to the oscillation observed in our data, the most likely one being short ranged quasi-static 1D correlations between the spin chains. [6, p. 172].

Put simply, a spin chain is a one-dimensional line of spins which can be constrained to be parallel or antiparallel to a particular direction (Ising spins), point towards any point in a fixed plane (XY spins) or be free to move in any possible direction (Heisenberg spins). Spin chains can occur in crystals if the crystal structure is such as to keep the distance between chains sufficiently large so that the interaction between chains is negligible. In some systems, three-dimensional magnetic ordering may occur at very low temperatures as a result of an increase in the correlation between chains with decreasing temperature. In our sample, the in-plane distance between the Dy^{3+} ions is large enough for the interaction between the Dy ions to be minimum. Along the c-axis however, the distance is much less and therefore the interaction between the ions along this axis dominates, creating these 1D chains. This also appears to be the best way to explain our results in terms of the muon precession, which depending on the site, could indeed be precessing as a result of the short range correlation between the Dy spins along the c-axis.

The effect of short-range correlations has been studied before, and the effects on the muon signal have been observed experimentally in other systems with unusual, low temperature magnetic properties [175]. Figure 6.38 is a reproduced plot from reference [7], where a computed polarisation function $P_Z^{stat}(t)$ is plotted as a function of time, in order to check the effects of the short-range correlation on the spectrum. The dashed lines on the plot correspond to an ordinary Kubo-Toyabe function, which is usually used to describe the

data at high temperatures in a paramagnetic state, where nuclear moments dominate. The solid lines correspond to the computed polarization function $P_Z^{stat}(t)$, where short-range correlations are taken into account.

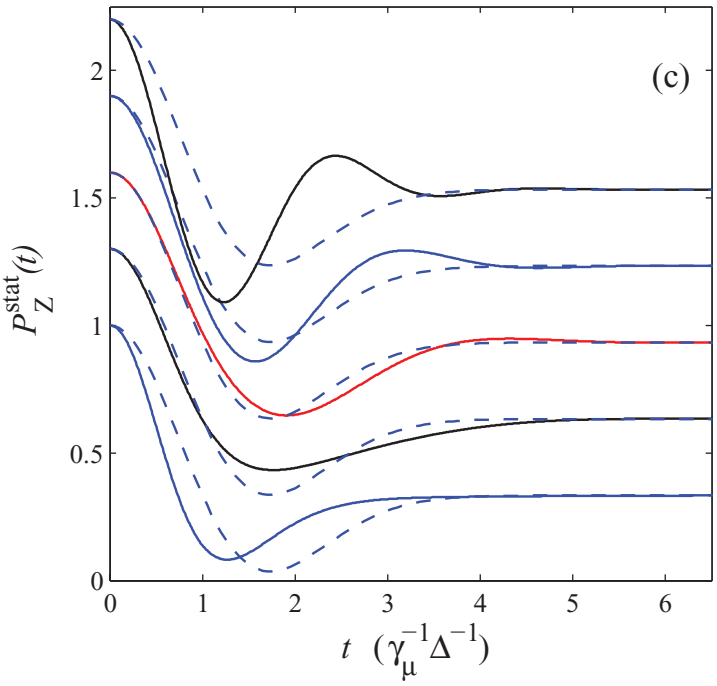

Figure 6.38: Plot of the computed polarisation function as a function of time. Dashed lines correspond to a Kubo-Toyabe function while the solid lines show the computed polarization taking into account the effects of short-range correlations, which can lead to oscillations in the data resembling an ordered magnetic system (figure reproduced from reference [7]).

The authors argue that short-range correlations have a strong effect on $P_Z^{stat}(t)$, and this can be observed on deepening of the minimum of $P_Z^{stat}(t)$ which causes the oscillations in the data to become more pronounced. More importantly, the authors explain that the polarisation function resembles that of an ordered magnetic system with a strong damping, which is the same as what we observe in our data. We are therefore convinced that despite the fact that there is no long range magnetic ordering in our material, the anomaly observed in our data at short times is indeed an oscillation. Furthermore, we argue that the the oscillation is the result of short-range correlations that can lead to precession, and therefore resemble long range order of the system.

Although we strongly believe that the origin of the oscillation is most likely related to short ranged correlations along the Dy chains, there are other possible mechanism that

could also give rise to an oscillation. These include:

- There could be a direct dipolar interaction between the implanted muons and individual Dy ions.
- It could be as a result of the Nb nuclear moments as well, which can be described by a Kubo-Toyabe relaxation function (see chapter 3). The KT function does indeed have an oscillating part, however, fitting a KT function to the data proved to be difficult and it did not provide a reliable fit. Also, the fact that the muon data shows changes in the temperature dependent frequency, further indicates that this is not the case. Moreover, nuclear moments should be decoupled from an electric field, especially if there is no weak structural change associated with the ME coupling and no structural changes as a function of temperature, as shown by the neutron data. Furthermore, RUS data suggest that the ferroelectricity is weakly coupled to the crystal structure. It is therefore safe to say that the origin of the oscillation is not as a result of nuclear moments.

6.7 Conclusions

In summary, we have shown that $Ba_4Dy_{0.87}Nb_{10}O_{30}$ is a material that displays magnetoelectric behaviour as the magnetic properties of the material can be tuned and manipulated with an electric field, indicating a strong magnetoelectric coupling. Measurements of the relative permitivity and dielectric loss as a function of temperature, as well as polarisation-field hysteresis loops, confirm that the material is ferroelectric with a paraelectric-ferroelectric transition temperature $T \sim 470$ K. Neutron data also gives evidence of the structural order of the ferroelectricity in terms of displacements of the Ba ions away from the centro-symmetric position in the oxygen octahedral cage.

Magnetic susceptibility measurements suggest that the material undergoes two different magnetic phase transitions, one at ~ 165 K and another at ~ 50 K. The anomaly at 50 K is the more pronounced throughout all the experiments, and it needs to be fur-

ther analysed and scrutinised in order to fully understand what's driving the change in magnetism at this point. μSR measurements corroborate the results obtained from the susceptibility measurements. Although the anomaly at 165 K revealed by the susceptibility measurements is not as pronounced, ISIS muon data also reveal magnetic anomalies at the same temperature (below which the precession frequency increases), and also a second anomaly at 50 K (which shows a significant reduction in the muons precession frequency), consistent with the susceptibility data.

μSR measurements under an applied electric field gives strong evidence that there is a strong coupling between the ferroelectricity and the magnetism in this material in terms of tuning of the magnetism with an applied electric field. A second electric field experiment performed on a different sample and using a different sample holder, reveals that the field does indeed have a significant effect on the magnetic properties of the material below 50 K.

RUS measurements confirm that the ME mechanism is not related to strain effects in the material, either a strain-ferroelectric coupling that then overlaps with the magnetism or viceversa. No anomalies can be observed on the RUS spectrum at the ferroelectric transition temperature or the temperatures at which magnetic anomalies occur.

Magnetic neutron scattering measurements confirm that there is no long range order in the material. The diffraction pattern looks the same throughout the entire temperature scan and there is no evidence of magnetic extra peaks developing or changes in the intensity as a result of the onset of magnetic ordering.

Fits to the ISIS muon data using several different models that fail to produce a reliable fit to the data at short times, confirm that the data does consists of a low frequency oscillation and not two separate relaxations.

Measurements performed using different sample holders in order to test whether or not the holder has a significant effect on the experimental spectrum, show that despite the changes in amplitude of the signal, there is no significant change in the signal itself. We conclude that the muon signal for these experiments comes from muons implanted in

the sample. Analysis of PSI muon data does not reveal an oscillation at short times as a result of different doping and number of events, but both data sets are consistent in terms of the temperatures at which anomalies can be observed, further confirming that the magnetic anomalies are completely independent of sample holder or the spectrometer used for the experiments.

6.8 Future work

Although we are convinced that the oscillation in our data is real, and that our analysis describes the data accurately, the next step would involve using the model used in reference [7] to have a better understanding of the physics of our material. In principle, this model could be used to extract the first four moments of the field distribution for our system and potentially the correlation lengths, to have a more clear picture about the interaction between the Dy in the 1D chains.

We are also left searching for a potential mechanism for the ME effect in this material, which is not related to indirect coupling, such as via structural strain. There are a number of alternative mechanism that could be worth considering, some of which involve domain walls. For example, whilst linear ME effect is symmetry-forbidden in $YMnO_3$ and $HoMnO_3$, the FE and AFM domain walls were found to be coincident [176]. Coupling in these walls is found to arise due to a reduced magnetic symmetry [15] or an interaction with the strain from the FE domain wall [176]. Whilst we have shown that the strain-coupling is weak in our material, the former mechanism - a reduction in magnetic symmetry at the grain boundaries is also not plausible. Any ME coupling mechanism that involves the FE domains would result in a change in relaxation rate but not precession frequency. This is because the complex set of boundary conditions that give rise to FE domains are intimately related to the crystal structure.

Another potential mechanism responsible for the magnetoelectric coupling in our material is spin-orbit interaction. As mentioned in chapter one, the behaviour of an electron with orbital angular momentum can be described as a circulating electric current, implying

that it has a magnetic moment with an associated magnetic field as a result it its motion. Electrons also posses a magnetic moments as a result of their spin. The magnetic moment as a result of the electron spin interacts with the magnetic field resulting from its orbital motion, and this interaction is known as spin-orbit coupling.The charge on the atomic nuclei determines the magnitude of the interaction, which in turn depends on the atomic number Z. This can be visualised by considering the electron to be fixed in space with the atomic nucleus orbiting around it. The resulting current as a result of the orbiting nucleus is larger for larger nuclear charge. The fact that the SO interaction is proportional to Z^4 [6, p. 210] implies that the SO interaction is very weak in light nuclei (in fact, in the hydrogen atom the interaction is negligible), but increases rapidly with atomic number. The fact that the magnitude of the coupling increases rapidly with atomic number, implies that for heavy atoms like Dy the interaction is particularly strong. An electric field could modify the orbital motion of the f electrons and this in turn could modify the magnetism of the material. X-ray magnetic circular dichroism (XMCD) measurements could help understand the effect of the electric field on the magnetism by measuring how the magnetic moments of the dysprosium ions are affected by the applied electric field. Electric field measurements of this kind are challenging, as they have never been performed before, but if it is possible to perform the measurements the results could potentially give a good idea about the unusual magnetic properties of this material as well as the sort of mechanism responsible for the ME coupling.

Figure 6.39 shows the ferroelectric phase diagram of the TTB sample. There are still a large number of samples that can be produced measured to see the effect that different doping will have on the ferroelectric properties of the material. In terms of the magnetism, we have no phase diagram describing what other magnetic species could be included, in order to improve the magnetic properties of the sample and potentially, magneto-electric response. Despite the fact that producing these materials is very challenging in terms of the chemistry, this is something that will have to be investigated thoroughly.

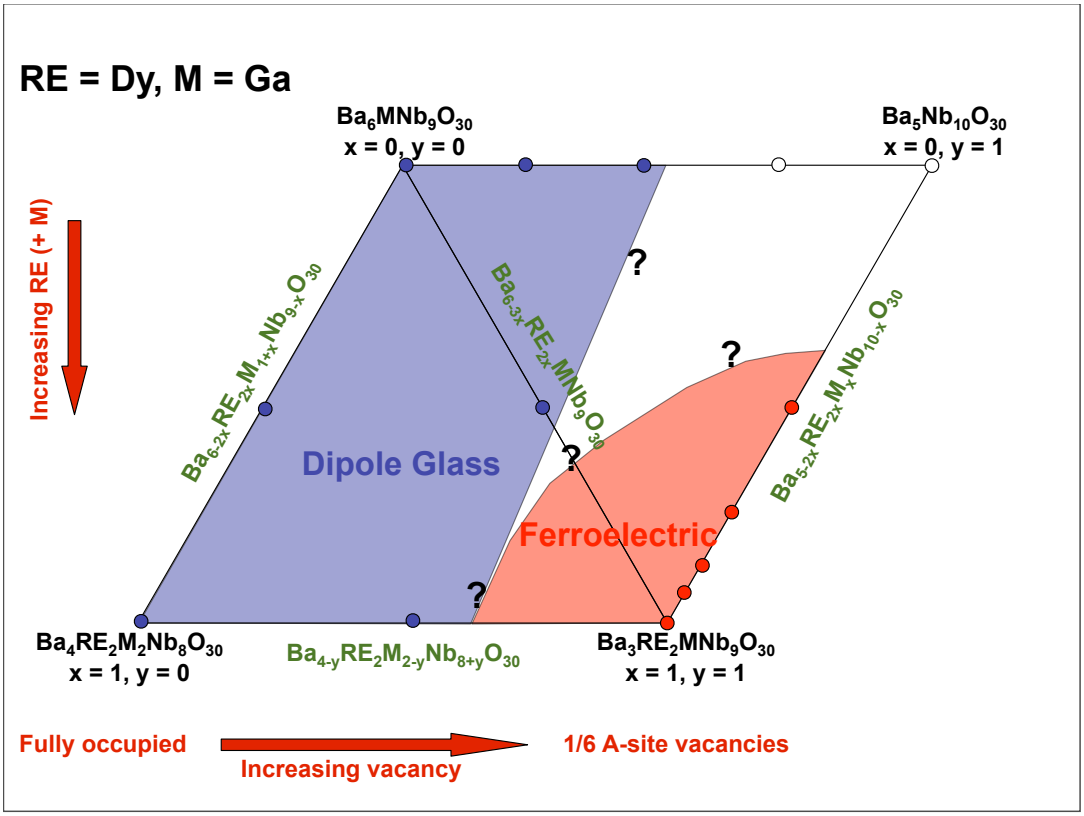

Figure 6.39: Ferroelectric phase diagram for the tetragonal tungsten bronze sample.

Bibliography

[1] B. B. Van Aken. *Nature Materials*, 3(164), 2004.

[2] D. Khomskii. *Physics-American Physical Society*, 2(20), 2009.

[3] T. Kimura. *Annual Review of Materials Research*, 37(387-413), 2007.

[4] S. J. Blundell. *Contemporary Physics*, 40(175), 1999.

[5] J. Wang *et al.* *Science*, 299(1719), 2003.

[6] S. Blundell. *Magnetism in condensed matter.* Oxford, 2001.

[7] A. Maisuradze A. Yaouanc and P. Dalmas de Rotier. *Physical Review B*, 87(134405), 2013.

[8] Gary A. Prinz. *Science*, 282(1660), 1998.

[9] S. A. Wolf *et al.* *Science*, 294(1488), 2001.

[10] Kenji Uchino. *Ferroelectric Devices.* Marcel Decker, 2000.

[11] J. F. Scott. *Ferroelectric memories.* Springer-Verlag, 2000.

[12] H. Schmid. *Ferroelectrics*, 162(665), 1994.

[13] Nicola A. Spaldin and Manfred Fiebig. *Science*, 309(391), 2005.

[14] T. Kimura et al. *Nature*, 426(55), 2003.

[15] Thomas Lottermoser and Manfred Fiebig. *Physical Review B*, 70(220407), 2004.

[16] N. D. Mathur W. Eerenstein and L. F. Scott. *Nature*, 442(759), 2006.

[17] M. Fiebig. *Journal of Physics D: Applied Physics*, 38(R123), 2005.

[18] H. Schmid. *International Journal of Magnetism*, 4(337), 1973.

[19] N. A. Hill. *Journal of physical chemistry*, 104(29), 2000.

[20] T. Kimura *et al.* *Physical Review B*, 67(180401(R)), 2003.

[21] T. Katsufuji *et al.* *Physical Review B*, 64(104419), 2001.

[22] N. Hur. *Nature*, 429(392), 2004.

[23] G. Lawes *et al.* *Physical Review Letters*, 95(087205), 2004.

[24] T. Kimura *et al.* *Physical Review B*, 73(220401), 2006.

[25] T. Kimura *et al.* *Physical Review Letters*, 94(137201), 2005.

[26] R. Jarrier *et al.* *Physical Review B*, 85(184104), 2012.

[27] G. Catalan and James F. Scott. *Advanced Materials*, 21(2463), 2009.

[28] L. C. Chapon. *EPJ Web of Conferences*, 22(00013), 2012.

[29] A. S. Borovik-Romanov and H. Grimmer. *International tables for Crystallography*, D 1.5(105), 2006.

[30] Martin T. Dove. *Structure and Dynamics: An atomic view of materials*. Oxford university press, 2003.

[31] I. Blech D. Shechtman. *Physical Review Letters*, 53(20), 1984.

[32] Hans Grimmer. *Acta Crytallographica*, A 36(839), 1980.

[33] Stephen Bramwell and Sean Giblin. *Nature*, 461(846), 2009.

[34] Nicola A. Spaldin. *Magnetic materials, fundamentals and applications second edition*. Cambridge University press, 2011.

[35] Sang-Wook Cheong and Maxim Mostovoy. *Nature materials*, 6(13), 2007.

[36] Cox DE et al. *Journal of Applied Physics*, 40(387413), 1969.

[37] Newnham R. E. et al. *Journal of Applied Physics*, 49(6088-91), 1978.

[38] R. E. Cohen. *Nature*, 358(136), 1992.

[39] J. Valasek. *Physical Review*, 17(4), 1920.

[40] P. Muralt. *Journal of Micromechanics and Microengineering*, 10(136), 2000.

[41] O. Auciello and J. F. Scott. *Physics Today*, 51(22), 1998.

[42] Millicent B. Smith et al. *Journal of American Chemical society*, 130(22), 1994.

[43] N. Sicron et al. *Physical Review B*, 50(18), 2007.

[44] http://www.doitpoms.ac.uk/tlplib/ferroelectrics/phase_changes.php.

[45] Matthew W. Stoltzfus et al. *Inorganic Chemistry*, 46(3839), 2007.

[46] N. A. Hill R. Seshadri. *Chemistry of materials*, 13(2892), 2001.

[47] J. A. McLeod. *Physical Review B*, 81(144103), 2010.

[48] D. V. Efremov. *Nature Materials*, 20(434217), 2004.

[49] J. van den Brink. *Journal of Physics: Condensed Matter*, 3(853), 2004.

[50] D. Khomskii. *Journal of Magnetism and Magnetic Materials*, 306(1-8), 2006.

[51] Subramanian *et al.* *Advanced materials*, 18(1737-1739), 2006.

[52] N.A. Spaldin C. Ederer. *Physical review B*, 74(020401), 2006.

[53] I. E. Dzyaloshinskii. *Soviet Physics JETP*, 10(628), 1959.

[54] D. N. Astrov. *Soviet Physics JETP*, 11(708), 1960.

[55] D. N. Astrov and Al' shin B. I. *Soviet Physics JETP*, 17(809), 1963.

[56] Schmid H Ascher E, Rieder H and Stossel H. *Journal of Applied Physics*, 37(1404), 1966.

[57] Segal D J Santoro R P and Newman R E. *J. Phys. Chem. Solids*, 27(1192), 1966.

[58] R. M. Hornreich W. F. Brown, Jr. and S. Shtrikman. *Physical review*, 168(574), 1968.

[59] J. P Rivera. *European Physical Journal B*, 71(299), 2009.

[60] T. Zhao *et al.* *Nature materials*, 5(823-829), 2006.

[61] W. C. Rontgen. *Annals of Physics*, 35(264), 1888.

[62] H. A. Wilson. *Philosophical Transactions of the Royal Society A*, 204(129), 1905.

[63] P. Curie. *Journal de physique*, 3(393), 1894.

[64] L. D. Landau. *The electrodynamics of continuous media*. Pergamon Press plc, 1959.

[65] R. D. Shannon. *Acta Crystallographica*, A 32(751), 1976.

[66] D. I. Khomskii T. Mizokawa and G. A. Sawatzky. *Physical Review B*, 60(10), 1999.

[67] M. Mostovoy. *Physical Review Letters*, 96(067601), 2006.

[68] H. Katzura. *Physical Review Letters*, 95(057205), 2005.

[69] M. Kenzelmann *et al.* *Physical Review Letters*, 95(087206), 2005.

[70] R. Kajimoto *et al.* *Physical review B*, 70(012401), 2004.

[71] S. Quezel *et al.* *Physica B*, 86-88(916-918), 1977.

[72] T. Arima *et al.* *Physical Review Letters*, 96(097202), 2006.

[73] T. Kimura. *Annual Review of condensed matter physics*, 3(93-110), 2007.

[74] K. Nakamura *et al.* *Journal of Physics and Particle Physics*, 37(075021), 2010.

[75] D. H. Frisch and J. H. Smith. *American Journal of Physics*, 31(342-355), 1963.

[76] http://pdg.lbl.gov/2013/listings/contents_listings.html.

[77] S. F. J. Cox. *Journal of Physics C: Solid State Physics*, 20(3187), 1986.

[78] S. H. Kilcoyne S. L. Lee and R. Cywinski. *Muon Science, Muons in Physics, Chemistry and Materials*. Scottish Universities Summer School in Physics, 1999.

[79] R. L. Garwin. *Physical Review*, 105(1415), 1957.

[80] Alain Yaouanc and Pierre Dalmas. *Muon Spin Rotation, Relaxation and Resonance. Applications to Condensed Matter*. Oxford University Press, 2011.

[81] P.J.C King *et al.* *Physica B: Condensed Matter*, 326(260-264), 2003.

[82] P Dalmas de Reotier and A Yaouanc. *Journal of Physics: Condensed Matter*, 9(9113-9166), 1997.

[83] R. S. Hayano *et al.* *Physical Review B*, 20(850), 1997.

[84] L. P. Le *et al.* *Physical Review B*, 48(7284), 1993.

[85] C. Bernhard *et al.* *Physical Review B*, 86(184509), 2012.

[86] http://www.isis.stfc.ac.uk.

[87] Ruth E. A. McKnight. *Doctoral Thesis: Anomalous elastic behaviour associated with phase transitions observed using resonant ultrasound spectroscopy*. Darwin College, University of Cambridge, 2009.

[88] R G Leisure and F A Willis. *Journal of Physics: Condensed Matter*, 9(6001-6029), 1997.

[89] Manuel Bibes and Agns Barthlmy. *Nature Materials*, 7(425), 2008.

[90] Y. Tokura. *Science*, 312(1481), 2005.

[91] M. Cazayous *et al.* *Physical review letters*, 101(037601), 2008.

[92] M. K. Singh *et al.* *Journal of Physics: Condensed Matter*, 20(252203), 2008.

[93] R. M. White *et al.* *Physical Review B*, 25(1822), 1982.

[94] N. Koshizuka *et al.* *Physical Review B*, 22(5394), 1980.

[95] M. K. Singh *et al.* *Journal of Physics: Condensed Matter*, 21(042202), 2009.

[96] M. K. Singh *et al.* *Physical review B*, 77(144403), 2008.

[97] J. F. Scott *et al.* *Journal of Physics: Condensed Matter*, 20(425223), 2008.

[98] J. Herrero-Albillos *et al.* *Journal of Physics: Condensed Matter*, 22(256001), 2010.

[99] R. Przenioso *et al.* *Journal of Physical Society of Japan*, 75(084718), 2006.

[100] X. Marti *et al.* *Physical Review Letters*, 106(236101), 2011.

[101] R Gerson W. J. James J. M. Moreau, C. Michel. *Journal of Physics and Chemistry in Solids*, 32(1315), 1971.

[102] H. Schmid F. Kubel. *Acta Crystallographica B*, 46(698), 1990.

[103] J. D. Bucci *et al. Journal of applied crystallography*, 5(187), 1972.

[104] H. Schmid P. Tissot S. J. Clark J. Robertson S. A. T. Redfern J. F. Scott R. Palai, R. S. Katiyar. *Physical Review B*, 77(014110), 2008.

[105] R. Haumont B. Dkhil L. Bellaiche I. A. Kornev, S. Lisenkov. *Physical Review Letters*, 99(227602), 2008.

[106] C. N. W. Darlington H. D. Megaw. *Acta Crystallographica A*, 31(161), 1975.

[107] S. Lisenkov L. Bellaiche J. Kreisel B. Dkhil R. Haumont, I. A. Kornev. *Physical Review B*, 78(134108), 2008.

[108] F. D. Morrison P. Lightfoot D. C. Arnold, K. S. Knight. *Physical Review Letters*, 102(027602), 2008.

[109] M-A. Einarsrud T. Grande S. M. Selbach, T. Tybell. *Advance Materials*, 20(3692), 2008.

[110] Guangyong Xu *et al. Applied Physics Letters*, 86(182905), 2005.

[111] Jiefang Li Guangyong Xu and D. Viehland. *Applied Physics Letters*, 89(222901), 2006.

[112] Jiefang Li *et al. Applied Physics Letters*, 84(5261), 2004.

[113] J. R. Teague *et al. Solid State Communications*, 8(1073), 1970.

[114] C. Ederer and N.A. Spaldin. *Curr. Opin. Solid State Mater. Sci.*, 9(128), 2005.

[115] J. B. Neaton *et al. Physical Review B*, 71(014113), 2005.

[116] D. Lebeugle *et al. Physical Review B*, 76(024116), 2007.

[117] D. Lebeugle *et al. Applied Physics Letters*, 91(022907), 2007.

[118] R. Haumont V. V. Shvartsman and J. Kreisel. *Applied Physics Letters*, 90(172115), 2007.

[119] I. Sosnovska *et al. Journal of Physics C: Solid State Physics*, 15(4835-4846), 1982.

[120] D. Lebeugle. *Physical review letters*, 100(227602), 2008.

[121] J. F. Scott *et al. Journal of Physics Condensed Matter*, 20(322203), 2008.

[122] R. Przenioslo *et al. Journal of Physics: Condensed Matter*, 18(2069), 2006.

[123] A. Palewicz *et al. Solid State Communications*, 140(359), 2006.

[124] I. Sosnowska *et al. Applied Physics A: Materials, Science and Processing*, 74(S1040-S1042), 2002.

[125] A. A. Bush *et al. JETP Letters*, 78(389), 2003.

[126] A. V. Zalesskii *et al. JETP Letters*, 95(101), 2002.

[127] Feiming *et al. Applied Physics Letters*, 86(032511), 2005.

[128] Claude Ederer and Nicola Spaldin. *Physical Review B*, 71(060401 (R)), 2005.

[129] Toru Moriya. *Physical Review*, 120(1), 1960.

[130] W. Eerenstein *et al. Science*, 307(1203), 2005.

[131] Yu. F. Popov *et al. JETP Letters*, 57(69), 2003.

[132] A. K. Zvezdin *et al. Journal of Magnetism and Magnetic Materials*, 300(224-228), 2006.

[133] I. H. Ismailzade *et al. Phys. Stat. Sol. A*, 57(99), 1980.

[134] A. M. Kadomtseva. *JETP Letters*, 79(571), 2004.

[135] C. Fennie. *Physical Review Letters*, 100(167203), 2008.

[136] C. Ederer and C. J. Fennie. *Journal of Physics: Condensed Matter*, 92(192906), 2008.

[137] S. Lee *et al. Applied Physics Letters*, 92(192906), 2008.

[138] D. Lebeugle *et al. Physical Review Letters*, 100(227602), 2008.

[139] A. T. Savici *et al. Physical Review B*, 66(014524), 2002.

[140] L. Schulz L. Nuccio and A. J. Drew. *Journal of Physics D: Applied Physics*, Submitted 2013, 2013.

[141] Y. J. Uemura *et al. Physical Review B*, 31(546), 1985.

[142] T. Lancaster *et al. Journal of Physics: Condensed Matter*, 19(376203), 2007.

[143] P Dalmas de Reotier and A Yaouanc. *Journal of Physics: Condensed Matter*, 4(4533-4556), 1992.

[144] S. Blundell *et al. Physical review B*, 81(092407), 2010.

[145] S. A. T. Redfern *et al. Journal of Physics: Condensed Matter*, 20(452205), 2008.

[146] E. Holzschuh *et al. Physical Review B, volume =*, 1983.

[147] R. L. Lichti C. Boekema and K. J. Ruegg. *Physical Review B, volume =*, 1984.

[148] T. Egami and S. J. L. Billinge. *Underneath the Bragg peaks, structural analysis of complex materials*. Pergamon, 2003.

[149] Valeri Petkov. *Materials Today*, 11(11), 2008.

[150] Simon J. L. Billinge and M. G. Kanatzidis. *Chemistry Communications*, (749-760), 2004.

[151] Simon J. L. Billinge. *Journal of Solid State Chemistry*, 181(1695-1700), 2008.

[152] C. A. Young and A. L. Goodwin. *Journal of Materials Chemistry*, 21(6464), 2011.

[153] A. L. Goodwin *et al.* *Physical Review B*, 72(214304), 2005.

[154] Alex C. Hannon. *Nuclear Instruments and Methods in Physics Research*, 551(88-107), 2005.

[155] http://www.isis.stfc.ac.uk/instruments/gem/.

[156] R. J. Zeches *et al.* *Science*, 326(977), 2009.

[157] Y. H. Chu *et al.* *Nature Materials*, 7(478), 2008.

[158] M. Gajek *et al.* *Nature Materials*, 6(296), 2007.

[159] Y. Tokunaga *et al.* *Nature Materials*, 8(558), 2009.

[160] H. Katzura *et al.* *Physical Review Letters*, 98, 2007.

[161] J. Ma *et al.* *Advance Materials*, 23(1062-1087), 2011.

[162] D. Arnold and F. Morrison. *Journal of Materials Chemistry*, 19(6485), 2009.

[163] P. G. Dickens and M. S. Whittingham. *Chemical Society Reviews*, 22(30), 1968.

[164] A. Daoud-Aladine A. Rotaru, D. C. Arnold and F. D. Morrison. *Physical Review B*, 83(184302), 2011.

[165] M. Passlack *et al.* *Applied Physics Letters*, 64(2715), 1994.

[166] J. D. Cashion *et al.* *Journal of Materials Science*, 3(402-407), 1968.

[167] Y. Shimakawa *et al.* *Physical Review B*, 61(6559), 2000.

[168] M. Venet *et al.* *Applied Physics Letters*, 94(172901), 1994.

[169] http://www.isis.stfc.ac.uk/support-laboratories/materials-characterisation-lab/quantum-design-ppms/physical-property-measurement-system-ppms10280.html.

[170] T. Toyabe R. Kubo. *in Magnetic Resonance and Relaxation.* North-Holland, 1967.

[171] J. Schiemer *et al.* *Physical Review B*, 88(054108), 2013.

[172] M. Carpenter *et al.* *Journal of Physics: Condensed Matter*, 24(045902), 2012.

[173] Martin T. Dove *et al.* *Mineralogical Magazine*, 59(629-639), 1995.

[174] http://www.isis.stfc.ac.uk/instruments/wish/.

[175] J. A. Hodges *et al.* *Physical Review Letters*, 88(077204), 2002.

[176] M. Fiebig *et al.* *Nature*, 419(818), 2002.